**ScuDo**
Scuola di Dottorato ~ Doctoral School
WHAT YOU ARE, TAKES YOU FAR

Doctoral Dissertation
Doctoral Program in Civil and Environmental Engineering (33th Cycle)

# Progress in planning mitigation and adaptation strategies driven by indigenous knowledge and numerical modelling to face hydrometeorological hazards in the Sahel

## Paolo Tamagnone

\* \* \* \* \* \*

**Supervisors**
Prof. Maurizio Rosso
Prof. Elena Comino

**Doctoral Examination Committee:**
Prof. Jerónimo Puertas Agudo, Referee, University of A Coruña
Prof. Alessandro Toffoli, Referee, University of Melbourne
Prof. Jaak Monbaliu, Catholic University of Leuven
Prof. Alessandro Valiani, Università degli studi di Ferrara
Prof. Francesco Laio, Politecnico di Torino

Politecnico di Torino
2020

I hereby declare that, the contents and organisation of this dissertation constitute my own original work and does not compromise in any way the rights of third parties, including those relating to the security of personal data.

………………………….....

Paolo Tamagnone

Turin, 2020

# Acknowledgement

I would like to express infinite gratitude to my family and my friends for being present every day of my life.

The greatest thank goes to Cristina for sharing with me all the difficulties and for being my lifeline when the waters were more troubled.

# Abstract

Natural hazards are becoming more and more a global issue since the negative impacts that are causing on the environment and the entire biological sphere. Nowadays, these phenomena are even more exacerbated by the ongoing climate changes and environmental degradation that are affecting, although with different severity, the whole planet. Among others, one of the hardest hit areas is the Sahel, the region that embeds all arid and semi-arid countries bordering the great Sahara Desert. In these regions, climate-related extremes are increasingly threatening the basis for developing modern societies, from securing the livelihood to the economic expansion. Besides the rising frequency with which natural catastrophes occur, the relentless growth of the population makes a large share of it progressively more exposed and vulnerable to these threats. Notwithstanding these facts that are already taking place among the African communities, future projections are depicting worse scenarios in which the hydrological framework will be characterized by an intensification of precipitation, higher temperatures, and longer dry spells. Thus, impelling is the necessity of developing adaptation and mitigation strategies to face anthropic and climate-related impacts.

In this context, the main purpose of the dissertation is to provide a comprehensive analysis of suitable strategies to deal with hydrometeorological hazards affecting the Sahel, especially against floods and droughts. All addressed investigations are characterized by the twofold purpose to be: (a) contextualized, i.e. indigenous knowledge has represented the starting point of each insight and analysis; (b) advanced, i.e. enhanced numerical models have been implemented to examine and meet the goal. The goals pursued in this thesis are (i) to provide all the preliminary analyses accomplished for the implementation of the first Early Warning System for flood alertness at the service of riverine populations of the Sirba river; (ii) to assess the capabilities of indigenous rainwater harvesting techniques (RWHT) to be adopted as an effective strategy for flood mitigation; (iii) to comprehensively investigate the benefits induced by using RWHT in mitigating the plant water stress induced by rainwater shortage.

Firstly, watershed characteristics and the temporal evolution of river flow are essential data to understand the river behaviour and set up mitigation and

prevention strategies against flooding. This thesis provides the recalibration of the rating curves and the updating of the discharge dataset of the Sirba River. The analysis of the updated flow time series underlines the rising trend in flood frequency and intensity. Moreover, a new changepoint into the dataset is detected in 2008, which identify the beginning of an epoch characterized by severe floods. The behavioural alterations of the river caused by land cover and climate changes are depicted through the calculation of its flow duration curves. Then, the flood hazard assessment of the Nigerien reach of the Sirba river is presented. The flood-prone areas are delineated and classified in conformity to the four alert classes currently used in Niger. The definition of the hazard thresholds exploits advanced non-stationary method able to consider the changes in the basin response to hydrometeorological extremes over time.

The second part of this dissertation offers a new concept: the use of indigenous agricultural practice for reducing runoff and mitigating flood hazard. To confirm such insight, the thesis analyses the hydraulic performances of the most used RWHT in sub-Saharan regions in terms of runoff reduction and infiltration increase. HEC-RAS and Iber are the numerical models chose to study processes occurring in the runoff formation and propagation. The simulations show that half-moons organized in staggered lines are the best configuration in reducing runoff. The right design may lead to runoff retention up to 87% and double the infiltration. Thus, the runoff collected into the field is water that does not immediately reach the river during rainstorms. The application of these techniques enhances the hydrological efficiency of the farmland bringing a noticeable reduction of the runoff coefficient.

The third part examines the capacity of RWHT in mitigating soil water stress prompted by water scarcity. A new methodology is proposed to compute the evapotranspiration rate into a two-dimensional distributed hydrological model used to simulate the water balance of typical Sahelian farmlands. This method expands the application field of such analyses in a context typically marked by data scarcity. Intercepting and storing overland flow, RWHT increase the water content in the root zone and the right design can even bring the water stress to zero. Furthermore, outcomes reveal that RWHT may lengthen the growing period up to 20 days, contributing to prevent crop failure.

# Contents

# List of Figures

# List of Tables

# Nomenclature

## Acronyms

ANFD: ANADIA Niger Flood Database
ASA: Arid and Semi-Arid
BB: Bossey Bangou
CSA: Climate-Smart Agriculture
DGRE: Direction Générale des Ressources en Eau
DHD: Decoupled Hydrological Discretization
DSM: Digital Surface Model
DSW: Diffusion Shallow Wave
EWS: Early Warning System
FAO: Food and Agriculture Organization
FDC: Flow Duration Curve
GEV: Generalized Extreme Value
GIS: Geographic Information System
GK: Garbey Kourou
HDI: Human Development Index
HEC-RAS: Hydrologic Engineering Center–River Analysis System
LHS: Latin Hypercube Sampling
LOESS: LOcally Estimated Scatterplot Smoothing
LULC: Land Use and Land Cover
MK: Mann-Kendall
MNRB: Middle Niger River Basin
NBA: Niger Basin Authority
NSGEV: Non-Stationary Generalized Extreme Value
OCS: Organized Convective System
ODA: Object Detection Algorithm
QGIS: Quantum Geographic Information System
RC: Rating Curve
RWHT: Rainwater Harvesting Techniques
SCS-CN: Soil Conservation Service-Curve Number

SDG: Sustainable Development Goals

SGEV: Stationary Generalized Extreme Value

SLAPIS: Système Locale d'Alerte Precoce contre les Inondations de la Sirba

SLM: Sustainable Land Management

SLWM: Sustainable Land and Water Management

SW: Shallow Water

WOCAT: World Overview of Conservation Approaches and Technologies

# Latin Symbols

AMAX: annual maximum discharge

$a, b$: rating curve parameters

$A_k$: face area of the edge k

$c$: $ET_p$ calibration coefficient

$c_f$: bed friction coefficient

$CN$: curve number

$d$: number of days

$D_{65}$: particle diameter correspondents to the sieve throughput of 65%

$D_s$: soil layer extent

$DP$: deep percolation rate

$ET$: evapotranspiration rate

$ET_c$: crop evapotranspiration

$ET_p$: potential evapotranspiration

$f$: Coriolis parameter

$FPR$: flow peak reduction

$g$: gravitational acceleration

$h$: water depth

$H$: water surface evevation

$I$: infiltration rate

$I_a$: initial abstraction

$I_{cum}$: cumulative infiltration

$I_s$: Initial saturation

$k$: cell edge

$K_c$: crop coefficient

$k_s$: saturated hydraulic conductivity

$k_{s,hole}$: saturated hydraulic conductivity of subcrust soil

$k_{s,p}$: saturated hydraulic conductivity of the deep soil

$k_{s,surface}$: saturated hydraulic conductivity of crusted soil

$K_s$: water stress coefficient

$L$: depth of the wetting front

$L_n$: number of days oof each growth stage

$n$: manning coefficient

$n_0$: roughness related to the natural materials on which the water flows

$n_{1,2,3,4}$ $and$ $m_5$: roughness corrective values

$p$: soil water depletion fraction

$P$: total precipitation

$P_e$: runoff depth

$PWD$: cumulative plant water deficit

$PWDR$: plant water deficit reduction

$Q.max$: maximum flow rate that flows out of the domain

$Q$: discharge

$q_{x,y}$: unit discharge components along x and y

$Q_d$: characteristic discharges

$\mathcal{R}$: hydraulic radius

$R$: rainfall intensity

$R_c$: runoff coefficient

$R^2$: coefficient of determination

$RAWC$: readily available water

$RT$: return time

$S$: soil storage capacity

$S_0$: conversion parameter

$S_t$: source term

$SAI$: standardized anomaly index

$t$: time

$T_a$: air temperature

$TAWC$: total available soil water content

$V$: velocity vector

$V_{annual}$: annual volume

$Vol.out$: cumulated volume of water that flows out of the domain

$VR$: volume reduction

$z_s$: free surface elevation

# Greek Symbols

$\alpha$: level of significance

$v_t$: eddy viscosity coefficient

$\eta$: soil porosity

$\theta$: soil moisture content

$\theta_{FC}$: water content at field capacity

$\theta_i$: initial soil moisture content

$\theta_t$: water content threshold

$\theta_{WP}$: water content at wilting point

$\lambda$: pore size distribution index

$\mu$: location parameter of GEV distribution

$\mu_{AMAX}$: mean of the AMAX time series

$\xi$: shape parameter of GEV distribution

$\rho_p$: Pearson's correlation coefficient

$\rho_s$: Spearman's correlation coefficient

$\sigma$: scale parameter of GEV distribution

$\sigma_{AMAX}$: standard deviation of the AMAX time series

$\phi_I$: infiltration increase

$\phi_Q$: flow peak reduction

$\phi_S$: water stress mitigation

$\phi_V$: volume reduction

$\Psi$: suction head

$\Omega$: cell volume

$\omega$: percentage of total daytime in which the evapotranspiration occurs

# Chapter 1

# Introduction

## 1.1  Foreword

Sub-Saharan countries are the poorest regions in the world. Among the 28 countries with a poverty rate above 30%, 27 are in Sub-Saharan Africa [1]. Notwithstanding, these countries have one of the highest fertility rates with 5.4 children per woman, which results in extremely fast population growth [2,3]. Projections estimate that the population might overcome 2 billion people by 2050, and further duplicate by the end of the current century [4]. Although the incessant effort in developing the entire socio-economic fabric, Sub-Saharan countries still occupy the last positions of the Human Development Index (HDI) ranking drawn up by the United Nations Development Programme [5] (Figure 1.1).

The Food and Agriculture Organization of the United Nations (FAO) reports that roughly 30% of the population is undernourished and 40% of infants risk their life due to malnutrition [6]. To face the constant hazard of famine, farmers incessantly strive to boost the local agricultural production in their scarcely fertile lands, naturally poor in organic matter. During the last 50 years, the increase in food production was achieved mainly by expanding the extent of cropland but with a scarce cereal yield compared with the rest of the world, since the artificial fertilizers were too expensive for the majority [7,8]. Moreover, the ongoing climate changes are forcing Sahelian farmers to find innovative strategies to deal with droughts, unpredictable rainfall, and depletion of soil nutrients. The research community have identified Africa as one of the parts of the world in which the climate changes will have the major impacts [9,10].
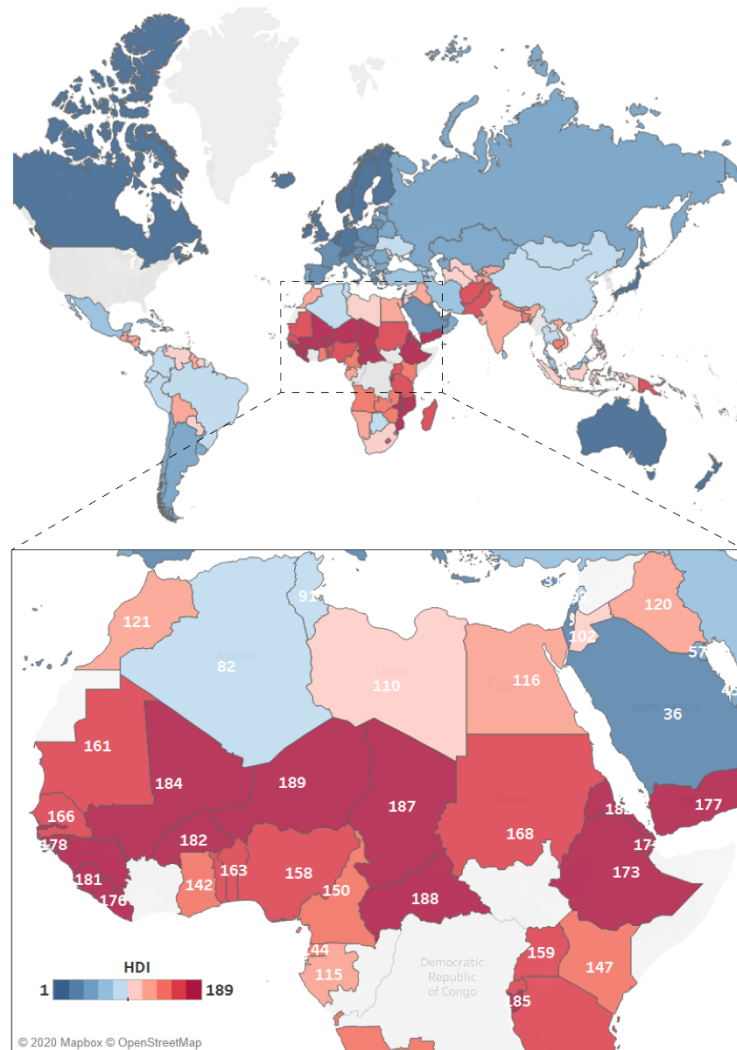
Figure 1.1 Worldwide ranking of the Human Development Index, updated to 2018. Enlargement: overview of the HDI values of sub-Saharan countries. (source: [5], maps elaborated by the author)

The recent history of the Sahel has shown how this part of the world is prone to sensitive changes in its climate. Over the last 70 years, the Sahelian climate has been characterized by three well-marked phases with a specific hydrological outline. The first period extends from the installation of the first rain-gauging stations (middle of the last century) to the end of the 1960s in which rain fell abundantly with a constant pattern. Then, twenty years (1970-1990), locally remembered as the "*great drought*", characterized by a persistent rainfall deficit. Indeed, over this dry epoch, annual precipitations were averagely 200 mm lower than in the previous decades [11]. After that, a third period starts from the end of the 20th century and shows a slight increase in precipitation [11–13] (see Figure 1.2). This positive trend, labelled as the "*return to wet conditions*" or "*recovery of rainfall*", gives hope for the start of a period of regreening of the Sahel [14,15].
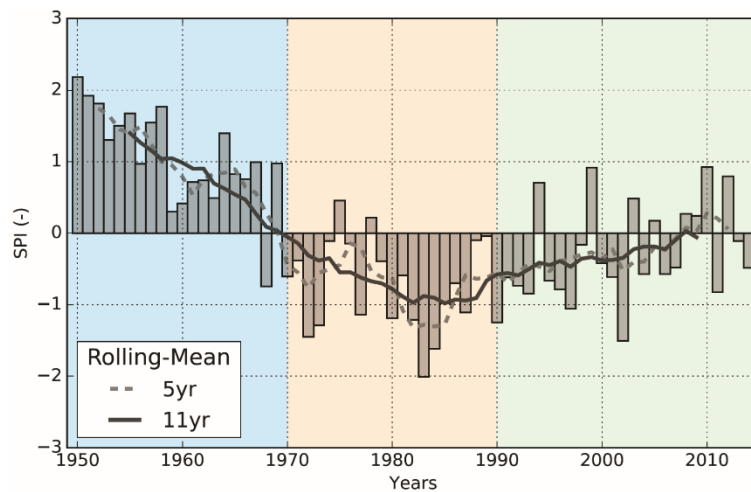
Figure 1.2 Standardized annual precipitation index for the Sahelian region. The three hydrological epochs are highlighted by colours. Colouring: light blue represents the wet epoch, the light orange covers the 20 year of drought and the light green displays the recovery of rainfall (adapted from [16]).

Even though the annual total amount of precipitation almost reached the average of the entire recorded period [17], rainfall events show a greater interannual variability that is leading to an exacerbation of rainstorms. Particularly, the rainfall regime of the last twenty years is characterized by a smaller number of rainy days and a significant growth of the occurrence of extreme daily rainfall [18,19]. This corresponds to an increase of hydrodynamic intensity, in which the hydrological cycle is characterized by longer dry spells and higher precipitation intensity [16,20]. With the ongoing global warming, this is one of the climate anomalies that is harshly affecting African countries nowadays [21]. Climate scientists are striving to understand how global warming is conditioning the hydrological cycle. An immediate consequence is that a warmer atmosphere may store a higher degree of moisture and consequently generates catastrophic rainstorms. The study of Taylor et al. [22] showed how the higher temperature is responsible for tripling the frequency of extreme storms in West African Sahel. The Sahelian storms are among the most powerful on the planet, with intensities exceeding hundreds of mm per hour [23]. The higher frequency of extreme events tied with incessant land degradation is leading to severe floods [24–26]. Evident examples are the massive downpour that deposited 263 mm of rain over the capital of Burkina Faso, flooded half of the city, and forced 150,000 people to leave their homes, in 2009, and the Niger River flood of 2012 and 2020, the two most intense flood ever registered in the Middle Niger Basin. Notwithstanding the evident impact on watersheds dynamics of this harsh rainy pattern, the recurrent occurrence of floods it is not totally understood. Indeed, the amount of precipitation that falls every year is still lower than the wetter period

before the great drought. This ambiguous phenomenon, called the "*Sahelian Paradox*", has been deeply analysed during the last 30 years [15,27–31]. It was first observed during the twenty years of drought in which, despite the shortage of precipitation, the discharge of Sahelian rivers showed a remarkable increase [32,33]. A great debate grew in the scientific community: what are the most important factors driving this paradoxical behaviour in the Sahel strip? Two different factors were analysed as possible drivers of the increase in flood magnitude: land use/land cover (LULC) changes and hydrometeorological changes.

Descroix et al. [32] argued that the uncontrolled deforestation and clarification of the savannah to create agricultural lands is leading to soil crusting and a consequent decrease in soil water hold capacity. These authors extensively observed this phenomenon happening on the right tributaries of the Middle Niger River (Sirba, Gorouol and Dargol rivers). This change of LULC drastically affects the hydrological response of basins, simultaneously enhancing the runoff coefficient and decreasing the time of concentration (Figure 1.3). Therefore, they determined a direct correlation between the increase in river discharge and the increased runoff coefficient of the Sahelian watersheds.
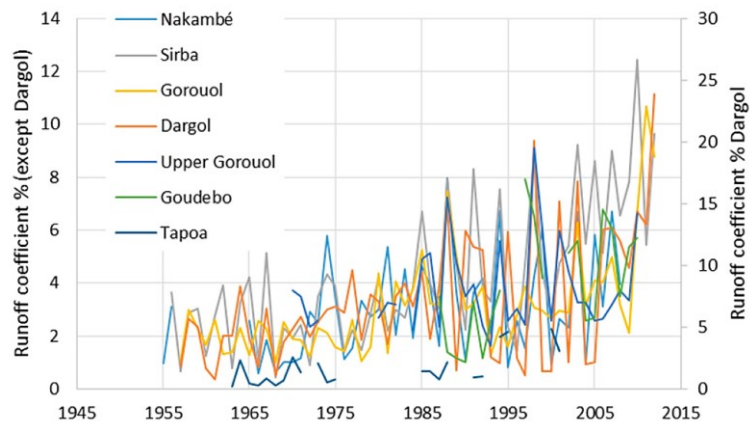


Figure 1.3 The runoff coefficients of Sahelian rivers. The trends show the evolution over time of the runoff coefficient with a net increase during the dry period and an exponential rise after the drought (source: [14])

By contrast, Aich et al. [34] established that the cause of increasing flood intensity can be connected with climate changes. They found that the recovery of rainfall, therefore a return to wet conditions, is the key driver for the increased discharge, explained by the direct correlation of the precipitation and streamflow trends in the last three decades.

Updated studies claimed that is not totally clear what is the major driver and have suggested that the mutual influence strongly depends on the local climatic

and territorial features [24,35,36]. Thus, each basin or sub-basin should be analysed carefully to understand which aspect leads to the intensification of the flow rate regime. All these studies, both data-based and modelling approach, needs of reliable and continuous dataset to achieve a robust result. Unfortunately, failures of gauging stations or lack of maintenance often cause losses of data. Even worse, the acquisition of wrong records, such as from an obsolete rating curve that is no more representative for the river cross-sections, which leads to unrealistic measurements. According to this, during the research activities, a critical mismatch was found in the water balance of the Middle Niger River at Niamey, the Nigerien capital. Working at the sub-basin scale, the Sirba river flow data showed a significant difference between the discharge calculated with the current rating curve and the discharge measured during field surveys. The recalibration of the Sirba river's rating curves and the update of the flow time series is addressed in this dissertation.

The Niger River is a shocking example of the impacts induced by the abovementioned climatological and terrestrial factors on its hydrology. An increase in the occurrence and magnitude of extreme flooding events in the Niger River and its tributaries has been registered in recent decades and above all during the last 10 years [26,31,32,34,37–39]. This exacerbation of extreme floods, in addition to the water scarcity, was identified as one of the most significant problems affecting the African countries [40]. In Niger, the number of people and their assets damaged by floods have sharply increased during the past decades [26,37]. These catastrophes have raised the awareness of local administrations toward the necessity of developing policies and strategies concerning flood risk adaptation and mitigation, such as hazard mapping and Early Warning Systems (EWS) [41]. A case study of the planning and realization of such strategies in the sub-Saharan area is presented in this thesis. The dissertation reports all phases and methodologies implemented to draw the flood hazard mapping of the Nigerien reach of the Sirba River.

In recent years, mainly in West Africa, scientific and technical teams together with the local population are striving to set up reliable systems to meet the needs for flood risk early warning [42]. The objective of these projects is not limited to saving lives, but they would like to provide a useful service to also save assets or livelihoods [43]. Likewise, preserving the productive activities that are the basis of a growing economy [44]. Several case studies have identified a clear cause-effect relation between the occurrence of hydrometeorological extremes and the reduction of GDP [45]. Thus, in order to preserve their developing economy, many actors (such as local governments, aid associations, Non-Governmental Organizations,

cooperation and developing programs, and so on) are putting themselves on the line to find feasible and reliable solutions [46]. In these countries, almost 70% of Africa's labour force is employed in the agricultural sector that presents the first source of incomes [47]. More than 95% of the crop production comes from rainfed agriculture, which relies only on the water that falls from the sky to grow crops [48]. Hence, not only a large slice of the economic sector but also food security is particularly vulnerable to the impact of hydrometeorological extremes induced by the ongoing climate changes.

Due to the fragile economic stability that marks the sub-Saharan countries, often, there are not enough resources to plan structural defence works or ad-hoc high-tech solutions to contrast these natural hazards [49]. Therefore, in recent years, the process of problem-solving is moving from the directly interested stakeholders instead from the top on the decision hierarchy.

Innovative farmers are starting to adopt improved practices to deal with climate changes and gain benefits from this harsh climate pattern. These agricultural systems are the crucial actions to meet the future climate-challenges and to act a transition towards a Climate-Smart Agriculture (CSA) [50]. FAO defines the CSA as "*an approach to developing the technical, policy and investment conditions to achieve sustainable agricultural development for food security under climate change*" [51]. It aims to promote sustainable development across the economic, environmental, and social fields. CSA is based on 3 pillars: (1) improvement of agricultural productivity and the connected incomes; (2) enhancing the resilience and adaptation to climate changes; (3) decreasing greenhouse gas emissions. All these actions have the common purpose to boost the achievement of Sustainable Development Goals (SDG) conveyed by the United Nations for 2016-2030 [52]. Among the 17 goals, CSA can help sub-Saharan inhabitants to cope with the five ones listed in Figure 1.4.



Figure 1.4 Sustainable Development Goals related to CSA technologies. (source: [53])

Among several CSA technologies, agroforestry, farmed managed natural regeneration and sustainable land and water management (SLWM) practices have demonstrated to be effective strategies to deal with ecological degradation and significantly increase the food production in drylands [54–59]. According to the World Resources Institute's investigation, improving water and land management

on just 25% of sub-Saharan Africa's cropland would provide an additional 22 million tons of food, moving towards food security [7]. In a farming system predominantly based on rainfed agriculture, the water scarcity represents the most critical limiting factor. Hence, farmers have developed several SLWM techniques for efficiently harvest rainwater, making the best use of the resource [60].

During the past thirty years, water harvesting has been defined by several authors coming from different specializations. Focusing on food production, Critchley et al. [61] defined water harvesting as a "*rudimentary form of irrigation*" in which runoff is collected for productive scopes. Oweiss [62] explained how water harvesting is the process in which rainfall is collected in a catchment area and it is concentrated in a smaller target area to be used. The definition contained in the book Water harvesting-Guidelines to Good Practice [63] is: "*the collection and management of floodwater or rainwater runoff to increase water availability for domestic and agricultural use as well as ecosystem sustenance*". In addition to these definitions, many authors have maned the technologies used to harvest rainfall with different terms such as Runoff Water Harvesting is the term used by Salazar at al. [64], Rainwater Harvesting Practice [65], or the term Rainwater Harvesting Techniques (RWHT), adopted by Biazin et al. [66]. Among the different terminologies, RWHT is the most widely recognized and used along with the whole dissertation. RWHT have been used in worldwide arid and semi-arid (ASA) countries (Middle East, China, India, Americas and Africa) over the history but their use was put aside during the green revolution in which new technologies resulted more successful [63,67]. Nowadays, in the era characterized by climate changes, the utilization of rainwater harvesting techniques is rediscovered as adaptive behaviour to cope with the increasing water scarcity and climate exacerbation [68–70]. Furthermore, they represent an unmissable opportunity to benefit from the ongoing meteorological pattern characterized by slightly increasing precipitation [71,72]. African farmers are using RWHT principally to collect overland flow, increasing the soil moisture and fertility and consequently enhancing the crop yield [57,73]. Many studies have analysed the benefit in crop production provided by the adoption of these techniques [54,55,59,74]. Developed from indigenous expertise and knowledge, RWHT are being promoted as CSA solutions for soil and water conservation [75,76].

In the Sahel, half-moon and planting pits, known locally as demi-lunes and zai/tassa, are popular among smallholder farmers. They are widely used in Burkina Faso, Ethiopia, Mali, and Niger [77]. The study of Zouré et al. [78] clearly showed the multiple benefits of using these farming practices in mitigating

the effect of dry spells and improving the crop yield. Fatondji [79] showed the capability of zai of doubling water use efficiency of the cereal at the bases of the Sahelian farmers' diet, the millet. The functions of decreasing surface runoff, reducing erosion of fertile topsoil and increasing infiltration are effective in contrasting the ongoing desertification in drought-prone areas and restoring degraded lands [80,81].

Besides food production, other studies have developed methodologies to identify suitable sites where the use of RWHT could be successful [60,82,83]. The majority of the investigations related to RWHT are carried out on experimental sites in which experimental plots are instrumented and records are analysed [78,84–88]. Despite previous studies have revealed the effectiveness of numerical modelling in simulating the effects induced by morphological alterations [89], a very few researches have investigated the impacts induced by the presence of RWHT through numerical models.

In addition, very little attention has been paid to the capability of RWHT in reducing the surface runoff and no researches have been found that match the concept of flood mitigation with these practices. So far, the concept of flood reduction coupled with RWHT has been analysed primarily in flood-prone urban areas [90–93]. In rural environments, Al-Seekh and Mohammad [94] and Ali et al. [95] conducted tests on artificial runoff plots to directly measure the amount of runoff after rainstorms. Welderufael et al. [96] implemented a Morin and Cluff runoff model to investigate the rainfall-runoff relationships on treated and non-treated fields of Dera, Ethiopia. Verbist et al. [97] evaluated the effect of an infiltration trench on a hillside in Chile combining on-site measurements and numerical simulation using the software HYDRUS-2D.

Filling these lacks is one of the goals of this dissertation, through the comprehensive assessment of the hydraulic/hydrological performances of RWHT through advanced hydraulic/hydrological modelling.

RWHT are practices that, despite they require exhausting manual labour, are marked by simplicity, adaptability, replicability, and the low cost of realization and maintenance. All these features make the usage of rainwater harvesting techniques apt in a wide variety of contexts [94]. On the base of this consideration, this thesis pursues the objective of providing feasible and repeatable methodologies which could guide local administration, landscape planners or directly farmers during the decision process for the choice of the best technique and design to use in every context.

## 1.2   Context

The work presented in this dissertation has been conducted in the framework of the ASA regions of the Sahel. The Sahelian belt stretches from the parallel 17° N to 10° N, from north to south, and spans from the Atlantic Ocean coasts to the coasts of Red Sea, from west to east (Figure 1.5). The Sahelian belt run across big countries such as Senegal, Mauritania, Mali, Burkina Faso, Niger, Chad, Sudan. It represents a transitional zone between the arid desert of Sahara and the tropical forests overlooking the coast. The natural Sahelian landscape is principally composed of a patchwork of shrub bush, fallow savannah and rainfed millet fields. Nowadays, the original environment is strongly affected by the fast population growth. Indeed, some areas originally covered by the savannah vegetation are continuously replaced with cultivated and pastoral areas [32,98].
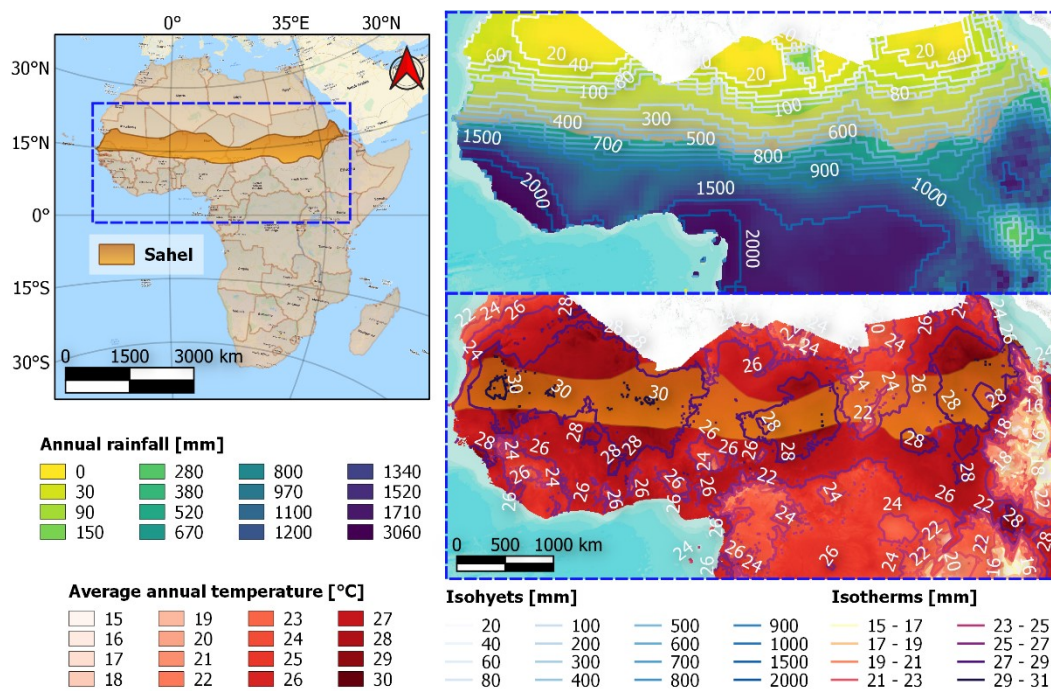


Figure 1.5 Geolocation of the Sahelian strip. Upper enlargement: long-term annual rainfall and isohyets (1960-2014). Lower enlargement: average temperature and isotherms (1970–2000). [99,100].

Its climate is predominantly arid at the border with the Sahara Desert, with rainfall almost absent, and semiarid towards the south with an annual pluviometry that ranges from 600 to 800 mm [100,101]. It has an ecological dry season of 7-9 months and a rainfall pattern mainly concentrated in August. Temperatures are affected by the winds that control the ecological season. During the dry season, when the Harmattan blows, the temperature ranges between 25°C and 42°C while,

during the colder period, when African monsoons bring moist air, the temperatures drop down to a range of 15-27°C (enlargements in Figure 1.5).

The Sahelian strip, an area set in a fragile context, has been undergoing dramatic climate and land-use changes since the middle of the 20th century. In the following years, this area will be one of the most affected by climate changes [21]. The study conducted by the University of Notre Dame showed that the Sahelian countries are among countries with the highest level of vulnerability to climate changes [102]. Indeed, countries such as Niger, Chad, Sudan, and Mali fill the last positions in the global rankings.

The study of Todzo et al. [103] reveals that the Sahel is going to experience an increase in precipitation and temperature faster than the global average in the near future. Moreover, according to the findings of Seidou [71], the rainfall pattern is expected to become more intense and less frequent, therefore characterized by severe rainstorms and longer and more likely periods of drought. Previous studies showed that roughly 50% of annual precipitation falls in the occurrence of a small number of extremely intense and short events [18,23]. This type of climate and future perspectives are not in favour of a farming system mostly based on rainfed agriculture. A critic forecast is conceived in the paper "*Climate change and variability in the Sahel region: impacts and adaptation strategies in the agricultural sector*", which reports that the Chad and Niger, two countries of the central Sahel, could likely lose nearly the whole production coming from rainfed agriculture by 2100 [104]. For these reasons, farmers living in ASA areas are striving to develop suitable and efficient water management practices. Along with the harsh climate, the ongoing land degradation due to desertification and anthropic deforestation is reducing the land fertility and increasing the exposure of soil to crustification [14].

Zooming in, towards the central Sahel, a considerable portion of the research effort was focused on the Sirba River, one of the main tributaries of the Middle Niger River Basin (MNRB). It is the major tributary in terms of discharge and the second in terms of watershed size. The Sirba river basin encompasses a surface of approximately 39'000 km$^2$ across two countries, Burkina Faso and Niger. The Burkinabe waterhead covers the 93% of the whole surface while, downstream, the Nigerien reach occupies the remaining share. The topography of the basin is predominantly flat, whit slight height variations between the upper and the lower part and without steep slopes. The main altimetric and planimetric features of the basin are summarized in Table 1.1.

Table 1.1 Plano-altimetric characteristics of the Sirba River Basin (adapted from [38]).

| Sirba River Basin | | | | Sirba River | |
|---|---|---|---|---|---|
| Surface [km$^2$] | Altitude [meter a.s.l.] | | Slope [%] | Length [km] | Slope [%] |
| | max | mean | min | mean | max | mean |
| 39'138 | 444 | 286 | 181 | 1.12 | 439 | 0.02 |

The river basin is located in the Inter-Tropical Convergence Zone between the isohyets 400 and 700 mm. It is characterized by a Sahelian semiarid climate. The meteorological conditions of this area can be delineated in two well-defined seasons: the dry season (October–May) and the wet season (June–September) [72,105–107]. The Sirba River is an intermittent river, typical of those areas, in which flows water for about six months a year. Its hydrology is tightly related to the monsoons coming from the Atlantic Ocean. During the monsoon season, the riverbed is predominantly filled by the surface runoff generated by the abundant rainfall. Reversely, during the dry season, the riverbed is dry since the exchanges with the groundwater are almost non-existent.

The Sirba River rises just a few kilometres upstream from the Niger border, in correspondence of the confluence between its main tributaries (Yali, Faga, and Koulouko rivers) flowing from the headwater in Burkina Faso. Then, it flows towards downstream, into the Nigerien valley, for about 100 km until the confluence into the Niger River.
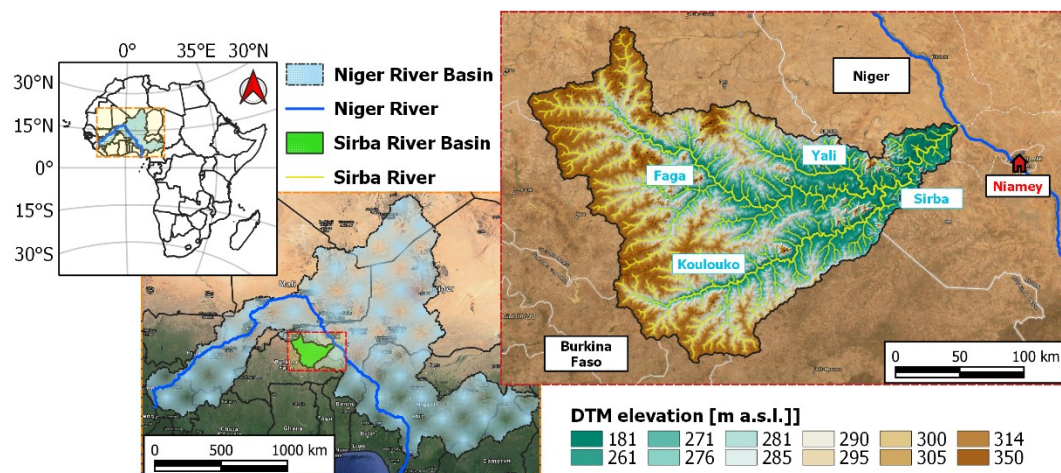


Figure 1.6 Geographical location of the Niger and Sirba River catchments. Enlargement: Sirba River hydrography and topography.

**11**

# 1.3 Objectives and outline

As described in the introductive overview, the Sahelian populations must continuously deal with natural hazards to defend their assets and livelihood.

The overall dissertation has several, but closely linked, objectives which go through the identification of lacks, the comprehension of the problematics and the assessment of proposed solutions. The relationship between issues and resolutions is displayed in Figure 1.7.

The research activities and achievements can be grouped into two main sub-research projects. The first study figures out the problem and embeds the preparing phases for the implementation of a flood management strategy, described in Chapter 2. The second provides methodologies for the investigation of proposed solutions and assessment of their performances, described in Chapter 3 and 4.

Chapter 2 collects all results achieved during the collaboration to the international cooperation projects ANADIA 2.0 [42]. The aim of the project is the development of an EWS against floods at the service of the riverine inhabitants of the Sirba River. The outcomes represent the hydraulic analyses carried out in preparation for the implementation of the system. Firstly, the revised and updated discharge time series of the Sirba River is provided. This dataset is then used to evaluate the hydraulic features and the level of flood hazard of the river. This package of preliminary information embodies the basis for the definition of different hazard scenarios and, consequently, the delineation of flood hazard maps.

Chapter 3 explores the capabilities of different indigenous RWHT to be adopted as non-structural flood mitigation techniques. The quantitative assessment of their hydraulic performances, meaning the efficiency in reducing runoff, is accomplished through advanced hydraulic modelling. In a first attempt, the hydraulic simulations are performed with the well-known hydraulic model HEC-RAS. The analyses focus on conceptual models, replicating the RWHT geometrical features, and the proposed methodology is then applied to a target watershed to show the effectiveness of such techniques in a real context. Subsequently, for overcoming the limitations observed from the use of a pure hydraulic model, a second numerical model, the two-dimensional distributed hydrological model Iber, is exploited to simulate the surface runoff processes.

Chapter 4 examines the benefits induced by the use of RWHT to cope with the rainwater shortage that characterizes the Sahelian climate. Eco-hydrological analyses show the impact of RWHT in minimizing plant water stress during the

growing season of typical Sahelian crops. In this section, a novel approach is proposed to compute the water balance assessment at the plot scale. The methodology seeks to minimize the number of inputs requested for the computation, dealing with the data scarcity that commonly contradistinguishes developing countries.

In the end, the dissertation concludes with chapter 5 in which the main research achievements are synthetically summarized. The chapter underlines the source of weakness of the current studies and suggests possible solutions and further developments that could foster future research endeavours.
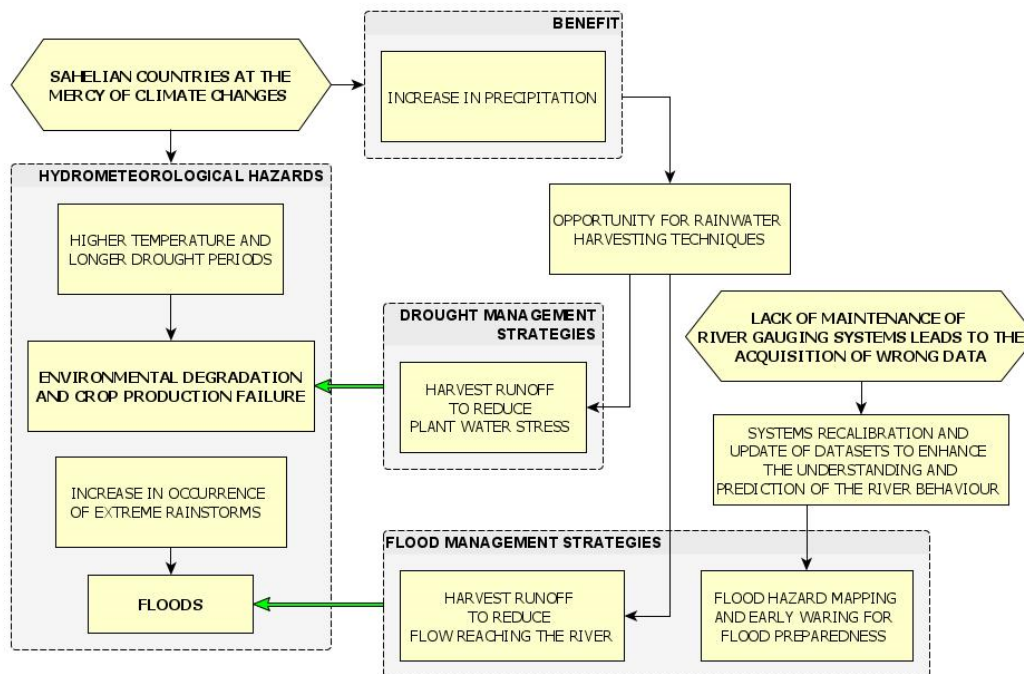


Figure 1.7 Conceptual workflow of the whole dissertation.

# Chapter 2

# Flood Hazard Alertness: preparation steps for an Early Warning System to protect African riverine inhabitants

*"Study the past if you would define the future."*

*Confucius*

## 2.1 Preface

The work described in this chapter has been partially derived from papers "*Hydrology of the Sirba River: Updating and Analysis of Discharge Time Series*" and "*Flood Hazard Scenarios of the Sirba River (Niger): Evaluation of the Hazard Thresholds and Flooding Areas*" both published in Water [26,38].

People living in Sahelian regions are continuously affected by catastrophic floods which are becoming, year after year, more frequent and severe as a consequence of climate changes and environmental degradation. Despite the effort in preventing these hazards, the consequences are still exacerbated by the incessant population growth and the persistent increase of hydroclimatic extremes. Hence, the development of flood risk management strategies aimed to mitigate the negative impacts or improve the degree of adaptation, enhancing the resilience of the populations, has become the crucial purpose for sub-Saharan nations. These strategies can be structural, such as the realization of dams, levees and diversions, or non-structural, such as land-use planning, flood forecasting, flood risk assessment and Early Warning Systems (EWS). The implementation of such strategies requires a deep knowledge of the behaviour of the river, its hydrology, and all activities that take place along the riverbanks and floodplains. This latter aspect is particularly significant in African rural areas, where many agropastoral activities, forms of subsistence and important assets (e.g. water pumps) are located close to the river.

This chapter expounds all the preliminary hydrological and hydraulic investigations carried out during the implementation of the first EWS on the Nigerien reach of the Sirba River, called SLAPIS (Système Locale d'Alerte Precoce contre les Inondations de la Sirba) [108]. The local EWS has been conceived and developed within the ANADIA 2.0 Project (Adaptation to Climate Change and Disaster Risk Reduction for Food Security—Phase 2); project founded by the Italian Agency for Development Cooperation. Many partners collaborated to meet the goal between:

- Nigerien partners: National Directorate for Hydrology and the National Directorate for Meteorology;
- Italian partners: Politecnico and Università di Torino and the National Research Council.

The preliminary investigations concerned the revision and update of flow time series, the evaluation of hazard thresholds and the identification of flood-prone

areas identified through the delineation of flood hazard maps. The followed workflow is displayed in Figure 2.1.

First of all, reliable data and continuous dataset are needed to perform hydrological or statistical analyses and achieve robust results. Unfortunately, these datasets often present gaps caused by lack of maintenance or failures of gauging stations. Or they are affected by wrong records induced by obsolete rating curves that lead to an erroneous transformation from water depth to flow rate.

The first part of the study focuses on the critical examination of the existing river flow data of the Sirba River and provides a revised dataset for the stream gauge station of Garbey Kourou. Working at the sub-basin scale, a significant mismatching in river discharge was noticed due to the evident differences between the flow rate calculated with the current rating curve and the discharge measured on-site. Thus, the revision and recalibration of the set of rating curves were essential to obtain the correct correlation stage/discharge and provide a revised and more reliable discharge time series of the river.

The revised time series states a reliable new starting point for every future analysis. In particular, it becomes indispensable during the calibration phases of data-based and modelling approaches. Additionally, the revised flow time series allowed the revaluation of some important hydraulic features, such as the flow duration curve and trends, useful for improving the comprehension of the river. The results confirm and strengthen previous research's findings. The flood frequency and intensity are characterized by a marked positive trend over the entire analysed period 1956-2018. This positive trend is much more pronounced for the last 20 years, asserting a period of recurring dangerous natural phenomena. Moreover, a new changepoint in the time series was detected in correspondence of the year 2008, which represents the beginning of the period where the highest flood magnitudes were registered.

The second part of the study deals with the flood hazard assessment of the most populated reach of the Sirba River. This reach stretches for 108 km from the state border between Niger and Burkina Faso to the confluence into the Niger river. The assessment execution embeds by two main steps: the definition of hazard thresholds, i.e. the configurable hazard scenarios, followed by the demarcation of the spatial limits characterized by a certain level of hazard.

The hazard scenarios were configured matching the flood hazard categorization, currently in force in the Niger state, with defined hazard thresholds. The hazard thresholds were set as the range of discharge comprised between 4 design floods. The design flood can be expressed as the amount of

discharge related to a specific frequency of occurrence, i.e. flood return time. The entity of such discharge is generally estimated through statistical inference on the time series of recorded data. As argued by Paturel et al. [109,110] and confirmed by the insights came out in the first part of the study, it is necessary to choose a methodology able to take into account the non-stationarity of the hydrological variables. This necessity is more evident in observing the future scenarios showed by climate projections [16]. Thus, the present study exploits the novel methodology introduced by Wilcox et al. [111] to quantify design discharges related to different return times.

For each hazard scenarios, the delineation of the flood-prone areas was achieved through the implementation of a nondimensional hydraulic numerical model of the entire river. The use of hydraulic numerical models is a consolidated practice utilized by river engineers to predict the potential inundation extent and plan the emergency procedures in case of crisis [112–114]. Each simulation revealed the riverine areas potentially interested by the water flowing out of the river banks and allowed to classify each zone in flood hazard maps. These maps are also a precious tool for the administrations and citizens themselves, in order to achieve a conscious use of the territory. The hydraulic model was also used to furtherly validate of the rating curves in correspondence of the two main gauging sites of the Sirba river.

All the outcomes have had strategic importance in the implementation of the EWS for the flood alert at the service of riverine inhabitants of the Sirba river. A brief analysis of the extraordinary wet season 2020 is also reported, where the system has had its first actual test.
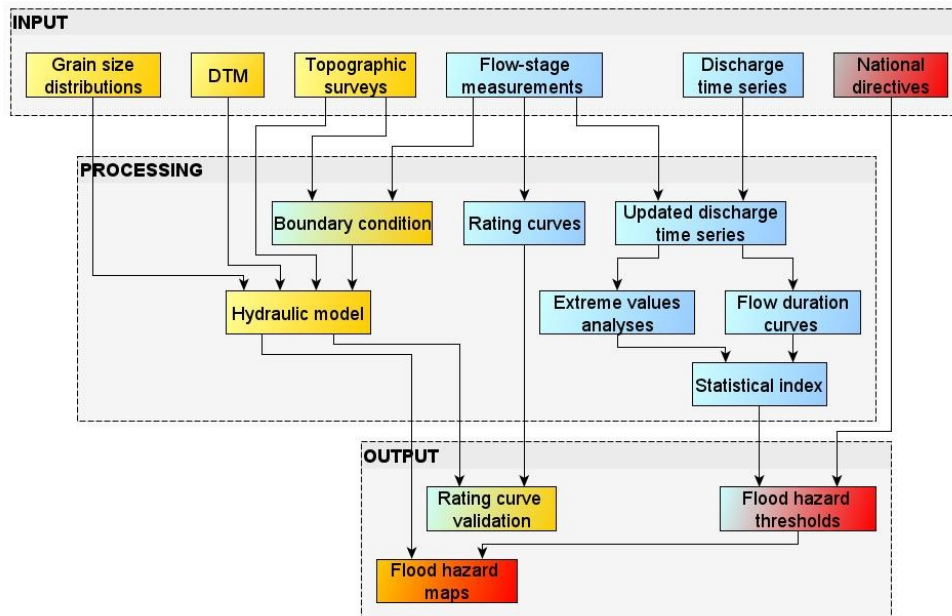
Figure 2.1 Workflow: Data collection (input); elaboration of collected data (processing) and outcomes of the work (output). Colouring: geometrical data (yellow), hydrological data (blue), and local legislation (red).

## 2.2 Rating curves

### 2.2.1 Gauging stations and datasets

The Sirba river basin is nestled in the core of the Middle Niger River Basin (MNRB) and its water flows into the Niger river almost fifty kilometres upstream of the Nigerien capital, Niamey. Several hydrometric stations are installed in this vast area for monitoring the flow rate and checking the water balance over the hydrographic network.

The system of discharge monitoring of the Sirba river is, today, composed of a total of five gauging stations in which the water depth is recorded. Three are located in the Burkinabe part of the basin and they are respectively installed on each one of the tributaries: on Koulouko river at Bassieri, on Faga river at Liptougou and Yali river at Sebba. These are manual stations, so the water depth is registered by a specialized observer every day and then the records are transmitted to the river authority.

Instead, the Nigerien part is instrumented with two automatic hydrometric stations. The most important is the gauging station of Garbey Kourou sets at the outlet of the basin. It was installed in 1956 and it is placed 8 km upstream of the

confluence into the Niger River. The gauging station is equipped with 6 staff gauges (0-600 cm) and two water pressure measuring devices controlled respectively by Niger Basin Authority (NBA) and General Water Resources Management (DGRE, Direction Générale des Ressources en Eau) of the Republic of Niger. The newest station was installed in correspondence of the village of Bossey Bangou, few kilometres downstream the border with Burkina Faso, in June 2018. This intervention was accomplished to set up the observation system needed for the early transmission of flood warnings. This station is equipped with 8 staff gauges (0-800 cm) and a water pressure measuring device, managed by DGRE.

In the hydraulic junction Sirba-Niger, others two gauging stations are installed on the Niger river. From the confluence is it possible to identify the hydrometer of Kandadji, upstream, and the station of Niamey, downstream. Between them, a minor tributary flows into the Niger river just a few kilometres north of Garbey Kourou. This is the Dargol river whose flow rate is measured at the gauging station of Kakassi.

The aforementioned gauging stations are listed in Table 2.1 and displayed in Figure A.1.

Table 2.1 Gauging stations included in the area pertaining to hydraulic junction Sirba-Niger. Between brackets, the acronyms that will be used along the text to identify the Bossey Bangou and Garbey Kourou gauging stations.

| Country | River Basin | River | Gauging station | Basin area subtended [Km$^2$] |
|---|---|---|---|---|
| Niger | Niger | Niger | Kandadji | 633'000 |
| | | | Niamey | 700'000 |
| | Dargol | Dargol | Kakassi | 6'940 |
| | Sirba | Sirba | Bossey Bangou (BB) | 37'000 |
| | | | Garbey Kourou (GK) | 38'750 |
| Burkina Faso | | Yali | Sebba | 2'280 |
| | | Faga | Liptougou | 15'700 |
| | | Koulouko | Bassieri | 8'000 |

The series of records have been collected for all these stations. Except for the new Bossey Bangou station, the observed river stages and discharge at the daily resolution were obtained from the database of NBA and DGRE. Additionally, scrupulous research was carried out to find all the discharge measurements realized on-site covering the period 1956-2018.

The main attention was focused on the Garbey Kourou gauging station since it defines the effective amount of water that flows out of the Sirba basin. The analysis of the stage and discharge time series spans over an observation period that ranges from the year of the installation in 1956 until 2018. In this temporal range, a vast set of 140 on-site measures was collected and it involves measurements derived from NBA (91), the Monographie hydrologique du fleuve Niger (39) [115], and recent measurements managed by the DGRE (3). Moreover, other 7 measurements realized during survey campaigns within ANADIA 2.0 project. These last seven measures were realized using an Acoustic Doppler Current Profiler and GPS devices in the wet season 2018.



Figure 2.2 Flow measurement campaigns in September 2018. The figures show the devices used during the on-site measurements.

In the same season, the same number of measurements have been carried out also in the new BB gauging site.

The discharge time series for the gauging stations of Niamey, Kandadji and Kakassi were provided by DGRE for the period 2006-2017.

The further data collected were the three rating curves (RC) adopted by the DGRE to transform the water depth measured by the water pressure sensors in discharge for the GK station. From 1956 only two updates have been completed: the first one in 1976 and the last dates back to 80s. Hence, the range of validity of each RC is: (1) 1956-1976, (2) 1977-1979 and (3) 1980-up to now.

In addition to the GK rating curves, the RC of the other gauging stations of the hydraulic junction Sirba-Niger where collected.

## 2.2.2 Rating curves revision and recalibration

### *Garbey Kourou rating curve*

Three different rating curves have been used during the 63 years of measurements and the last dates back to 1980. The on-site discharge measurements realized at GK observation site have shown how the application of the current rating curve was causing a significant underestimation of the streamflow (Figure 2.3).
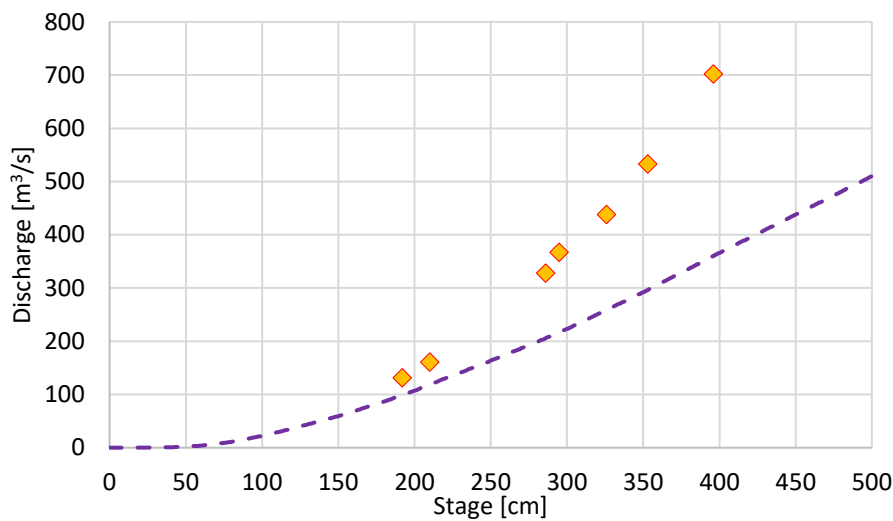


Figure 2.3 Comparison between more recent on-site measurements (orange dots) and RC currently used by the DGRE (violet dashed line).

During land surveys, we noticed that many human activities are digging the riverbanks leading to deep morphological changes. These modifications have altered the geometry of the river cross sections and therefore the hydrodynamic features of the river. Therefore, such changes potentially explain the unsuitability of the current RC and confirmed the necessity of an urgent recalibration.

The set of 140 measures allowed to revise the existing rating curves obtaining a new set of them. The new three RC were calculated using a homogeneous set of data dived in 3 intervals of validity: 1956-1978 (based on 84 measures), 1979-2003 (based on 39 measures) and 2004-2018 (based on 17 measures). The breakpoint of each interval was set up in correspondence of gaps into the measurement set. The reason why the last update is so old can be found in the decreasing number of on-site measures made over time. This aspect underlines the insufficient effort put on river monitoring and lack of a systematic plan of revision and verification.

The stage/discharge rating curves were calculated for each interval, following a power-law with two parameters [116,117]:

$$Q = a \cdot h^b \tag{2.1}$$

where $a$ and $b$ are the coefficient and the exponent that define the shape of the curve, respectively, $h$ is the stage height [m] and $Q$ is the discharge [m$^3$/s]. Taking the logarithm of each on-site measure, the coefficients were extracted by linear regression of the logarithm plot, which maximizes the coefficient of determination $R^2$

$$\log Q = \log a + b \cdot \log h \tag{2.2}$$

In order to distinguish between old and new results along with the text, the previous rating curves will be called "DGRE RC", while the recalibrated rating curves will be referred to as "ANADIA RC".

The outcomes of the linear regression analysis are displayed in Figure 2.4.
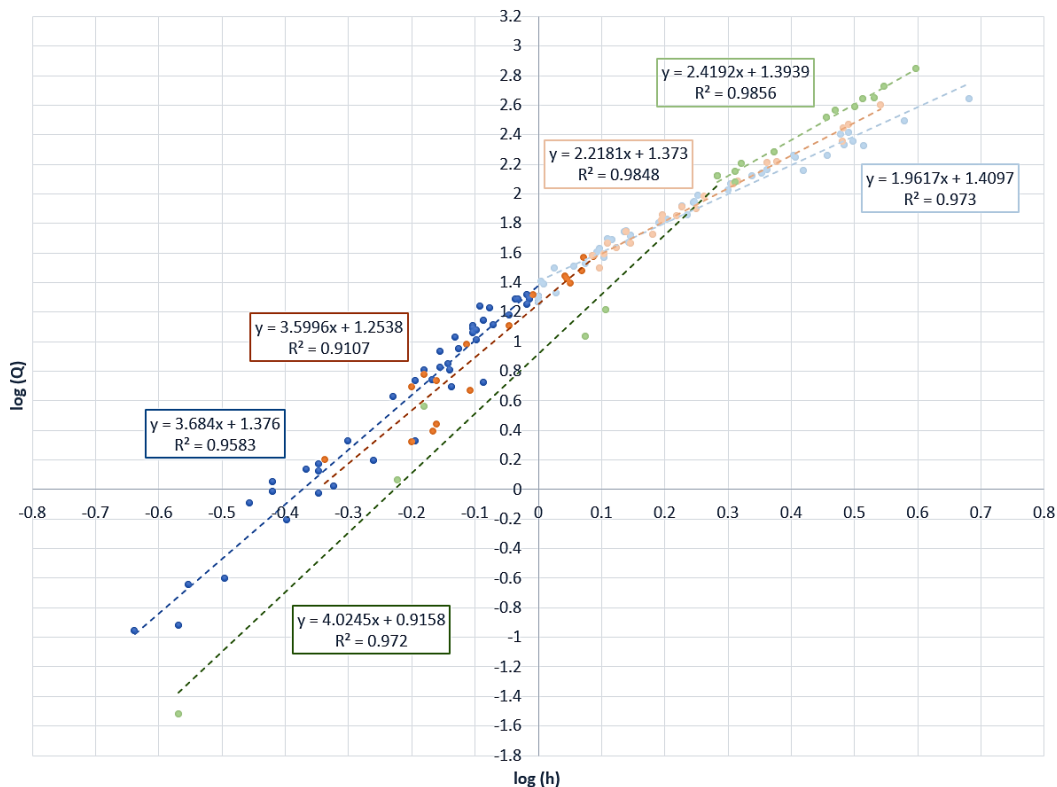


Figure 2.4 Logarithmic plot of the 140 on-site measurements (dots). The three intervals of validity are identified with different colours. Blue for the interval 1956-1978, orange for the interval 1979-2003 and green for the interval 2004-2018. Dashed lines represent the linear fitting lines. The lines' equations and the relative coefficient of determination are reported into the coloured boxes.

To find the best fitting, and therefore generate more representative RC, the entire set of measurement was divided into two ranges aimed to optimize the value of $R^2$.

The ranges of validity, coefficients and exponents of the new rating curve equations are summarized in Table 2.2. The upper limit of each range represents the highest stage measured during that interval; hence, the limit until the RC can be considered reliable.

Table 2.2 Parameters of the recalibrated rating curves, ANADIA RC, for the Garbey Kourou gauging station.

| ANADIA RC | Ranges [cm] | a | b | $R^2$ |
|---|---|---|---|---|
| 1956-1978 | [0 – 100) | 23.769 | 3.684 | 0.958 |
| | [100 – 500] | 26.914 | 1.908 | 0.976 |
| 1979-2003 | [0 – 130) | 17.570 | 3.545 | 0.927 |
| | [130 – 350] | 24.155 | 2.191 | 0.985 |
| 2004-2018 | [0 – 190) | 8.238 | 4.025 | 0.972 |
| | [190 – 400] | 24.769 | 2.419 | 0.986 |

In Figure 2.4 an unexpected trend can be noticed. In correspondence of lower stages, for the same water depth, the river shows a lower discharge in the recent interval than in the older ones. Indeed, the green dashed line lays under the blue dashed line. Conversely, for higher stages, the opposite order can be highlighted. This means that, for an equivalent water depth, in the river flows a much higher discharge (since it is regulated by a power-law) in recent times than in older ones. This is also emphasized in Figure 2.6, where the three RC are drawn.

This trend reflects the evolutive changes in the hydrodynamics of the river over time. The river is a natural environment subjected to continuously natural or artificial morphological alterations which determine a constant changing of its hydraulic behaviour. In particular, progressive enlargement of cross sections of the river has been observed, just downstream of the gauging site, caused by flow erosion processes and intense digging activities along the banks (Figure 2.5).

Figure 2.5 Alluvial erosion and digging activities along the Sirba riverbanks nearby Garbey Kourou. (Photo credit: Giovanni Massazza, left, and Paolo Tamagnone, right).

A considerable difference in the relation stage/discharge is displayed overlapping the updated ANADIA RC on the previous DGRE RC (Figure 2.6). all the old RC are lower than the recalibrated ones, and the mismatching increase over time. The comparison is reliable even though the temporal intervals are not perfectly paired.
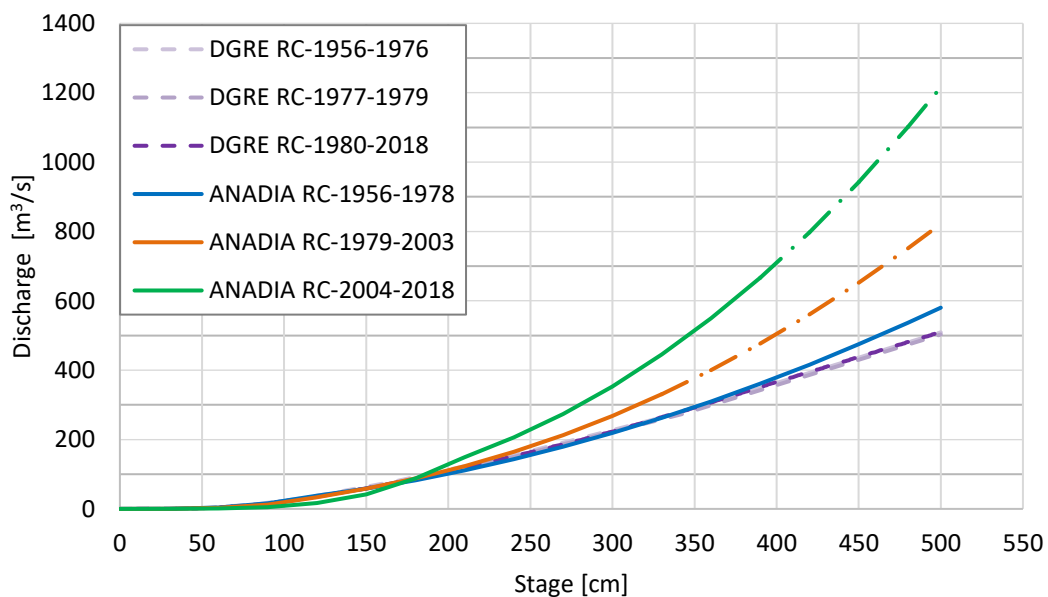


Figure 2.6 Comparison between ANADIA RC (solid lines up to the limit of the validity range, then dot-dashed lines up to 5 m) and DGRE RC (dashed lines).

Considering the interval of validity until 1978, there is not a significant discrepancy between the two curves. The only difference lies in the linear regression approach followed in the calculation of the equations' parameters. The DGRE uses the entire set of stages for the fitting, instead, we considered two stage ranges. This latter approach better fits the real correlation stage/discharge of the analysed cross-section of the river, but it also introduces a slight uncertainty in the calculation of the flow rate in correspondence of the transition from one range to

**25**

the next. For this reason, in Table 2.2, square and round brackets define the range's limits and indicate which equation should be used for each stage.

As regards the second period (1979-2003), the new rating curve (orange solid line) shows a trend significantly different compared to the old curve (violet dashed line). Focusing on the last period (2004-2018), the updated RC (green solid line) is totally divergent from the DGRE RC for stages higher than 2 m. At the upper limit of the validity range, i.e. 4 metres, the discharge measured with ANADIA RC is almost two times greater than the one calculated with DGRE RC.

### *Bossey Bangou rating curve*

This gauging station was installed before the rainy season 2018 and no previous measurements were conducted in this site. Thus, the only dataset that allowed to calculate the relation between stage and discharge is the set of discharge measurements realized between June and August of the same year.

Using the same approach explained for the GK RC, the parameters of the RC equations were extracted through linear regression.
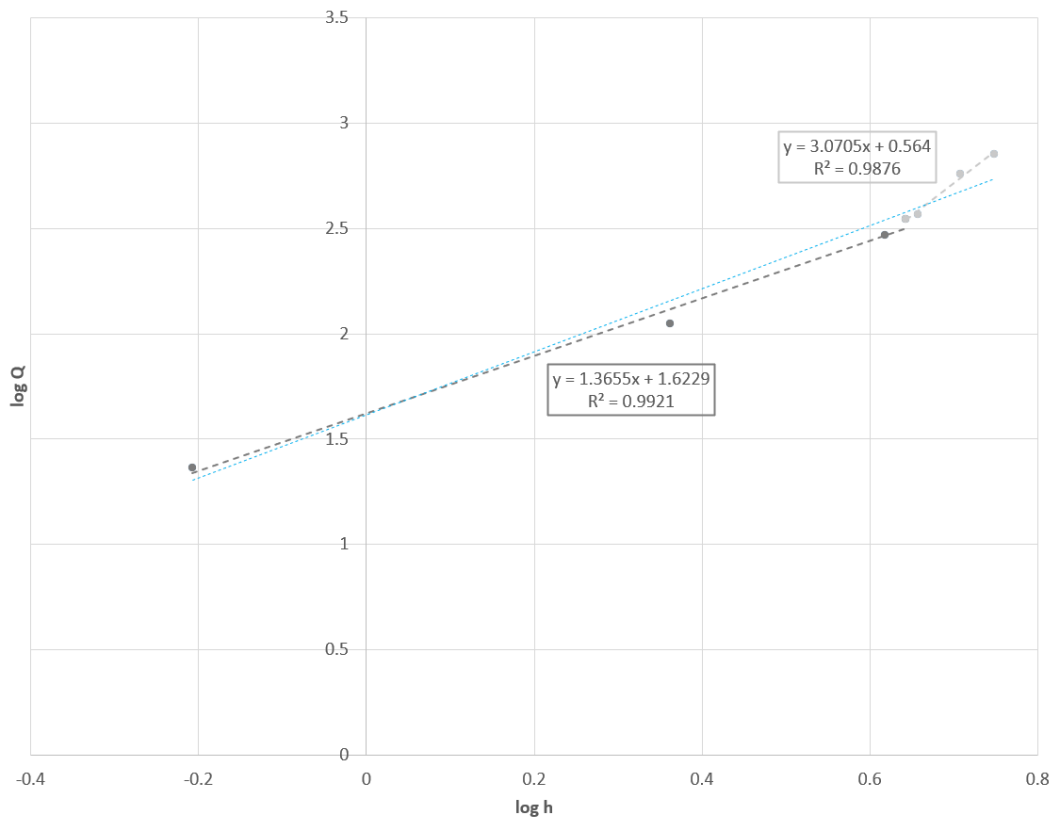


Figure 2.7 Logarithmic plot of the 7 on-site measurements (dots). Dashed lines represent the linear fitting lines. Grey lines are the fitting lines for the two ranges identified, whereas the blue line is

**26**

the fitting line without the optimization. The lines' equations and the relative coefficient of determination are reported into the coloured boxes.

Observing the trend of the grey fitting lines, it is clear how the relation stage/discharge has a different pattern as the water depth increases. This is because, at least in the analysed reach, the Sirba riverbed is devoid of defence works or embankments that avoid the outflowing of floodwater. Thus, when the level rises and overcomes the riverbanks, the discharge noticeably increases against a slight increase in water depth. For this reason, once identified the change point, a rating curve optimized over two ranges can better simulate the correlation stage/discharge. Indeed, without such optimization, hence a linear regression over the entire dataset (blue dashed lines, Figure 2.7), the RC curve appears much flatter. This shape would lead to an overestimation of the flow rate for low levels, and a strong underestimation for high stages (see Figure 2.8).

The equation thus calculated represents the first rating curve of Bossey Bangou (BB) observation site. The ranges of validity, coefficients and exponents of the rating curve equation are summarized in Table 2.3.

Table 2.3 Parameters of the rating curve for the Bossey Bangou gauging station.

| BB RC | Ranges [cm] | a | b | $R^2$ |
|-------|-------------|-----|-----|-------|
| 2018 | [0 – 440) | 41.965 | 1.366 | 0.992 |
|      | [440 – 600] | 3.664 | 3.071 | 0.988 |
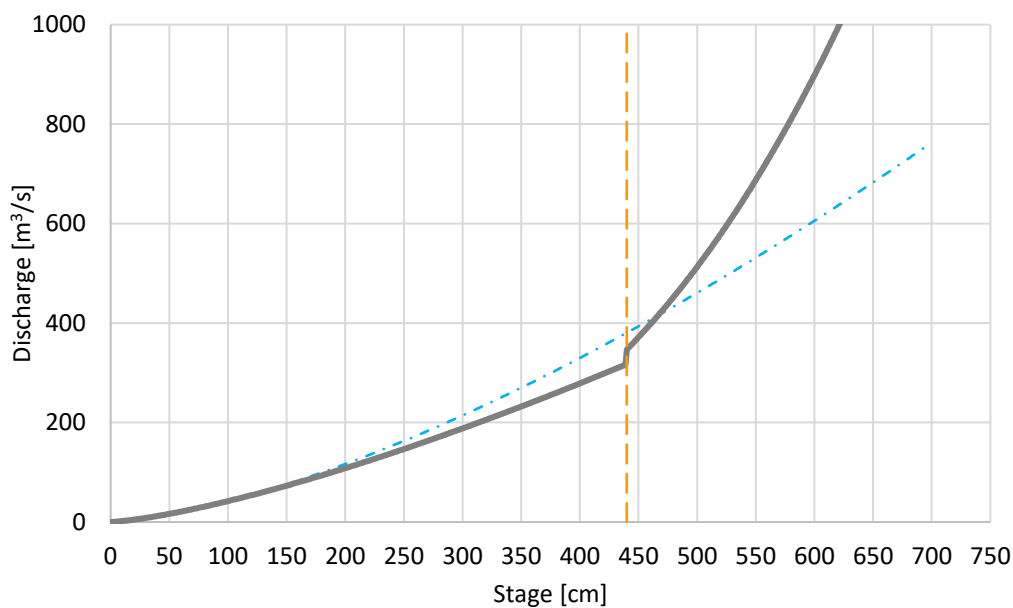


Figure 2.8 Bossey Bangou RC (solid grey line). The dotted-dashed blue line represents the RC without optimization. The dashed orange line indicates the changepoint between the two range of validity.

**27**

The small size of the dataset does not allow to define a smooth curve over the entire range of stages. Indeed, in correspondence of the transition from the equation that controls the lower and the upper part of the RC, a discontinuity is present. This step could lead to an uncertainty of almost 30 m$^3$/s, however lower than 10%.

This point of weakness highlights the necessity of further and frequent measure campaigns, in order to enlarge the dataset and improve the delineation of the RC.

### *Revision of the rating curves of the gauging stations of the hydraulic junction Sirba-Niger*

From the experience gained regarding the troubles concerning the rating curves of Garbey Kourou, the revision of the gauging sites of Kakassi, Kandadji and Niamey was carried out.

For the Kakassi station placed at the outlet of the Dargol river basin, a total number of 69 discharge measurements was collected from the Monographie hydrologique du fleuve Niger. Despite the relevant number of data, this set dates back to campaigns did between 1957-1978. Unfortunately, no updated data were found to evaluate the reliability of the current RC. However, conversely to the GK RC, this curve was updated at the beginning of the present century. Looking at Table 2.1, the Dargol basin is considerably smaller than the others basins analysed, and therefore it slightly affects the overall water balance of the junction.
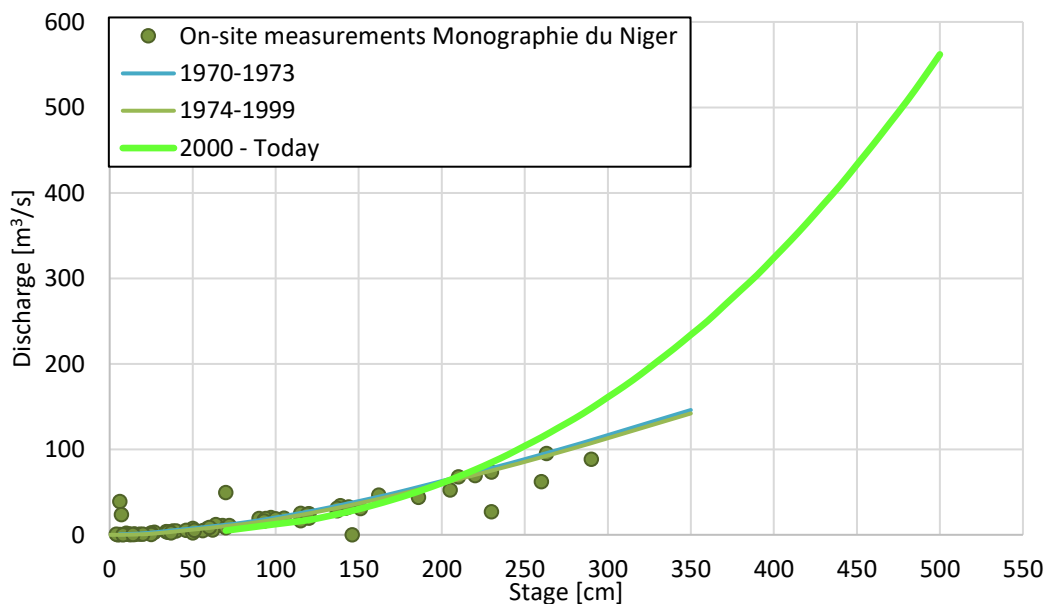


Figure 2.9 Kakassi RC of the Dargol river. The current RC is marked with green light colour.

Focusing on the main river, the Niger river, the Kandadji gauging station accounts for the inflow, whereas the Niamey gauging station checks the outflow from the hydraulic junction Sirba-Niger.

Starting from upstream, for the Kandadji gauging station, a series of 22 measurements were collected including two more recent on-site investigations realized in the years 2015-2016. The river features seem to be stable at this site and not affected by boundary conditions. Indeed, the latest investigations are roughly well aligned to the RC and confirm that it is still reliable, even though it dates back to 1979.
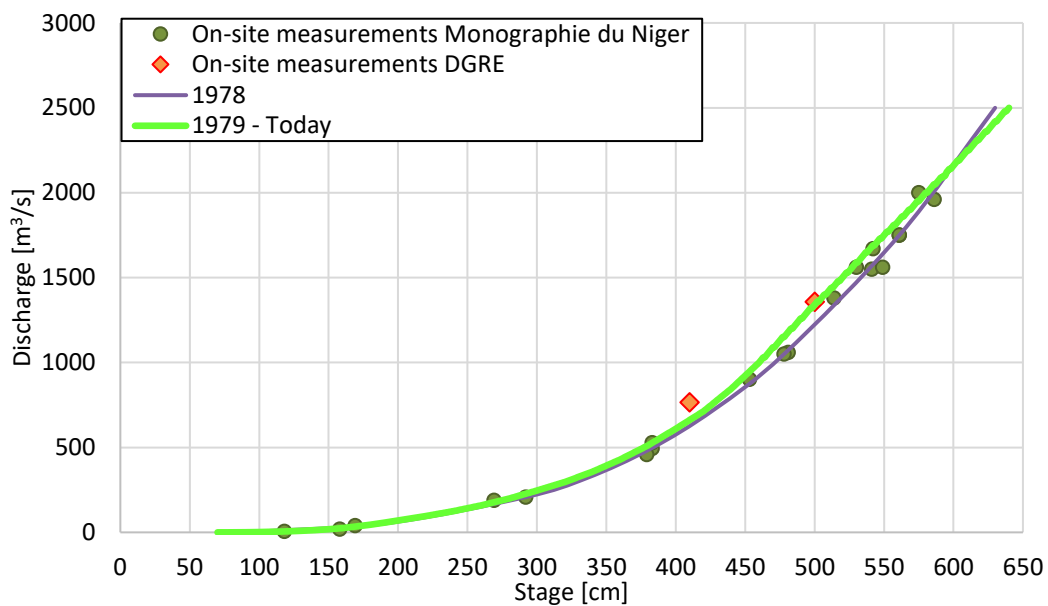


Figure 2.10 Kandadji RC of the Niger River. The current RC is marked with green light colour.

Finally, downstream the confluence of the Sirba river into the Niger river, there is the most important gauging station located at the Nigerien capital, where the river laps at the city. The set of measurements collected counts 236 observations with the most recent carried out in June 2018.

Conversely to the Kandadji station, the Niamey RC show an evolutive pattern in which, for the same discharge, the water level is higher in recent times than seventy years ago. This could be due to several modifications that altered the river morphology and its hydrodynamics during the last fifty years. Examples are the building of the Kennedy Bridge (1970), the China-Niger Friendship Bridge (2011) and now a third bridge is under construction in the northern part of the city. However, these changes have been well tracked simultaneously with a constant update of the RC. These efforts have guaranteed the use of a reliable relation

**29**

stage/discharge over time. The continuous expansion of the city brings the need for constant monitoring and update of this system.
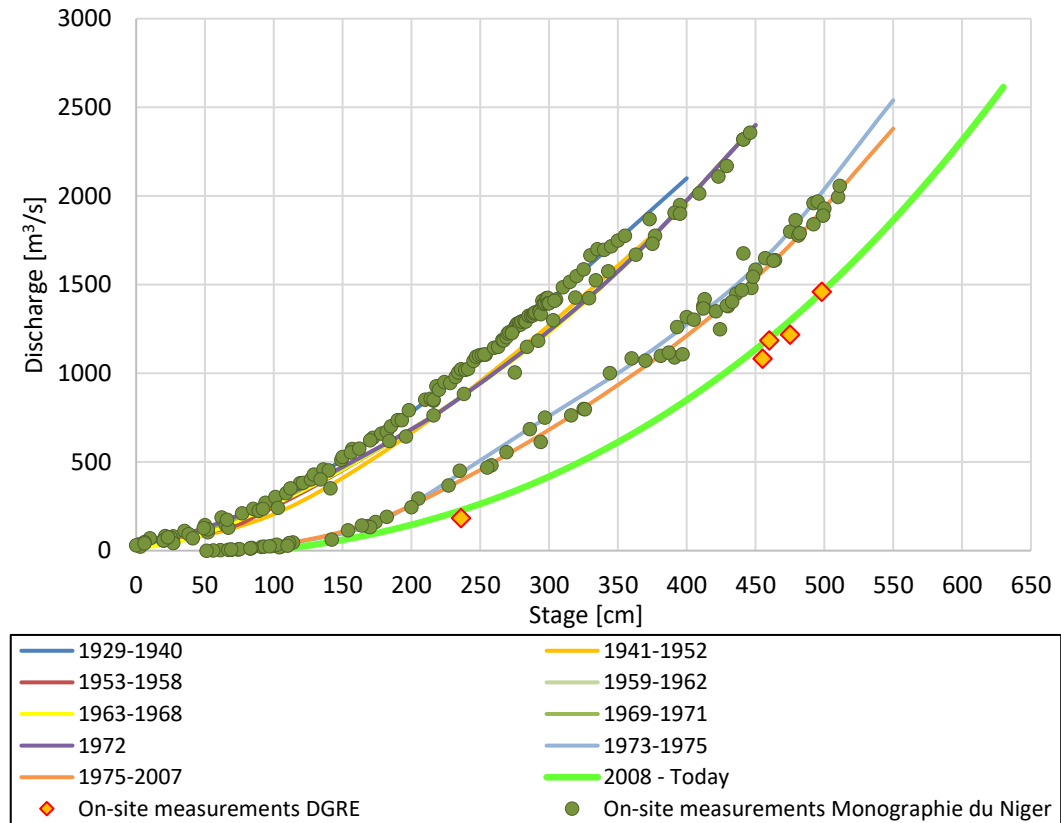


Figure 2.11 Niamey RC of the Niger River. The current RC is marked with green light colour.

## 2.3    Flow time series

Once defined the GK RC equations representative of each interval identified, they have been applied to recalculate the discharge associated with the recorded river stages. This step assumes the reliability of the water depth measured over time. The outcome provides a new time series of discharge which will represent a new milestone for the forthcoming analyses on the Sirba river.

As previously done, the old discharge time series will be called "DGRE time series", while the updated time series will be referred to as "ANADIA time series".

Comparing the two datasets (Figure 2.12), it is noticeable the sharp increase in discharge estimation bonded to the recalibrated RC. Considering the last severe flooding events occurred in the last twelve years, the DGRE strongly underestimated the flow peak that effectively flooded a vast portion of the Sirba's

floodplains. The gap between the two datasets overcomes 600 m³/s for the main floods and more than 800 m³/s for the most severe flood in 2012.
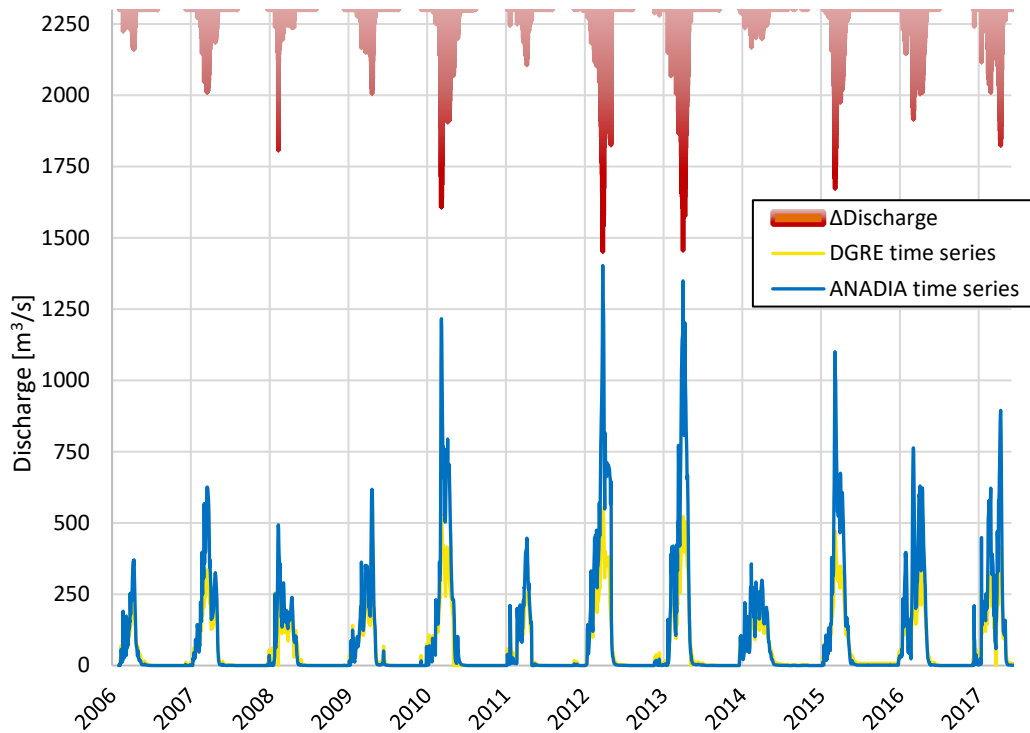


Figure 2.12 Comparison between DGRE and ANADIA time series for the last decade 2006-2017. ΔDischarge highlight the gap between the new dataset and the old ones (colouring: from -100, light red, to 850, dark red).

In order to assess the reliability of such results, the focus was moved out of the studied domain, evaluating how the new discharge modify the water balance of the hydraulic junction Sirba-Niger.

So far, the NBA was burdened with a doubt: *Why the water balance between Kandadji and Niamey, after subtracting the discharge of the two main tributaries (Dargol and Sirba), is still largely positive?* This incongruence was primarily examined by the research group of Luc Descroix [28] which tried to find an explanation in the strong increase of runoff coefficients in the middle Niger River tributaries and endorheism breaking of some minor valleys. Now, the recalibration of the GK RC and the increase in the flow rate calculation partially answer the NBA's query.

The revision of the water balance of the twelve-year period 2006-2017 was performed. Over the analysed period, the discharge and the related water volume flowed in each gauging station of the hydraulic junction was calculated.

The water balance was calculated as the difference between the annual volume that flows out of the hydraulic junction at Niamey and the cumulative

volume that flows through the upstream gauging stations of Kandadji, Kakassi and Garbey Kourou. Table 2.4 illustrates the gap existing between the inflow and the outflow water volume at Niamey station. With the revised discharge time series, this gap is reduced from 2.98 $Km^3$ to 1.84 $Km^3$, in percentage from 9.59% to 5.94%, respectively, of the annual volume of the Niger River at Niamey.

Table 2.4 Annual volume ($V_{annual}$) for the different gauging stations over the period 2006-2017. The discrepancy represents the differences between the inflow and outflow water volume at the Niamey stations.

| Gauging Station | River | $V_{annual}$ [km³] | |
|---|---|---|---|
| | | DGRE | ANADIA |
| Niamey | Niger | 31.01 | - |
| Kandadji | Niger | 25.54 | - |
| Kakassi | Dargol | 0.46 | - |
| Garbey Kourou | Sirba | 2.02 | 3.16 |
| Upstream Sum (Kandadji + Kakassi + Garbey Kourou) | | 28.03 | 29.17 |
| Discrepancy (Niamey – Upstream Sum) [%] | | 9.59 | 5.94 |

Looking at the water balance year by year (Figure 2.13), some consideration can be advanced. Despite the remaining water balance is still positive, except in 2013, the gap is significantly reduced with the introduction of the ANADIA time series. This means that effectively an underestimation of the discharge was in progress. The major differences correspond to those years when extreme flooding events have occurred, and therefore where the main contribution of the ANADIA RC affects the discharge calculation, stating the underestimation of those floods. The gap is minimized in those years with a value lower than 0.5 $Km^3$ in 2012 and 2013, whereas is considerably reduced for 2010 and 2015. The negative value of 2013 could be presumably related to high evaporation and infiltration losses occurred in that year.
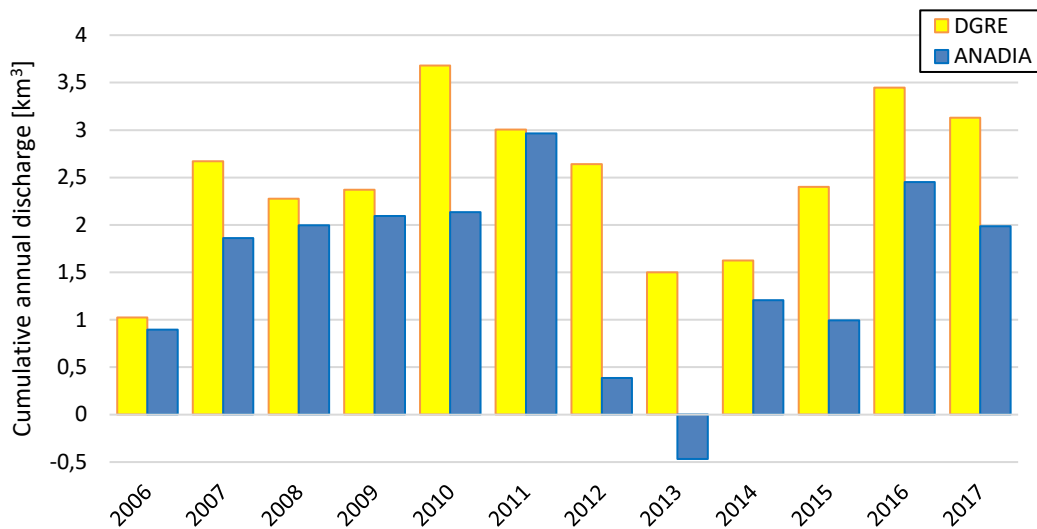
Figure 2.13 Comparison between the water balance calculated with the DGRE and with the ANADIA discharge time series of the Sirba River for the period 2006-2017.

The further confirmation of the validity of the proposed discharge time series can be highlighted superimposing the hydrographs of the rivers coming from upstream over the hydrographs measured at Niamey. Focusing on the year 2012, when the most severe flood ever registered up to that moment occurred, it is possible to analyse the contribution of each basin (Figure 2.14).
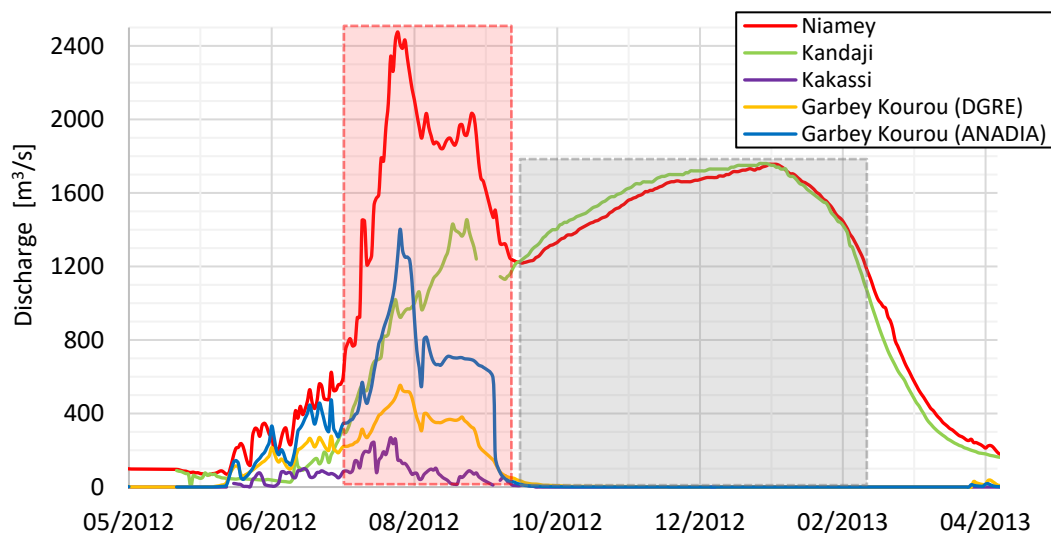


Figure 2.14 Flood decomposition between different inflows. The red shaded area covers the section of the Niger hydrograph called "Sahelian or red flood", whereas the grey shaded area embeds the "Guinean or black flood".

The updated discharge time series justifies the marked rise of the red flood, showing how the contribution of the Sirba river accounted for more the half of the flood wave that hit the Nigerien capital during the wet season 2012. The changes in the hydraulic response to extreme events of Sahelian tributaries explains the

**33**

ongoing exacerbation of the red floods against a negative trend of the intensities of black floods.

Combining all upstream flows, the good alignment of the curves delineated in Figure 2.15 state the effectiveness of the ANADIA time series. The updated time series perfectly fill the gap of the old time series, especially for the Sahelian flood (July-September). Deviations can be attributed to boundary conditions: outflowing fluxes (infiltration and evapotranspiration), inflows from unmonitored small tributaries [32] or the effect of flood retention areas. In Figure 2.15 it is roughly evident that the losses and flood retention related effects are sharper during the Guinean flood, whereas contributions from other tributaries are predominant during the Sahelian flood.
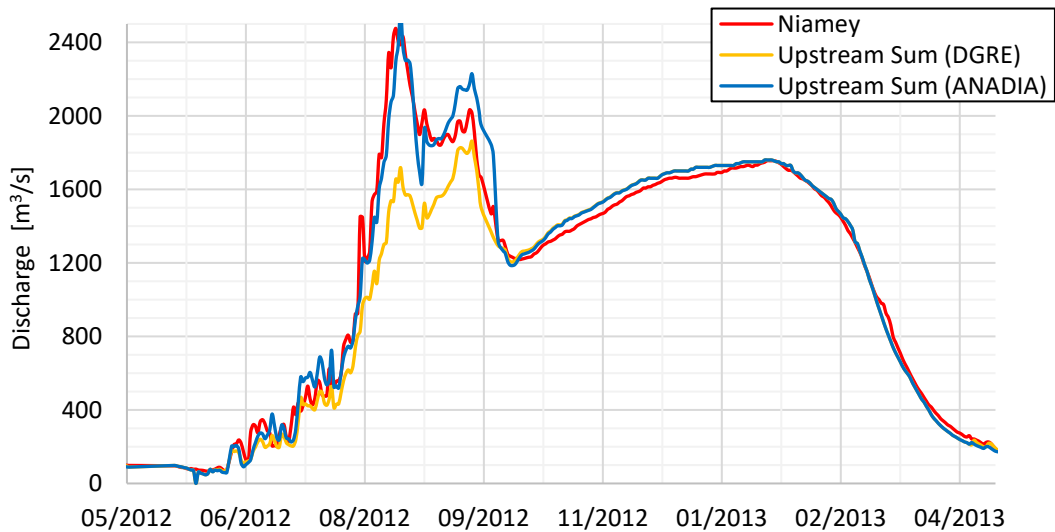


Figure 2.15 Hydrograph at Niamey (red line), the cumulative contribution of the of Niger (measured at Kandadji), Dargol (measured at Kakassi) and Sirba (measured at Garbey Kourou) with the ANADIA discharge (blue line) and with the discharge from DGRE (yellow line).

The alignments for the investigated period 2006-2017 are shown in Figure A.2 (see Appendix A)

Further studies should focus on the comprehension of the effective contribution of other small tributaries, tracking the behavioural shift of small basins from endorheic to exorheic and quantifying their runoff. The previous section revelated that Kandadji and Niamey RC are still reliable, whereas Kakassi RC would require a new campaign of discharge measurements in order to assess its effective quality.

## 2.4    River flow regime

On the base of the updated discharge time series, the hydrological regime of the Sirba river was recalculated in order to observe the basin's response to climate and environmental changes occurred during the last 60 years.

### 2.4.1  Annual extremes

The first feature analysed is the distribution of the annual maximum discharge (AMAX) over time. The AMAX time series is displayed in Figure 2.16. The values of AMAX were picked up only for those years without measurement gaps during the central months of the wet season. This precaution makes the selection more robust and avoids potential underestimation since the most severe floods generally occur between August and September [111]. In these months, especially in August, it is concentrated most of the total annual precipitation. As result, 8 out of 63 years have been removed from the time series (1959-1961, 1991, 1997, 2000, 2004-2005).
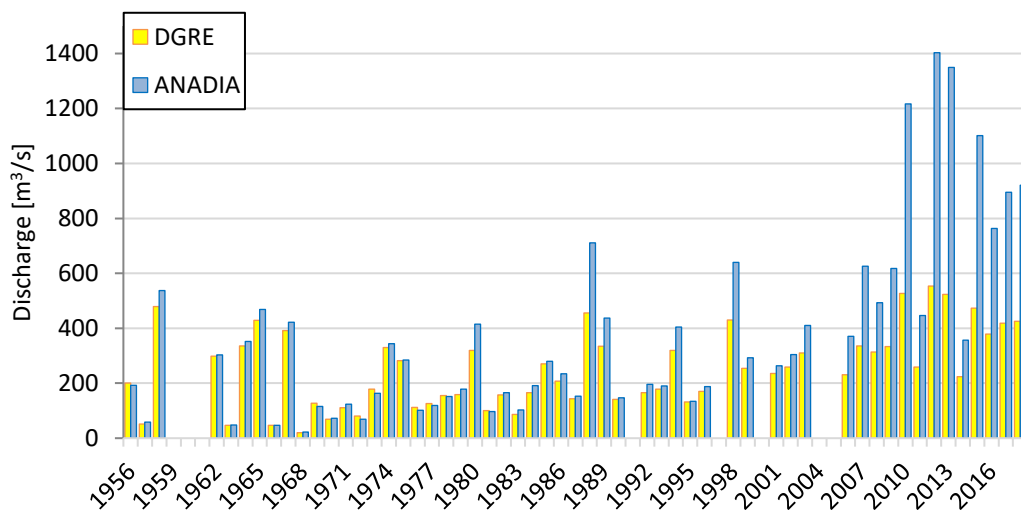


Figure 2.16 Comparison between the AMAX time series evaluated with the DGRE time series (yellow bars) and ANADIA time series (blue bars).

The ANADIA AMAX time series highlights a marked evolution of the flood magnitude over time. The evident positive trend states the strong non-stationarity of this distribution of data. From a first glance, different time-ranges characterized by a specific flow pattern can be identified. The limits of each range were evaluated pinpointing the changepoints of the dataset. To detect the abrupt changes into the time series, the approach developed by Wang [118,119] based on

**35**

the Penalize Maximal Function Test was used (analysis performed by Velia Bigi using RClimDex). Three changepoints were detected in correspondence of the years 1968, 1989 and 2008 (Figure 2.17). The first two values are consistent with those of other previous studies [34,72] which found almost the same changes into the dataset. The first changepoint in 1968 states the transition from the wet period to the dry period, whereas the second – 1989 – indicates the shift from the dry period to the recovery period both in discharge and rainfall time series.
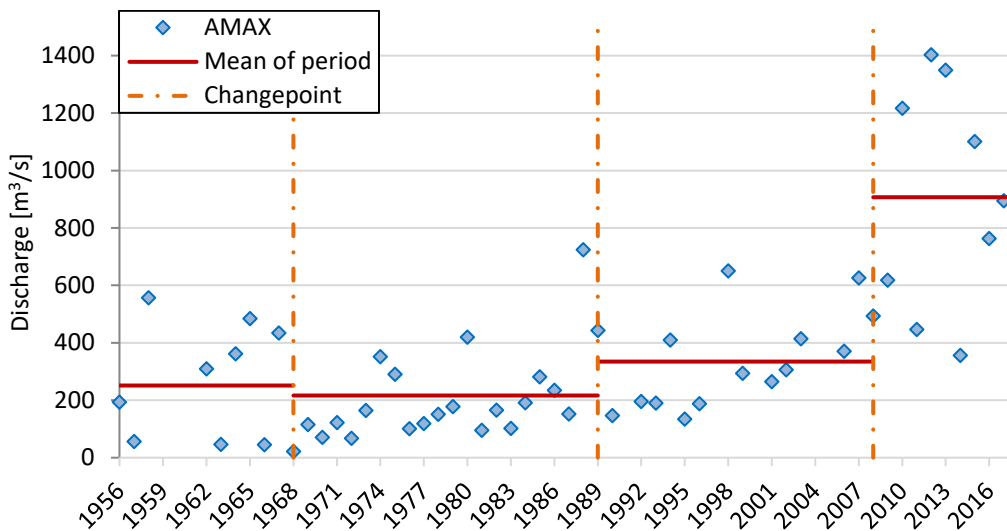


Figure 2.17 ANADIA AMAX time series (blue dots) in which changepoints (dash-dot orange lines) are demarcated. Red solid lines indicate the mean AMAX for each time-range.

Most notably, the new changepoint detected in 2008 represents the beginning of a new epoch characterized by frequent extreme floods. This point implies a new change in the discharge pattern, which find a direct correlation with the increase of extreme daily rainfall occurrence [14]. The study conducted by Panthou [18] examined the rainfall regime over the central Sahel and discovered a significant rise in heavy and extreme rain events frequency over the last three decades, essentially due to changes in the climate pattern after the great drought. As previously mentioned, this increment in discharge amount is also supported by the increasing runoff coefficient in Sirba basin (see Figure 1.3). This evolution is tightly related to the transformation of the land use, cover, and degradation affecting the whole watershed [32].

## 2.4.2 Annual flow-frequency characteristics of the Sirba river

The AMAX time series showed a great variability of discharge during the past half-century. To better understand how the streamflow of the Sirba river evolved among years, the updated time series was exploited for evaluating the water resource variability through the calculation of its flow duration curves (FDC).

Leboutillier and Waylen describe a FDC as "*the annual flow-frequency characteristics of rivers by depicting the cumulative frequencies for average ranked flows in a river*" [120].

The shape of the FDC provides important information regarding the basin and its hydrological regime. Since the estimation of the FDC is sharply sensitive to the interval of records used to calculate them, different periods of the time series were selected for the calculation of the Sirba's FDC (Table 2.5). This distinction was performed with a twofold aim:

(a) assess the evolution of the hydrological regime over time: the set of FDC are calculated for four time-ranges starting from the beginning and then from each changepoint until the last record;

(b) assess the river behaviour during each epoch: the set of FDC are calculated for each of the four time-ranges whose limits are defined by the detected changepoints.

Table 2.5 Periods identifying the set of records used to calculate each FDC.

| Evolution of the hydrological regime | River behaviour |
|:---:|:---:|
| 1956-2018 | 1956-1968 |
| 1969-2018 | 1969-1989 |
| 1990-2018 | 1990-2008 |
| 2009-2018 | 2009-2018 |

The two sets of FDC are displayed in Figure 2.18.
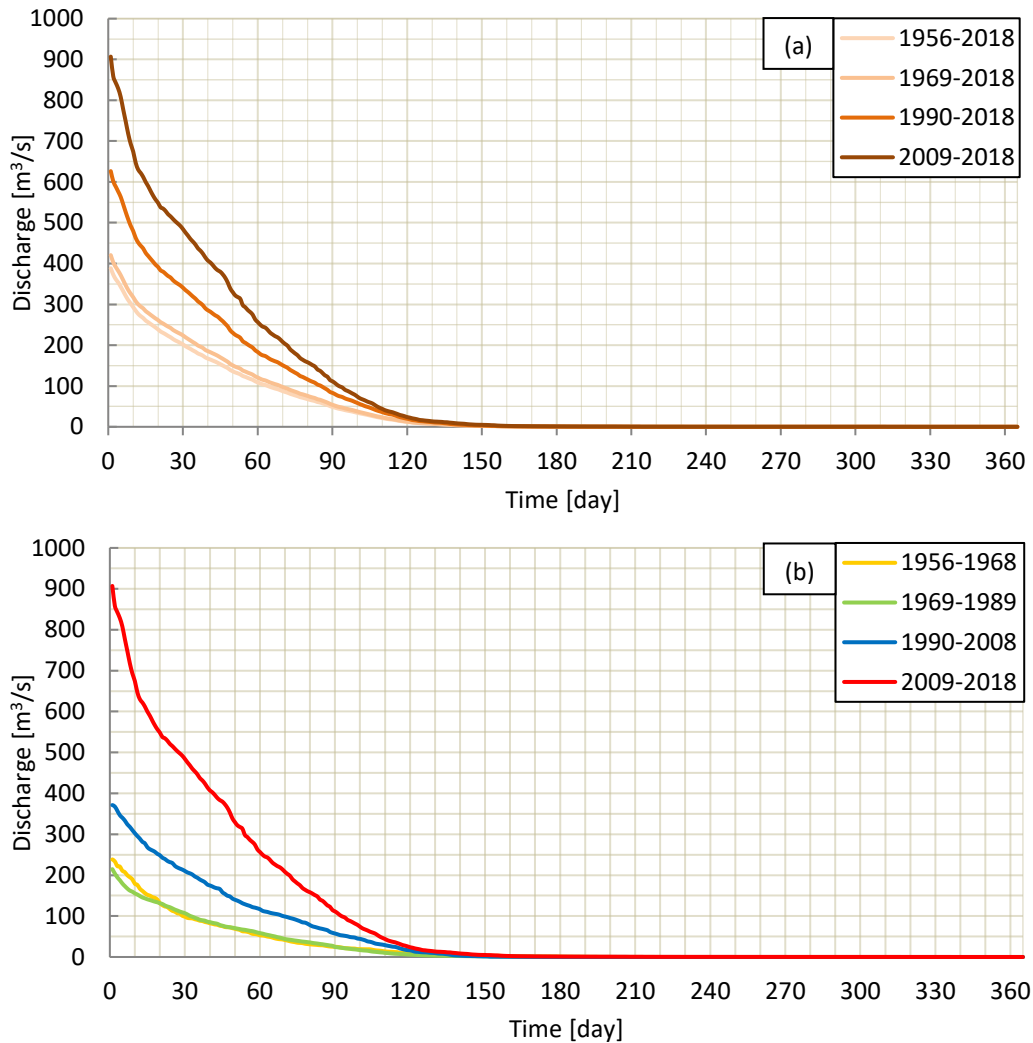
Figure 2.18 FDC used for the evolution of the hydrological regime are visualized in the graph (a), while the FDC used for the assessment of the river behaviour are displayed in the graph (b).

The evolutive trend depicted in Figure 2.18 (a) shows an incessant increase in magnitude and frequency of high discharge over the past decades, also bolstering the observations conveyed in recent studies of Descroix et al. and Aich et al. [32,39].

From the curves, some distinctive points, named characteristic discharges ($Q_d$), can be extracted for pointing out important peculiarities. The value $Q_d$ can be defined as the discharge that is averagely exceeded for a number of days ($d$) during the year; according to the entire period of record on which FDC is based. Physically, $Q_d$ refers to the amount of water that should flow on average into the river at least $d$ days per year. The characteristic discharge values for the two sets of FDC are listed in Table 2.6.

Observing Figure 2.18, the amount of $Q_d$ significantly varies over the different periods due to the relevant changes in the discharge pattern. Focusing on Figure 2.18 (b), the misalignment between the wet period (until 1968) and the dry epoch (the following twenty years called the great drought) can be observed mainly for discharge values higher than $Q_{20}$, thus with $d < 20$. The flatten shape of the lowest curve is totally in line with the rainfall pattern that characterized the dry period. The closeness of the first two curves in both graphs conveys that there was not a significant variation in the total amount of water flowed in the Sirba basin until 1989, but the differences are due to the lack of intense rainfall events over the entire dry period. After that, and according to the significant increase in runoff coefficients during the great drought, the recovery of rainfall led to a higher amount of water flowing into the river.

Comparing the annual maximum discharge ($Q_1$) over the last three decades, an average increase of 240% can be appreciated, from less than 400 m³/s (Figure 2.18 (b), blue line) to over 900 m³/s (Figure 2.18 (b), red line). This trend reflects the ongoing rise of the extreme flood frequency which are affecting thousands of people in the whole Middle Niger [98].

Table 2.6 FDC characteristic discharges for both sets of curves.

| $Q_d$ | Evolution of the hydrological regime [1] | | | | River behaviour [2] | | | |
|---|---|---|---|---|---|---|---|---|
| | 1956-2018 | 1969-2018 | 1990-2018 | 2009-2018 | 1956-1968 | 1969-1989 | 1990-2008 | 2009-2018 |
| $Q_1$ | 390.7 | 422.0 | 627.6 | 906.9 | 238.5 | 214.7 | 371.4 | 906.9 |
| $Q_5$ | 344.7 | 372.3 | 564.0 | 807.9 | 210.9 | 179.7 | 340.4 | 807.9 |
| $Q_{10}$ | 294.2 | 318.1 | 480.4 | 674.4 | 179.0 | 155.6 | 302.5 | 674.4 |
| $Q_{30}$ | 201.7 | 223.8 | 341.0 | 484.2 | 98.6 | 106.9 | 210.3 | 484.2 |
| $Q_{60}$ | 108.5 | 120.5 | 183.4 | 256.7 | 53.0 | 58.3 | 116.7 | 256.7 |
| $Q_{91}$ | 47.0 | 51.9 | 80.1 | 107.2 | 24.5 | 23.7 | 55.6 | 107.2 |
| $Q_{135}$ | 5.7 | 5.9 | 8.8 | 11.2 | 4.9 | 2.9 | 6.6 | 11.2 |
| $Q_{182}$ | 0.4 | 0.4 | 0.5 | 1.0 | 0.6 | 0.2 | 0.1 | 1.0 |
| $Q_{274}$ | 0.0 | 0.0 | 0.1 | 0.1 | 0.0 | 0.0 | 0.0 | 0.1 |
| $Q_{355}$ | 0.0 | 0.0 | 0.0 | 0.0 | 0.0 | 0.0 | 0.0 | 0.0 |

[1] relative to Figure 2.18 (a)

[2] relative to Figure 2.18 (b)

Besides the higher values of $Q_d$, another marginal consideration that can be underlined for the lower discharge. The positive trend seems to convey that the

river, despite it is still intermittent, is wet for more days a year. Thus, the pattern is characterized by longer permanency of discharge into the riverbed. Riverine inhabitants could take benefit in term of a longer availability of freshwater over the year.

### 2.4.3 Trend analysis

As showed in the previous two sections, the time series of discharge is characterized by great variability. To estimate the tendency towards the increasing occurrence of catastrophic floods, the monotonic linear trend detection and estimation were performed using MAKESENS [121]. This tool is based on the use of two non-parametric methods: the Mann-Kendall (MK) test and the Sen's approach. MK test detects the presence of a monotonic increasing or decreasing trend, rejecting the null hypothesis ($H_0$) with a certain level of significance $\alpha$. The Sen method computes the slope of the existing linear trend evaluating its magnitude. A well-defined monotonic linear trend (statistical significance $\alpha = 0.001$) was detected for both time series of discharge, DGRE and ANADIA (Figure 2.19). Through the Sen's approach, a slope of 4.44 was estimated, whereas the revised series show a slope two times steeper (8.75). This jump furtherly confirms the dangerous pattern that has been emerging in recent years. The marked positive trend over the entire period states that the increase in flood magnitude is not in line with the rainfall trend, given that a decrease in total precipitation over the last seventy years has been observed [72]. This opposite pattern is consistent with the anomalous behaviour of Sahelian rivers referred to as Sahelian Paradox.
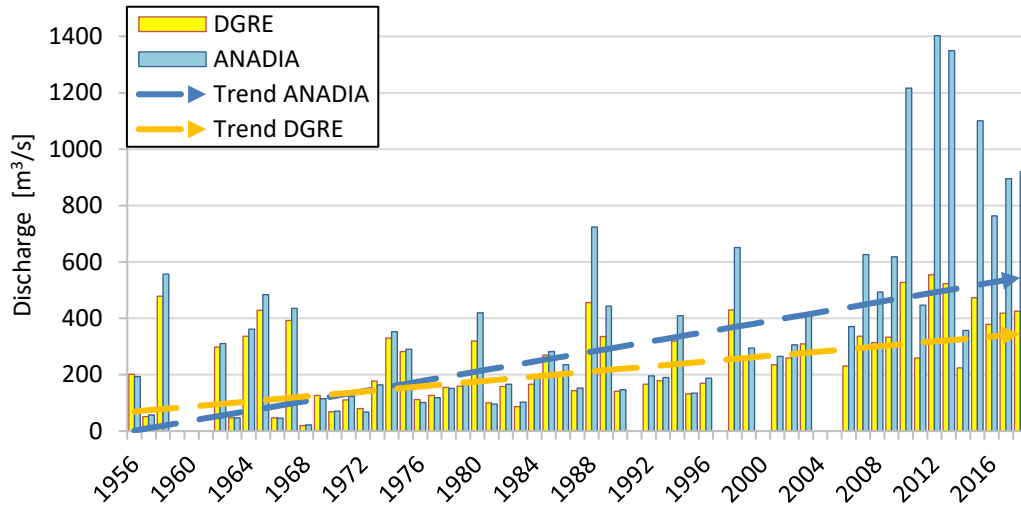
Figure 2.19 Monotonic linear trends overlapped to the related AMAX time series.

In order to provide a clear visualization of the AMAX variability over each time-range, the ANADIA AMAX anomaly and its tendency were evaluated. The AMAX anomaly was examined through the calculation of the Standardized Anomaly Index (SAI) introduced by E.B. Kraus [122,123], evaluated as

$$SAI_i = \frac{AMAX_i - \mu_{AMAX}}{\sigma_{AMAX}} \qquad (2.3)$$

where $SAI_i$ is the standardized anomaly index of AMAX for year $i$, $AMAX_i$ is the annual maximum discharge for year $i$, $\mu_{AMAX}$ and $\sigma_{AMAX}$ are the mean and standard deviation, respectively, of the AMAX time series. This metrics is frequently used to study the evolution of climate changes and their impacts [124,125]. Moreover, the local regression-fitting technique LOESS (LOcally Estimated Scatterplot Smoothing) was used to identify and visualize the tendencies in data distribution [126]. It is a widely used non-parametric regression method that combines multiple regression models in a k-nearest-neighbour-based meta-model. With this technique, a smooth curve, a so-called Loess Curve, is generated all through the set of data. Additionally, 10 years moving average line was plotted to better remark the time series pattern.

Considering the distribution of anomalies, a curious difference with previous studies can be noticed. Indeed, the SAI values of the wet period (until 1968) are even negative since the mean discharge is strongly increased taking in account the annual maximum discharge of the last years, which are the highest records over

the entire time series. This outcome is contrary to that of Aich et al. [39] who used the previous and outdated time series.

Figure 2.20 shows a smooth loess curve with a fluctuation between -67 and -17 until the end of the past century and with a critical point (minimum) in 1975. Then a steep positive trend begins until the end of the recorded period. The high frequency of extreme floods during the past decade delineates a new flood pattern. This tendency is also confirmed by superimposing the moving average line above the loess curve. Both curves accurately follow the same path.
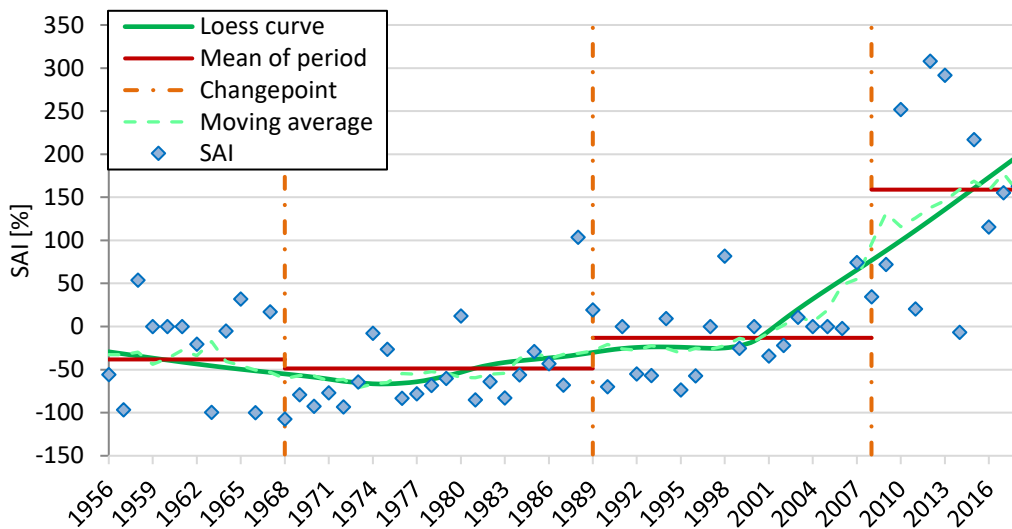


Figure 2.20 Temporal distribution of Standardized Anomaly Index of the annual maximum discharge (blue dots). Each period is enclosed between the detected changepoints (dash-dot orange lines). Trends depicted using a loess curve (green solid line) and moving average line (dash green line). The mean of each period (red lines) was also added to highlight the significant increase that characterizes the last epoch.

## 2.5   Flood Hazard Assessment

The outcomes presented in the previous sections represented the first step and the basis for the assessment of the flood hazard level to which the riverine inhabitants of the Sirba river are exposed. The flood hazard evaluation and visualization pass through the definition of the hazard scenarios to the identification and delineation of flood-prone areas.

## 2.5.1  Flood hazard scenarios

In order to make the classification of the flood hazard level concordant with the final users' knowledge, the adopted approach follows the official flood hazard scenarios already used in the Niger Republic. The hazard thresholds were identified by a multidisciplinary team involving national departments (i.e. Ministry of Hydraulic, Directorate of Meteorology and Ministry of Agriculture) and regional authorities (Niger Basin Authority and Agrhymet Regional Center) [127]. The flood hazard scenarios definition was accomplished following an impact and statistical-based approach. Firstly, "impact-based" because the field effects induced by floods were considered and they drove the design of each scenario. Secondly, in order to make univocal the description of the scenarios' thresholds, statistical metrics were identified for fixing certain flow conditions to the related hazard thresholds.

### *Flood-related field impacts – hazard classification*

As well highlighted in Figure 2.21, the increasing number of people affected by flooding events have pushed local authorities in setting a system able to store all important information related to flooding events and their impacts.
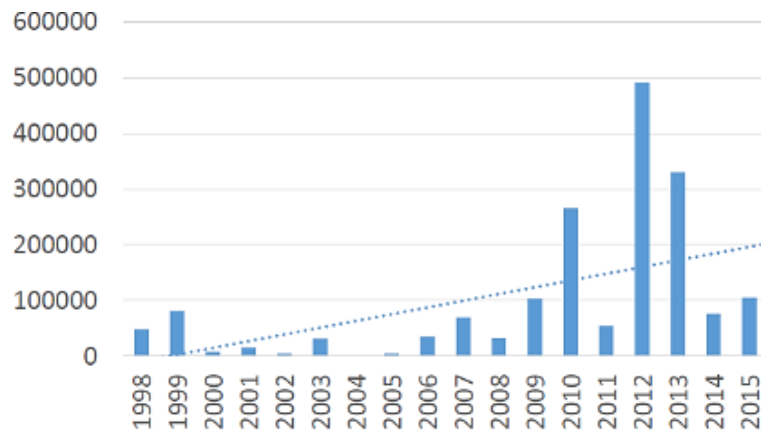


Figure 2.21 Number of people affected by floods in the whole Niger in the period 1998-2015 (source: [98])

For this purpose, in 1998 a national database was created and named ANADIA Niger Flood Database (ANFD). It represents the first effort in digitalizing such information in a unique platform available for different stakeholders but the lack of a standardized procedure for data collection during on-site surveys produced a non-detailed and incomplete dataset [98]. Despite these weaknesses, some important information can be extracted. Merging the data

collected into the ANFD with the AMAX time series allows tracking the most damaging floods and related impacts on the Sirba riparian villages. The villages and their inhabitants affected by the most significant floods are reported in Table 2.7.

Despite some important data were not detected, i.e. records for the 1998 and especially 2012 events, the data reveal that the flood-related impacts are not always directly proportional to the magnitude of the flood. Looking at the last 5 year of the analysed period, it is clear how the spirit of adaptation and flood awareness led to decreasing negative impacts even with the same flood severity. Meaning that people are inclined to move away once the hazard has been perceived. Indeed, the flood 2010 (with a magnitude never experienced before) affected more than 20'000 people, whereas only three years later a more violent flooding affected less than half of the people and even less in 2015. Even whether it is not recorded, the flood in 2012 was the highest and brought great devastation, especially to the agricultural sector.

Table 2.7 Villages and people affected by each flooding events during the period 1998-2015. NA indicates Not Available data. Nb: the number of people affected coincides with the total number of people living in the villages damaged by the flood. The floods that induced evident damages are those that overcoming a discharge of 600 $m^3$/s.

| Year | Maximum flow [$m^3$/s] | N° of villages involved | People affected |
|------|------------------------|-------------------------|-----------------|
| 1998 | 651 | NA | NA |
| 2007 | 626 | 4 | 11'017 |
| 2009 | 618 | NA | NA |
| 2010 | 1'216 | 18 | 21'325 |
| 2012 | 1'403 | NA | NA |
| 2013 | 1'349 | 3 | 10'383 |
| 2015 | 1'101 | 1 | 3'687 |

The considerations advanced above confirms that the risk evaluation is a complex task since not only physical factors (e.g. hydrological or climatic regime) are important but also social factors (population growth, urban development, and risk awareness) play a crucial role [128–130].

Once considered the damages caused by the historical floods, the Nigerien classification provides a detailed list of consequences bonded to each configurable flood scenarios:

**Green**: in the river flows an ordinary amount of discharge which does not negatively affect any riverine activities and does not represent a hazard for the livestock;

**Yellow**: frequent flood that slightly affects human activities. It could likely damage fishing nets, assets, water pumps and cause livestock losses along the river;

**Orange**: severe flood that has significant impacts on human life. It can hurt the houses closer to the river and block the accesses to the wells closest to the river banks;

**Red**: catastrophic flood that highly threats human life. The water may reach a vast portion of the riverine villages causing massive damages with likely human losses.

Thus, this classification guided our analysis in the definition of the flood hazard scenarios and their thresholds.

### *Statistical investigation – hazard thresholds*

In river engineering, increasing attention has focused on the description of metrics and design indexes related to the definition of floods [131]. The flow time series of the Sirba river shows a marked trend and therefore a strong non-stationarity of the dataset. It makes the use of standard statistical analyses not appropriate, i.e. statistical models based on the assumption of stationarity over the whole dataset. Thus, for achieving an accurate flood hazard evaluation, it is suggested the use of models able to take into account the evolutive behaviour of datasets, meaning, in this case, the river discharge [111]. According to these considerations, several metrics were exploited to define the level of flood hazard.

Three statistical tools are used to attribute a specific design discharge to each one of the four flood hazard categories delineated in the previous section. Firstly, to the ordinary flow condition and low magnitude floods were quantified using the characteristic values of the FDC, which identify the river actual behaviour (i.e. the last homogeneous period (2009-2018), see Table 2.6). Then, a Non-Stationary Generalized Extreme Value (NSGEV) model was fitted to the AMAX updated time series (1956-2018) using the same methodology described in the work of Wilcox et al. [111], in order to look at the consequences on extreme flow features. The analysis was carried out by Catherine Wilcox itself during a collaboration with the Institut des Géosciences de l'Environnement, Université Grenoble Alpes. Finally, a Stationary GEV (SGEV) fit to the updated data was computed for

**45**

providing statistical indexes, quickly calculable with an easier method, and to highlight risks of ignoring the non-stationarity of the dataset.

The GEV distribution is a statistical function designed to represent the distribution of variables and widely used for variables representing maxima values. In this case, the dataset of variables is represented by the time series of the annual maximum discharge, so-called AMAX. The GEV function can be written as

$$GEV\ (AMAX; \mu, \sigma, \xi) = \ exp\left\{-\left[1 + \xi\left(\frac{AMAX - \mu}{\sigma}\right)\right]^{-\frac{1}{\xi}}\right\}$$

$$for\ \ 1 + \xi\left(\frac{AMAX - \mu}{\sigma}\right) > 0$$

(2.4)

where the three parameters of the function are: $\mu$ is the location parameter, $\sigma$ is the scale parameter and $\xi$ is the shape parameter. These three parameters can be evaluated according to given criteria to account or not for the non-stationarity of the dataset. For the SGEV, the parameters are constant, thus GEV($\mu, \sigma, \xi$). Instead, in the NSGEV method, the parameters are time-dependent and vary over time, GEV($\mu(t), \sigma(t), \xi(t)$), meaning that parameters are different for each year.

For simplicity, the flood return times calculated with the two methodologies will be called S-RT$_{xx}$ (Stationary Return Time) for the SGEV, whereas NS-RT$_{xx}$ (Non-Stationary Return Time) for NSGEV; the xx values represent the number of years.

The hazard scenarios and their thresholds so defined are summarized in Table 2.8. The thresholds represent the maximum discharge related to each scenario and therefore must be considered as the upper limit of each step of the hazard scale. Each discharge value is unequivocally identified by a statistical index that defines its frequency of occurrence.

The four flood hazard scenarios are therefore characterised by the magnitude of the flooding event and associated impacts on human life and assets:

- **Green:** it corresponds to each discharge values below the threshold of 600 m$^3$/s which corresponds to the FDC characteristic value of Q$_{15}$ or a S-RT of 5 years (S-RT$_5$).
- **Yellow:** it ranges between 600 and 800 m$^3$/s, where the upper limit is set at the flow correspondents to Q$_5$ and, equivalently, to S-RT$_{10}$ and NS-RT$_2$.

- **Orange:** it spans from 800 to 1'500 m$^3$/s, where the upper threshold corresponds to a flood with a S-RT$_{30}$, equivalent to a NS-RT$_5$.
- **Red:** quantified up to 2'400 m$^3$/s that is related to the flood event with S-RT$_{100}$, equivalent to a NS-RT$_{10}$.

Table 2.8 Flood hazard scenarios and thresholds of the Sirba River.

| | $Q_{max}$ [m$^3$/s] | $Q_d$ | Index S-RT$_{xx}$ | NS-RT$_{xx}$ | Magnitude |
|---|---|---|---|---|---|
| Green | 600 | 15 | 5 | - | Ordinary flow |
| Yellow | 800 | 5 | 10 | 2 | Frequent flood |
| Orange | 1'500 | - | 30 | 5 | Severe flood |
| Red | 2'400 | - | 100 | 10 | Catastrophic flood |

### *Further considerations concerning extreme values distribution*

Besides the quantification of the return times of the hazard thresholds, the GEV distribution was exploited for further analyses.

First, the results of the previous work of Wilcox et al. 2018 [111], which performed a non-stationary analysis on the old AMAX time series for the Garbey Kourou station (DGRE time series), were compared with the NSGEV fitted to the updated series. The comparison aims to investigate the influence of rating curve accuracy on the estimation of the extremes trend. The former results showed that the double linear was the optimal model to represent the temporal variation of NSGEV parameters. This temporal function concerns the variation of both $\mu(t)$ and $\sigma(t)$ parameters over time. The variation follows a linear trend with different slopes up to and after a breakpoint. The double linear model was also confirmed for the updated dataset with a high level of significance (α<0.001). Instead, the shape parameter has been considered constant in both studies. The NSGEV's parameters time-variation is shown in Figure 2.22. The same breakpoint in 1996 for $\mu$ was found for both time series. Conversely, for $\sigma$, the old time series shows a breakpoint in 2003, whereas in 2006 for the updated series. The reason for this mismatch can be likely triggered by a boundary effect. Indeed, the methodology limits the search of a breakpoint up to 10 years from the edges of the data series, so the breakpoint 2006 would not have been identified since the former study analysed the time series until 2015. Looking at Figure 2.22, both parameters show

a marked rising trend after the breakpoint, with a greater slope for the updated series. This conveys an ongoing increase in the magnitude and variability of extreme floods. The $\xi$ parameter is higher in the updated series but with a much larger confidence interval than the old series. This result suggests that the most extreme floods can be even worse than previously assessed, but without a solid certainty since the higher level of uncertainty.
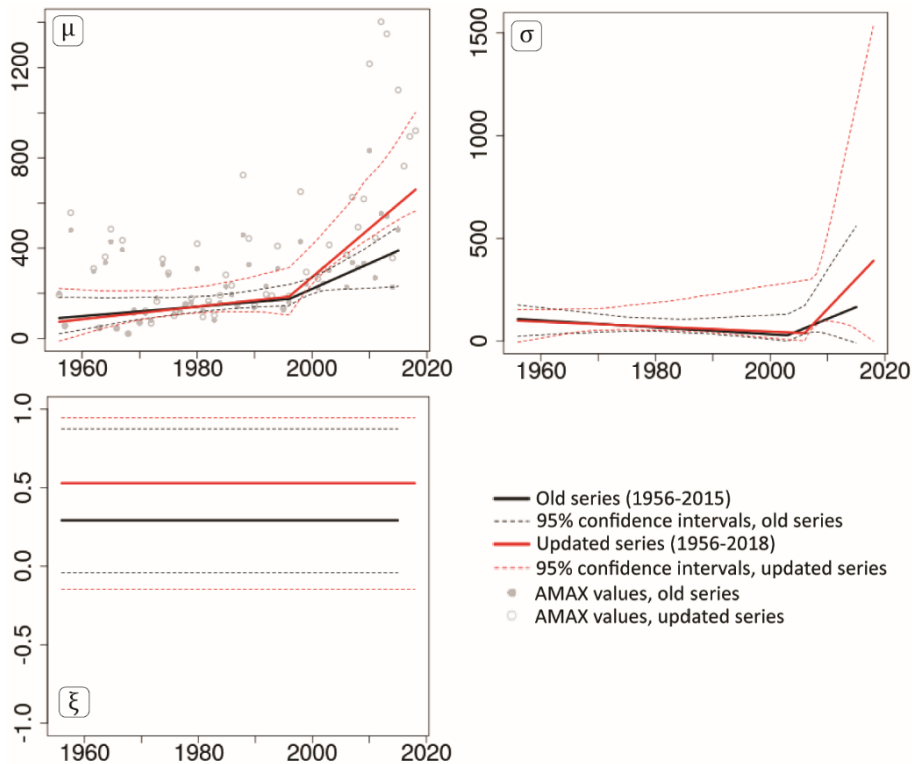


Figure 2.22 NSGEV's parameters time-variation for both the old and the updated AMAX time series.

A second consideration, the return times calculated with the NSGEV were compared to the ones from the SGEV, in order to appreciate what it means to ignore the non-stationarity of the dataset. The results from the two methodologies are displayed in Figure 2.23, showing how discharge related to the return time evolves according to the dataset tendency. Observing the graph for the shortest return time of 2 years, the discharge calculated with the NSGEV show a sharp raising trend with an increase of several hundred $m^3$/s in the last two decades. The main issue related to the non-stationary method is that the intervals of confidence exponentially increase as the return times increase, making low the reliability of the result. Up to $RT_{10}$, the confidence levels between the two methodologies were comparable. Instead, results were less clear once overcame 10-year return time.

The level of uncertainty for the NS-RT$_{20}$ diverges towards unrealistic values. This illustrates, despite the great potential of such methodologies, the huge challenge of estimating the value of a given return time in a non-stationary context.
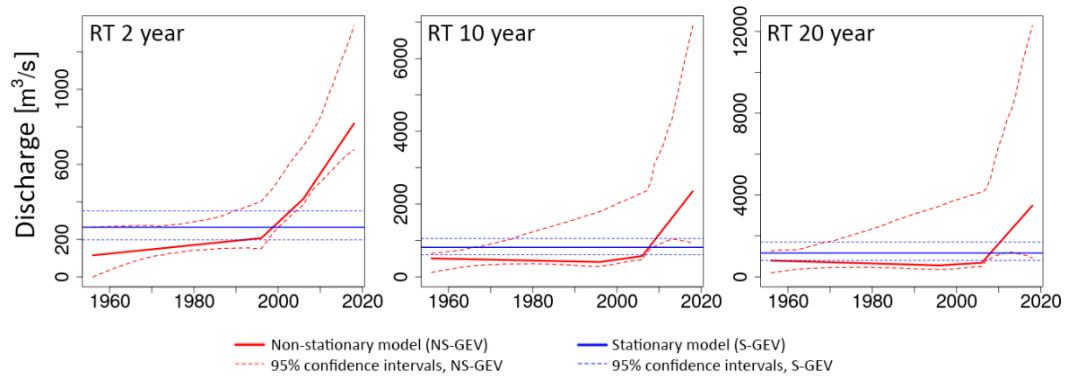


Figure 2.23 Discharge evaluated with the stationary and non-stationary models for a return time of 2,10 and 20 years from left to right, respectively.

In the context of hydrological extreme events, the comparison between return times calculated considering the stationary or non-stationary of the dataset it is used to evaluate the influence of the presence of a trend into the time series. In this case, the comparison underlines that NS-RT are almost ten times lower than the S-RT (Figure 2.24) [111,132]. For example, the discharge related to a S-RT$_{200}$ is equivalent to a NS-RT of almost 20 years, meaning a likelihood of occurrence ten times higher. This behaviour is justified since AMAX increases in accordance with time, especially in the last two decades. Moreover, as shown in Figure 2.20, the trend raises very sharply.

Comparing the relation between RT calculated with the updated and previous AMAX time series, it is noticeable how the discrepancy between S-RT and NS-RT is even higher using the old series (e.g. the discharge for S-RT$_{300}$ is equal in case of NS-RT$_{15}$).
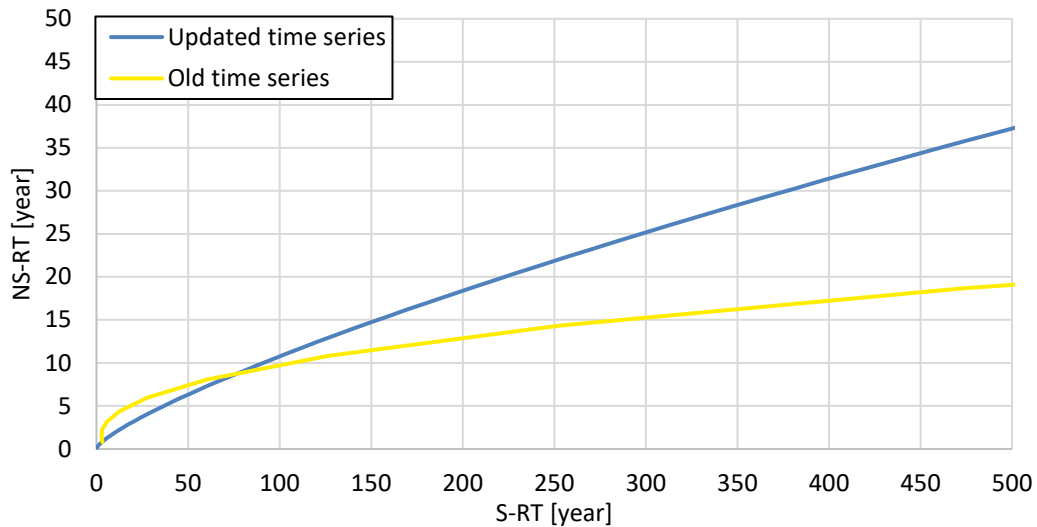
Figure 2.24 Variation of NS-RT as a function of S-RT. The blue line represents the relation between the RT obtained using the updated AMAX time series, while the yellow line concerns the relation between the RT calculated using the old AMAX time series.

## 2.5.2 Flood hazard mapping

Flood hazard mapping of the Sirba River represents a crucial step towards the implementation of the EWS SLAPIS. Furthermore, it provides the first assessment of the hazard to which riverine populations are directly exposed. Thus, this result would contribute to the flood-hazard assessment of African countries, encompassing also a comprehensive analysis of the hydraulic aspects and local dynamics [133–136]. The delineation of the flood-prone areas has been achieved through the simulation of the hazard scenarios explained in the previous section. The hydraulic simulations have been computed using a hydraulic numerical model specifically implemented to realistically represent the hydrodynamic behaviour of the Sirba river.

### *Hydraulic model*

The hydraulic numerical model was implemented using the software HEC-RAS (Hydrologic Engineering Center–River Analysis System) developed by the US Army Corps of Engineers, in its version 5.0.6 [137,138]. HEC-RAS is a physically-based numerical model able to compute the flow field solving the De Saint Venant equations [139–141]. Considering the large extension of the study area, more than 100 Km of river reach, the mono-dimensional configuration was chosen to decrease the computational load of the analysis. The digital

representation of the riverbed was shaped on 147 cross-sections extrapolated from precise DTMs (Digital Terrain Model) and topographical surveys realized in February and September 2018 (Figure 2.25). Moreover, the cross sections extend beyond the river banks in order to simulate the runoff over the floodplains.



Figure 2.25 Extracts from land surveys during topographical operations (Photo credit: Giovanni Massazza and Paolo Tamagnone).

The data collected during on-site surveys were also fundamental for the calibration process. The main factor that drives the calibration of a hydraulic numerical model is the definition of the roughness parameters, which aim to replicate the real flow friction. As common practices in river engineering, the roughness was defined through the Manning's formulation and different coefficients were attributed to each zone of the domain, making distinctions between the watercourse and riverine areas. Firstly, the river channel roughness was calculated in conformity with the procedure developed by Cowan (1956) and detailly explained by Ven Te Chow in his the book Open-Channel Hydraulics [139]

$$n = (n_0 + n_1 + n_2 + n_3 + n_4)\, m_5 \qquad (2.5)$$

where $n_0$ is the base value related to the natural materials on which the water flows, $n_1$ is an additive value accounting for surface irregularities, $n_2$ is the value added for taking into account the geometrical variations of the channel cross sections along the reach, $n_3$ considers the obstructions, $n_4$ represents the increment of friction due to the presence of vegetation, and $m_5$ corrects the global roughness in accordance with the sinuosity of the river.

Taking advantage from the intermittency of the Sirba river during the dry season, it was possible accomplishing the evaluation of the riverbed roughness $n_0$ from the characterization of its sediment. Due to the impossibility of carrying out the grain size classification directly on-site, the granulometry of several sampling points was evaluated using a digital quadrillage approach with BASEGRAIN v.2.2.0.4 [142,143]. This MATLAB plug-in embeds an object detection algorithm (ODA) which is able to identify, after a previous calibration, every single grain from photographs of the gravel bed, and subsequently evaluate the size and distribution of the sediment within the analysed spot (see Figure 2.26).
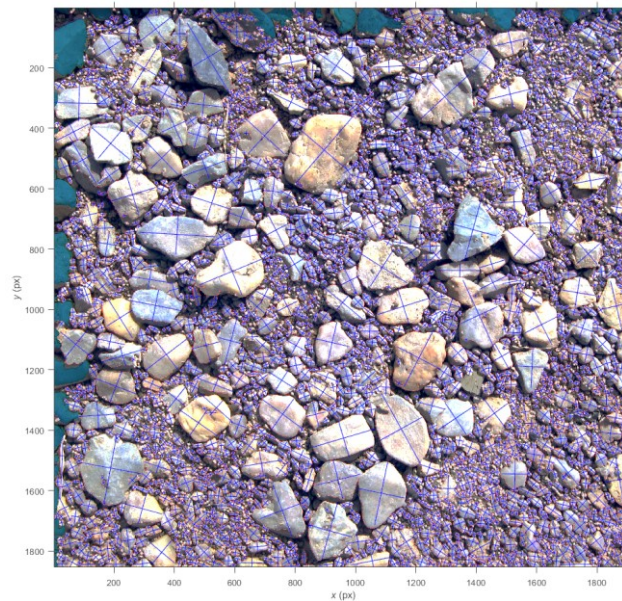


Figure 2.26 Grain size and distribution detection through ODA.

Notwithstanding this approach is not able to characterize the finest part of the sediment, it is a fast and effective method to define the coarse fraction of river's sediments, meaning the part that effectively offers resistance to the flow.

The Sirba riverbed is characterized by a rather course material with a mean particle size within the range 20-36 mm (Figure 2.27). Even though there are also alternations of areas covered by sandy deposits; these fine sediments are not detectable by the adopted methodology.
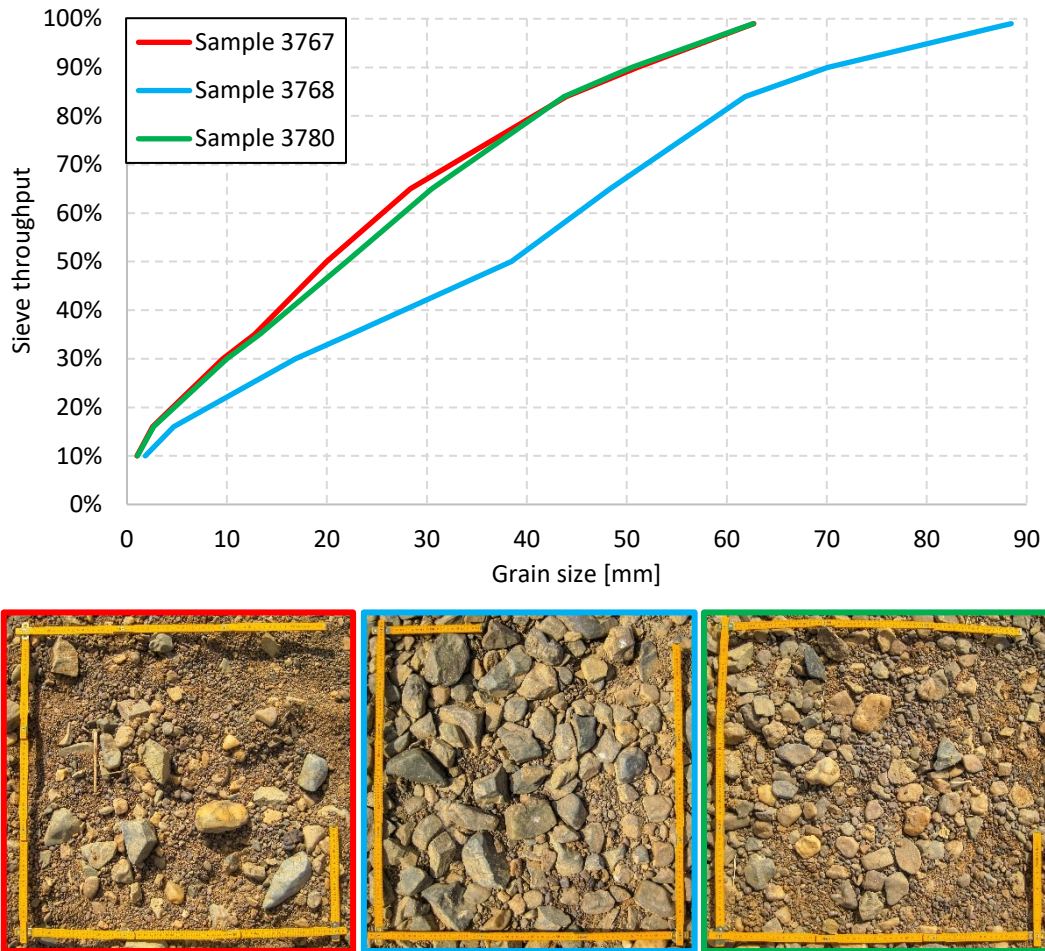
Figure 2.27 Grain size distribution and pictures of three representative spots picked up along the Sirba river. Nb: in each pic is present a meter used for the calibration of the ODA.

Sieve throughput characteristic values were used to calculate the related roughness, i.e. the relative Manning coefficient, through the Irmay's equation (1949) [144], written as:

$$n_0 = \frac{1}{24} D_{65}^{\frac{1}{6}} \qquad (2.6)$$

where $D_{65}$ is the particle diameter correspondents to the sieve throughput of 65%. Focusing on the samples shown in Figure 2.27, the Manning coefficients were 0.023 for samples 3767 and 3780 (similar grain distribution), and 0.025 for the sample 3768 (coarser grains).

The base value of roughness $n_0$ was then corrected with the additive values quantified according to the values proposed by Chow [139] as $n_{1,4} = 0.005$, $n_{2,3} = 0$ and $m_5 = 1$.

**53**

Finally, the definitive Manning coefficients were refined during the calibration process. In this phase, it was verified that the model was capable of correctly simulating the same relation stage/discharge as measured during the surveys made in September 2018 in different cross sections along the river reach. The final Manning coefficients are listed in Table 3 of the work of Massazza et al. [38].

### *Further uses of the hydraulic model*

Once tested that the hydraulic model was aligned with the real hydrodynamic behaviour of the river, it was exploited to accomplish a second analysis: the comparison between the RC computed by the hydraulic model and the ANADIA RC, for the cross section of Garbey Kourou and Bossey Bangou.

Figure 2.28 shows a good alignment throughout both comparisons. This match furtherly confirms the reliability of the hydraulic model in simulating the hydrodynamics of the river, even when the water level significantly rises. Moreover, it allows extending the RC ranges of validity beyond the aforementioned limits, set in correspondence of the maximum field measurement. Indeed, the validity of the GK RC may be extended up to 500 cm (see also Table 2.2), whereas a noticeable extension up to 800 cm can be deemed valid for the BB RC (see also Table 2.3). However, these are extrapolations that should be confirmed carrying out discharge measurements also for higher water levels, without neglecting the security of the operators.
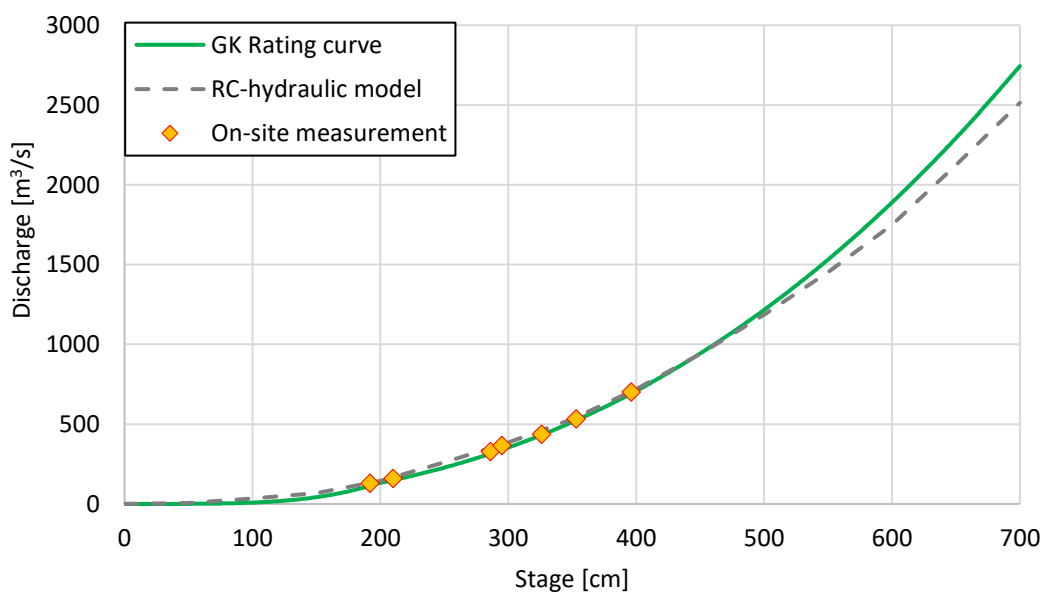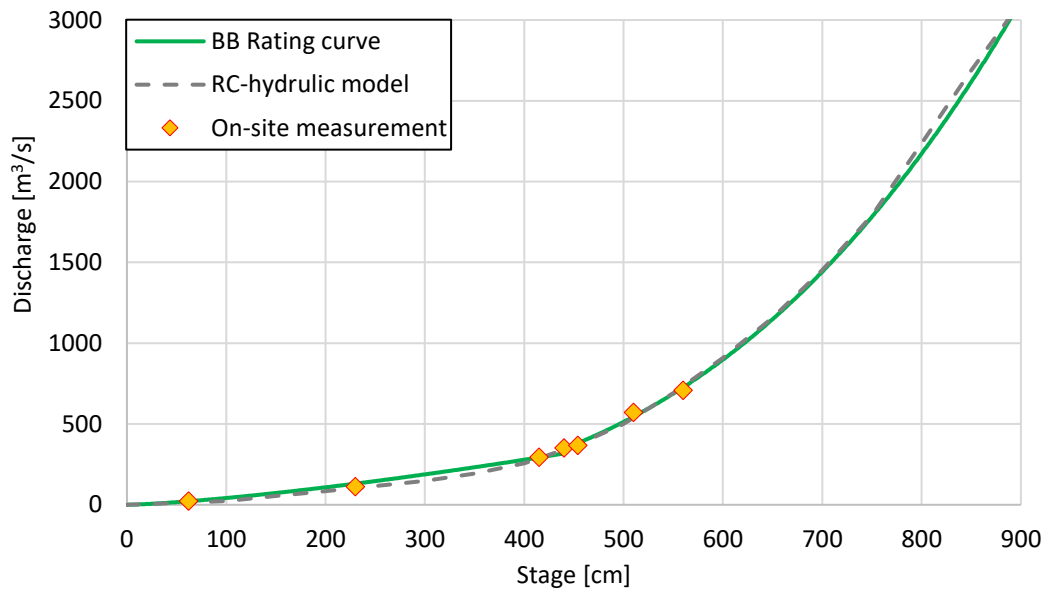
Figure 2.28 Comparison between rating curves previously calculated and from the hydraulic model for the two gauging stations of the Sirba river, Garbey Kourou (upper graph) and Bossey Bangou (lower graph). The on-site measurements refer to the measure campaigns made during the wet season 2018.

### *Flood hazard maps*

The simulation of the flood scenario using the hydraulic model allowed to identify the flood-prone areas and delineate the perimeter for each level of hazard.

These maps will be used to early activate specific security protocols related to each level of alert. The extension of each flood hazard scenarios is freely downloadable at the link: http://sdicatalog.fi.ibimet.cnr.it:5003/fr/dataset/risk-scenarios2.

An extract of the outcomes is illustrated in Figure 2.29. The image shows the 11 villages set along the Nigerien reach of the Sirba river and whose territories are characterized by a source of hazard deriving from the inundations of the river. Most of these settlements are located along the left bank of the Sirba River, thus the left strip is the most susceptible to be damaged by floods. Concentrating on the distribution of buildings set within the flood-prone areas, it is noticeable how most of the houses are into the red zone, whereas a few buildings in the orange zone. This confirms the aforementioned "adaptive behaviour" of the riverine inhabitants. Indeed, the last severe flood in 2012 destroyed almost every structure placed into the areas labelled with the orange hazard level and, subsequently, the inhabitants of those areas have rebuilt their houses a little further away from the river banks.
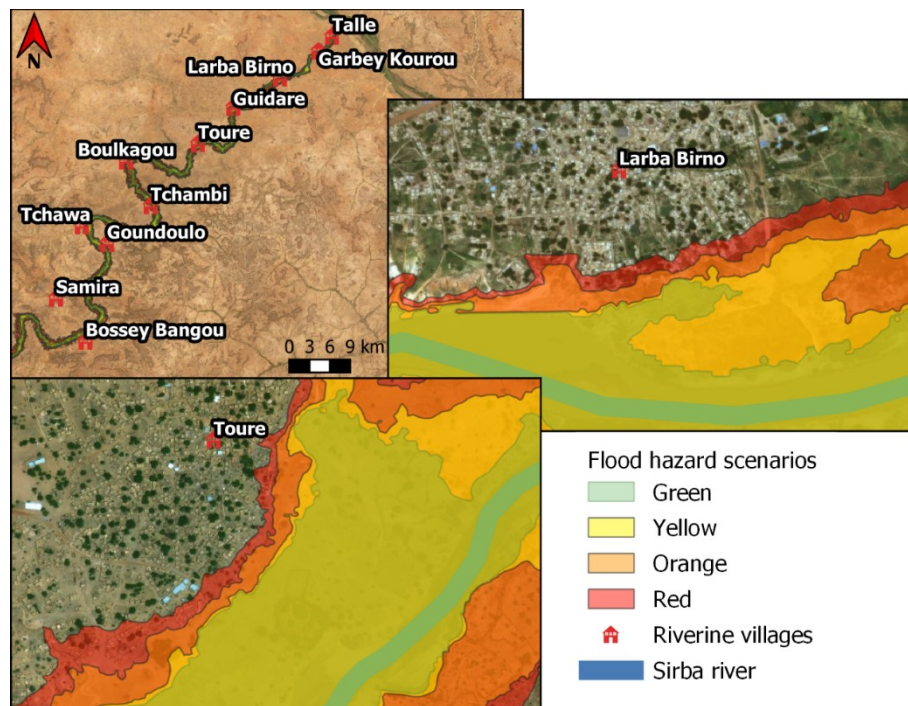
Figure 2.29 Riverine villages potentially affected by flooding events. Enlargements: flood hazard maps of the river sections next to the village of Toure and Larba Birno.

## 2.6  Sahelian Flood 2020

During all our analysis, the flood generated by the rainstorms occurred during the wet season 2012 was the highest ever registered. This record was overcome during the current rainy season 2020. This was the initiation of SLAPIS and allowed to effectively test the EWS capacity [145].

The flow time series recorded in the two crucial gauging stations of the Sirba river are reported in Figure 2.30 (downloadable at http://sdicatalog.fi.ibimet.cnr.it:5003/dataset).

The two hydrographs show three distinct peaks. The first at the end of July, which overcame the maximum alert in BB gauging site. The second in the middle of August, with peaks that almost have equalled the levels registered in 2012 at GK. Then, one month later, the peak with the highest magnitude occurred during the second decade of September. This latter peak almost reached the red threshold in GK, while abundantly crossed it at BB.
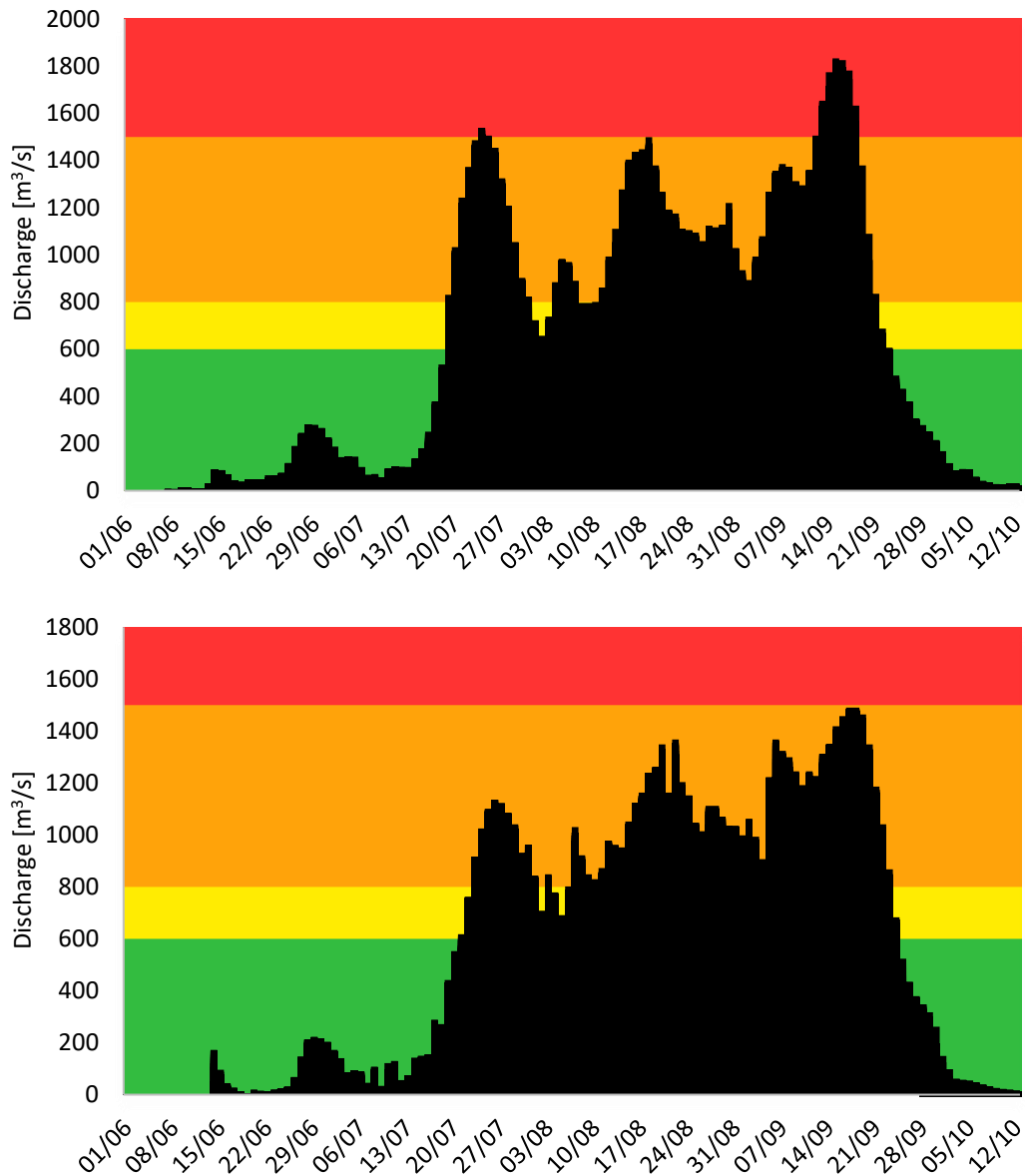
Figure 2.30 Discharge evolution over the wet season 2020 gauged at the Bossey Bangou (upper graph) and Garbey Kourou (lower graph) stations.

The consequences have been impressive. The flood heavily affected almost all riverine villages with losses of important assets, orchards, and vegetable garden, problems to gauges and electrical instrumentations but without any human loss (see Figure 2.31).

Figure 2.31 Images displaying some of the flood-related impacts (source: climateservices.it)

## 2.7 Concluding remarks

The staggering frequency with which hydrometeorological extremes are occurring in Sahelian countries has attracted the attention of many people, from directly interested governments to the scientific community. Despite different approaches to deal with the problem, everyone agrees with the impellent necessity to establish effective strategies helping to protect the economic sector and, principally, human lives.

In this chapter, we explained all the analyses and actions carried out as the preparatory phase aimed at the implementation of the first early warning system at the service of the riverine communities of the Sirba river. This phase embeds various hydrological, hydraulic, and statistical analyses.

The first achievement is represented by the re-calibration of the rating curves calculated for the gauging station of Garbey Kourou, also accompanied by the updating of its flow time series. These outcomes enhance the accuracy of the evaluation of streamflow and reliability of floods estimation. Pondering that the Sirba river is the main tributary of the Middle Niger River, the updated flow time series represents a crucial starting point for future works on hydrological and river

engineering in the central Sahel. Moreover, enhancing the reliability of data is the key point for making the hydrological/hydraulic modelling more robust and more accurate, especially when regional and sub-regional scale analyses are performed.

With the revision of the GK RC, also the rating curves characterizing the discharge evaluation into the hydraulic junction Sirba-Niger were observed and lacks highlighted. The water balance computed at Niamey also confirmed that the updated discharge of the Sirba river noticeably decreases the mismatch affecting the discharge assessment, improving the understanding in such fragile context.

Furthermore, the rating curve of the new gauging station installed in correspondence of the village of Bossey Bangou was calculated. This station, placed at the head of the analysed river reach, is fundamental for the functioning of the EWS since it is the place where the first alert is sent. Considering the strategic importance of these control systems, a greater effort should be put in keeping updated them.

Secondly, following the updates, the river regime and its tendency have been re-investigated. The evaluation through flow duration curves showed an ongoing increment in the amount of streamflow. This trend is mainly driven by the increasing surface runoff in the whole area and the slight recovery of annual rainfall. The greater amount of water is unfortunately also linked with a rising trend of the annual maximum peaks, which could likely increase in frequency and intensity in the coming years.

The sharp trend of the flow time series suggests that the evaluation of the frequency of these events cannot be addressed with a standard method, but it requires to consider the non-stationarity of the dataset. To meet this requirement, a non-stationary method was adopted to calculate the occurrence of flooding events. This approach is becoming increasingly popular for considering the impacts of climate changes on rivers hydrology. The comparison between the outcomes obtained from a stationary and non-stationary GEV approach showed that a flood with equal magnitude has a probability of occurrence, calculated with a non-stationary method, about ten times higher than considering the stationary approach (Figure 2.24). Despite the unquestionable usefulness of such advanced approaches, the results from the non-stationary method are hardly usable and not always clear since the high level of uncertainty they produce.

The evaluation of flood-related field impacts linked with FDC characteristic values and streamflow related to certain return times have been used to fix the thresholds of the defined flood hazard scenarios. Four levels of flood hazard are classified in conformity with the Nigerien codification for flood alert; the categories are: green (normal condition), yellow (frequent flood), orange (severe

flood), and red (catastrophic flood). The extension of flood-prone areas related to each scenario was simulated through hydraulic modelling. This allowed generating flood hazard maps where floodplains are categorized with colouring in conformity to the level of hazard. Beyond to be a piece of fundamental information for the functioning of the EWS, these maps are useful for local urban planners as a guideline to avoid the construction of new buildings into hazardous zones. These recommendations are even more precious in developing countries where the urban fabric is growing as fast as the population growth. The improved urban planning would help new inhabitants to be more aware of the natural hazards affecting their territories. Moreover, using the same codification currently active, it makes the EWS alert immediately understandable for the whole population.

The flood hazard has been proved to be tightly related to changes in climate pattern and recent climatological projections seem to convey that precipitation will increase in near future. Thus, all analyses and results showed in this chapter should emphasize the necessity and motivate the development of effective interventions aimed at the prevention and mitigation of these hydrometeorological hazards.

# Chapter 3

# Climate-Smart Agriculture as adaptive behaviour against hydrometeorological hazards: Rainwater Harvesting Techniques as a flood mitigation strategy

*"Essentially, all models are wrong, but some are useful."*

George Edward Pelham Box

# 3.1   Preface

The work described in this chapter has been partially derived from the paper "*Rainwater harvesting techniques as an adaptation strategy for flood mitigation*" published in the Journal of Hydrology [146], and "*Rainwater Harvesting Techniques to Face Water Scarcity in African Drylands: Hydrological Efficiency Assessment*" published in Water [147].

Sahelian countries are experiencing the harsh climate-related threats, such as frequent droughts, impetuous storms and severe floods, that are especially mining the development of rural populations. The low technological and institutional know-how to rapidly adapt to these threats will cause negative impacts overall socio-economic levels [148]. Thus, impelling is the necessity to find sustainable and, overall, feasible strategies to deal with these natural hazards. knowing the high level of distrust in adopting non-native techniques, the possibility of adopting indigenous RWHT as flood mitigation techniques has been explored. Rainwater harvesting practices have been developed since prehistoric times and they are still an integral part of several agricultural systems throughout the ASA regions [149]. RWHT are substantially composed of two parts: a catchment where the rainfall generates the overland flow, and a target area where the runoff is collected [150].

In order to assess whether RWHT can bring effectively advantages in contrasting the flood hazard, the quantitative assessment of the hydraulic performances of some selected RWHT is addressed in this chapter. The assessment involves the quantification of the capacity in runoff reduction, volume retention and infiltration increase. The goal is achieved through the numerical simulation of the processes occurring during the partition between rainfall and runoff. Two different methodologies are proposed to conduct the hydraulic investigation. The former, rainfall-runoff models are implemented using the hydraulic software HEC-RAS (version 5.0.6) [137]. The model allowed simulating the effect of severe precipitations on two different configurations: (a) the conceptual geometries used to replicate a treated and non-treated farming field (field scale); (b) the morphology of a real watershed (basin scale).

HEC-RAS is a pure hydraulic model, developed for computing free surface flow, mainly into rivers. Hence, it still presents some limitations in the transformation of precipitation in runoff. Intending to overcome such constraints, the second methodology makes the use of the software Iber (version 2.5.1) [151]. This numerical model is able to compute further runoff processes, such as infiltration, and therefore expanding the range of analysis. Moreover, multiple scenarios, typical of Sahelian farmlands, were simulated and a sensitivity analysis

was carried out to understand how physical characteristics of the site affect the RHWT's performances. At the last, the comparison between the two approaches is reported.

Results demonstrate that RWHT are an efficient flood mitigation strategy, reducing up to 87% the runoff overflowing out of farmlands. This effect of retention helps to decrease the amount of water that quickly reach the receptor river, mitigating the rise of the flood wave during severe rainstorms. The correct design is tightly linked to meteorological forces, therefore during the planning phase, all geometrical specifications should be tested against the rainstorms characterizing the rainfall pattern of the selected area.

The sensitive analysis reveals that to gain the maximum benefits from the RWHT is also valuable to combine other surface treatments between the micro-basins.

## 3.2  RWHT technical specifications

During the last thirty years, different researchers have classified the RWHT on the base of specific factors such as size, location, design, etc. Water harvesting systems were meticulously classified by Oweis et al. [62,152] and a detailed list of the most used was reported in the work of Yazar and Ali [153]. A comprehensive overview of the good practices in water harvesting adopted in drylands is given in the compendium of Mekdaschi Studer and Liniger, "Water Harvesting: Guidelines to Good Practice" [63].

Focusing on the RWHT developed in rural areas, these are commonly classified based on the type of catchment used to harvest water:

- Floodwater harvesting: they collect water from a water body (gullies, rivers, lakes);
- Macro-catchment water harvesting: the rainfall is collected in a selected area outside of the farmland;
- Micro-catchment water harvesting: the runoff is directly harvested inside of the farm field.

Among the different categories, this study is focused on micro-catchment RWHT commonly used by smallholder farmers. They can be organized into four main categories related to the type of processing technique (Figure 3.1)
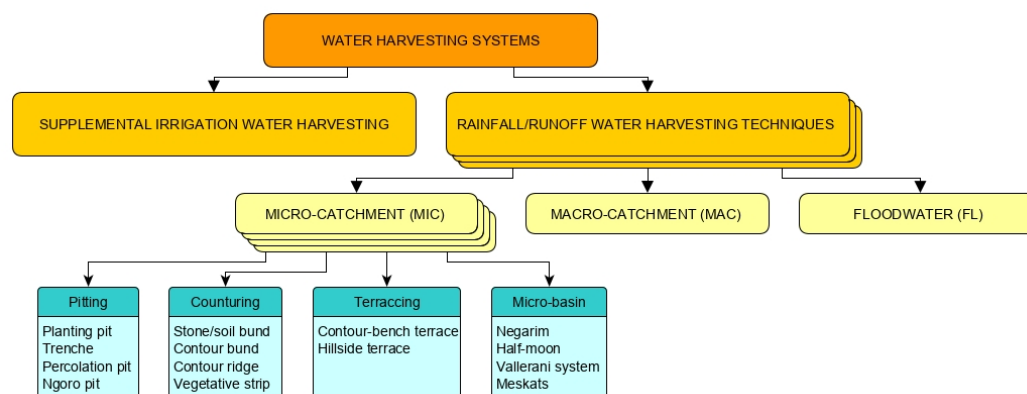
Figure 3.1 Classification of RWHT and the most common on-farm micro-catchment RWHT in sub-Saharan countries (adapted from [153]).

In this work, the authors have analysed 4 different techniques (half-moons, planting pits, hand-dug trenches, Vallerani trenches).

The design and the name of these systems vary depending on the place where the technique has been developed and consequently, it is possible to find different technical features. From 1992, the World Overview of Conservation Approaches and Technologies (WOCAT, [154]) is trying to collect in a consistent, systematic and standardised format the worldwide spread sustainable land management (SLM) knowledge. For its recognized reliability, all technical specifications were extracted from the WOCAT's Global SLM Database where details for each RWHT are reported in Table 3.1.

Table 3.1 Technical specification and spatial arrangement of the analysed RWHT (source: WOCAT).

| | Half-moons [1] | Planting pits [2] | Hand-dug trenches [3] | Vallerani trenches [4] |
|---|---|---|---|---|
| Width/diameter [m] | 4 | 0.2-0.4 | 0.6 | 0.5 |
| Length [m] | - | - | 3.5 | 4 |
| Depth [m] | 0.3 | 0.2 | 0.6 | 0.4 |
| Spacing between structures [m] | 3-4 | 0.8-1 | 4 | 1.6 |
| Vertical interval between structures [m] | 2 | 1 | 3.4 | 5.6 |

Figure 3.2 Pictures of the analysed micro-catchment RWHT (source: WOCAT)

## 3.3    Methodology 1

The procedural steps followed in the implementation of this first methodology are schematized in Figure 3.3. The diagram shows all input data required (specifying among data related to the geometry and the hydrology) and what of them are used to accomplish the analyses at different scales.
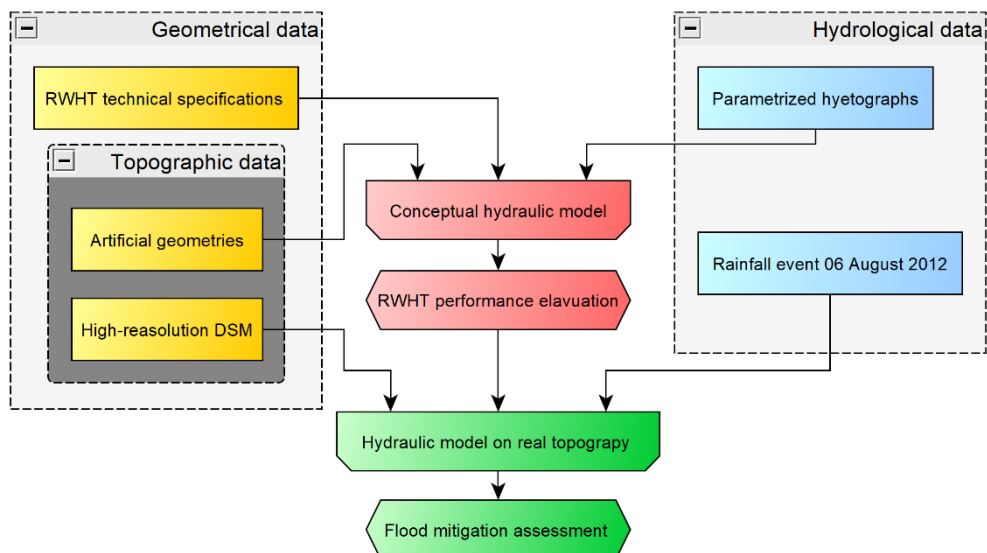


Figure 3.3 Workflow of methodology 1. Colouring: geometrical data (yellow), hydrological data (blue), processing and outcomes related to the conceptual geometries (red) and the real watershed (green).

## 3.3.1 The numerical model

HEC-RAS is a well-known and worldwide used freely accessible hydraulic software [138]. HEC-RAS can perform steady and unsteady 1D and 2D simulations with high compatibility with GIS tools. Throughout the last releases, developers are striving to include hydrological features in a numerical model primarily implemented for pure hydraulic studies. This transition will allow us to adopt a single widely recognized software to accomplish rainfall-runoff analyses. In its version 5.0.6 (currently used in this work), it is possible to follow a workflow called "rain-on-grid". This set up allows to directly apply uniform precipitation over the 2D spatial domain, using hyetographs as boundary conditions. At the present development level, hydrological losses are not embedded yet. Hence, when the rainwater is added on the computational cell, it directly participates to the runoff formation. When runoff is generated, the flow propagation is computed from the resolution of the bi-dimensional Shallow Water (SW) equations in which the continuity is guaranteed by the equation (3.1), written in vector form:

$$\frac{\partial H}{\partial t} + \nabla \cdot hV + S_t = 0 \qquad (3.1)$$

where $H$ is the water surface elevation, obtained from the sum of the bottom surface elevation $z$ plus the water depth $h$, $V = (u, v)$ is the velocity vector, encompassing the two components of velocity u and v in the Cartesian direction, $S_t$ is the source term representing inflow from external sources, such as rainfall.

Instead, the momentum conservation is expressed by equation (3.2), written in vector form:

$$\frac{\partial V}{\partial t} + V \cdot \nabla V = -g\nabla H + v_t \nabla^2 V - c_f V + f \times V \qquad (3.2)$$

where $g$ the gravitational acceleration, $v_t$ is the eddy viscosity coefficient, $c_f$ is the bed friction coefficient, $f$ is the Coriolis parameter. In the case of shallow frictional and gravity flow, the SW system can be simplified by adopting the Diffusion Wave approximation (DSW). This simplification entails the neglection of the eddy viscosity, Coriolis parameter and acceleration terms reducing the momentum equations to a single equation (3.3), where gravitational forces are balanced by friction forces

$$g\nabla H = -c_f V \qquad (3.3)$$

where $\nabla H$ is the water surface elevation gradient. Thus, equation (3.3) shows the link between the horizontal momentum and the water height can be expressed by an empirical relation, like the Manning's equation. Calculating the bed friction with the Manning formulation, the equation (3.3) can be rearranged into the form

$$V = \frac{-\left(\mathcal{R}(H)\right)^{2/3}}{n}\frac{\nabla H}{\sqrt{|\nabla H|}} \qquad (3.4)$$

where $\mathcal{R}(H)$ is the hydraulic radius expressed as a function of the water surface elevation and $n$ is the Manning's coefficient. Placing the velocity determined with equation (3.4) into the mass conservation (3.1) leads to the conventional vector form of DSW of shallow water equations

$$\frac{\partial H}{\partial t} - \nabla \cdot \frac{\left(R(H)\right)^{5/3}}{n\sqrt{|\nabla H|}}\nabla H + S_t = 0 \qquad (3.5)$$

The abovementioned equations are solved through finite-difference and volume methods at every cell of the computational domain. In order to take advantages from the high resolution of the topographic data without excessively increase the computational load, HEC-RAS accounts for the sub-grid bathymetry approach [155,156]. Additional pieces of information are preliminary computed from the high-resolution bathymetry in correspondence of each cell, such as hydraulic radius, volume, and cross-sectional area. This allows storing enough information to go through accurate mass conservation even if calculations are made on a coarser grid. In the framework of DSW, the sub-grid bathymetry form of the continuity equation can be written as

$$\frac{\Omega(H^{n+1}) - \Omega(H^n)}{\Delta t} - \sum_k \frac{\left(R(H)\right)^{2/3}A_k(H)}{n\sqrt{|\nabla H|}}\nabla H \cdot n + S_t = 0 \qquad (3.6)$$

where $\Omega(H)$ is the cell volume and $A_k(H)$ is the face area of the edge $k$, as a function of the surface water elevation. Further details are reported in Brunner, 2016 [137]. All simulations have been carried out using DSW equations.

### *Runoff coefficient estimation*

The most widely used approach to evaluate the water abstraction during rainfall events is the Soil Conservation Service Curve Number (SCS-CN) method [157,158]. This method has already been extensively and successfully used in various studies in Sahelian context [56,159–161]. The SCS-CN method aims to predict the volume of the surface runoff that might be produced from a watershed during a storm, assuring the validity of the hydrological balance. The water balance is written as

$$P = P_e + I_a + I_{cum} \qquad (3.7)$$

where $P$ is the total precipitation, $P_e$ is the runoff depth, $I_a$ is the initial abstraction before ponding and $I_{cum}$ is the cumulative infiltration after runoff begins. Considering that for a rainfall event, $P_e$ must be always less than or equal to $P$ and $I_{cum}$ is less than or equal to a potential maximum retention $S$ (soil storage capacity), the proportion between these quantities is assumed as

$$\frac{P_e}{P - I_a} = \frac{I_{cum}}{S} \qquad (3.8)$$

From the previous two equations, it is derived the basic equation for computing the runoff

$$P_e = \frac{(P - I_a)^2}{P - I_a + S} \quad for \; P > I_a \quad otherwise \quad P_e = 0 \qquad (3.9)$$

The initial abstraction is conventionally substituted by the empirical relation which bond it with the soil storage

$$I_a = 0.2\,S \qquad (3.10)$$

obtaining

$$P_e = \frac{(P - 0.2\,S)^2}{P + 0.8\,S} \qquad (3.11)$$

The features of the analysed basin, such as land uses and soil characteristics, are summarized into a non-dimensional coefficient, called Curve Number ($CN$), which is related to the S by

$$CN = \frac{100}{S/S_0 + 1}$$
(3.12)

where $S_0 = 254$ is a parameter to convert the unit from inches to millimetres. $CN$ defines the permeability rate of the analysed soil, ranging from 100 (impervious) to 0 (totally permeable). Hence, higher is the value of $CN$ and bigger is the fraction of rainfall that generates runoff.

In this study the SCS-CN method was not conventionally used to estimate the amount of runoff, instead, it was inversely used to evaluate the value of $CN$ correspondent to the runoff attenuation of each analysed configuration. Indeed, the volume of runoff is already derived as result from the numerical simulations. Knowing the runoff depth $P_e$ and rainfall amount $P$, it is possible to define the Runoff Coefficient $R_c$ as

$$R_c = \frac{P_e}{P}$$
(3.13)

The value of $R_c$ will give the evaluation of the efficiency in terms of runoff mitigation among the different configurations.

### *Statistics*

In order to investigate the relation between geometrical features and hydraulic performance of the RWHT analysed, the statistical dependence between these variables has been searched. The Pearson's correlation coefficient was applied to evaluate the linear correlation between variables. Correlation coefficient values range from -1 to 1, where ±1 is the perfect positive (or negative) correlation and 0 states the absence of correlation (independent variables).

## 3.3.2 Model set up

### *Geometrical data*

The former step in the implementation of a hydraulic model is the description of the spatial domain. Two different topographic bases have been manipulated to obtain the input geometries used for the hydraulic analyses.

Firstly, to schematize a portion of farmland with and without RWHT, a conceptual hydraulic model was implemented using a series of artificial geometries. These geometries were built shaping the selected RWHT on a plain

square of 1 ha, with a constant slope of 1%. From the four analysed RWHT, eight configurations have been developed following two geometrical layouts: (a) aligned rows and (b) staggered rows. An unmodified plain square was kept as reference geometry to carry out comparisons between the different configurations. Thus, a total number of 9 configurations have been investigated. An identification code has been matched to each configuration and it will be used along the text to identify the outcomes related to each simulated configuration (Table 3.2).

All geometries have been edited using the processing tools of QGIS v3.4.0 (Quantum Geographic Information System, [162]).

Table 3.2 Identification code of the different configurations used as geometry input of the conceptual hydraulic model.

| Identification code | Configuration |
| --- | --- |
| U-PS | Unmodified plain square |
| A-HM | Aligned half-moons |
| S-HM | Staggered half-moons |
| A-PP | Aligned planting pits |
| S-PP | Staggered planting pits |
| A-HT | Aligned hand-dug trenches |
| S-HT | Staggered hand-dug trenches |
| A-VT | Aligned Vallerani trenches |
| S-VT | Staggered Vallerani trenches |

Geometrical scheme of the configurations analysed is displayed in Figure B.1 (see Appendix B).

Secondly, hydraulic simulations were carried out on a real watershed next to the village of Touré, Niger. The settlement is located along the left bank of the Sirba River, the main tributary of the Middle Niger River Basin (Figure 3.3). Its inhabitants have been affected by floods several times during the last decades, with important losses of houses, cattle, and assets [38,98]. The topography is represented by the digital surface model (DSM) of the riverine territory. The DSM was elaborated during aerial surveys with a UAV by Belcore et al. [163] at the end of the wet season 2018. The DSM has a high level of resolution of 8 cm. Since the riverine territory is characterized by the presence of a series of gullies flowing into the river, a hydrological analysis was carried out to delineate the watersheds that collect rainwater into each gully. The elevation model of the widest identified catchment (26 ha) has been used to implement the hydraulic model on a real geometry. Successively, the DSM of the basin was modified in order to simulate the presence of RWHT on a farming area. The target agricultural

field (highlighted with a yellow shade in Figure 3.4) was identified from the high-resolution aerial photos shot during the abovementioned data collection campaign. The target area covers a portion of 5% of the whole watershed.

Outcomes from the hydraulic model will be identified with the name "original" and "modified", respectively, having as geometry input the unmodified DSM and the modified DSM.
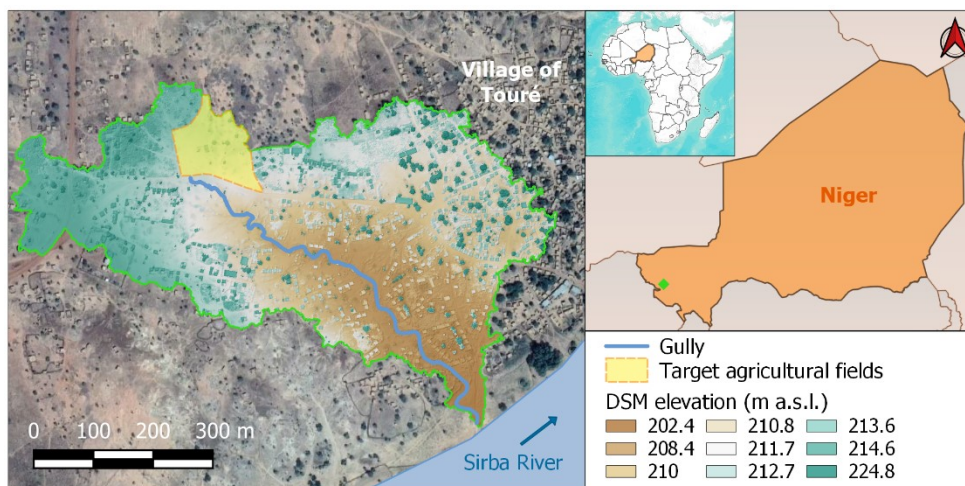


Figure 3.4 Geolocation, topography, and hydrography of the analysed watershed.

### Hydrological data

The Sahelian regions are cyclically struck by severe storms every wet season. These hydrometeorological hazards have been closely studied by many researchers since they are among the most powerful on the planet, with intensities exceeding hundreds of mm per hour [23]. These hydrometeorological extremes are the causes of dangerous floods that affect African's assets. Thus, extreme and heavy rainstorms have been the target inputs of our hydraulic simulations. A deep investigation of these events is reported in the study of Panthou et al. [18]. In the analysed study region, extreme events have been quantified as precipitation with a rainfall depth of 40 mm that occurs on average less than 2.5 times per year. Instead, heavy rainfalls are characterized by total precipitation of 20 mm and a yearly occurrence of 10 times. Sahelian rainstorms show an evolutive trend typical of an Organized Convective System (OCS), in which the front of the convective cell brings the mayor part of the rain and it is followed by a stratiform trail [164]. Hyetographs produced by this convective systems are organized in two well-defined intervals: a high-intensity peak (often with a duration lesser of an hour) followed by a low-intensity constant tail (Figure 3.5). The shape of OCS

hyetograph lends itself well to being disaggregated and parameterized to obtain a reconstructed realistic hyetograph. In order to obtain a representative hyetograph for both extreme and heavy rainfall, the disaggregation model proposed in the study of Balme et al. [23] was chosen to create the source inputs for the rainfall-runoff model. The model was developed and calibrated for the super-instrumented site around Niamey (Niger). This area is located in the heart of the Sahel and well represents the typical rainfall regime that characterizes sub-Saharan drylands. The site, together with two other sites situated in Mali and Benin, is part of a densely instrumented observation network dedicated to monitoring of hydrological, climatological and ecological changes in West Africa [165,166].

The disaggregation model is based on a conceptual hyetograph (see Figure 3.5) in which the shape, i.e. the distribution of rainfall intensity in time, is defined by 5 parameters all related to the total event rainfall $R$. The 5 parameters are computed as follows:

1. $R_c = a \cdot R + b$
2. $I_m = c \cdot R + d$
3. $R_s = R - R_c$
4. $D_c = 2 \cdot R_c / I_m$
5. $D_t = D_c + R_c / I_s$
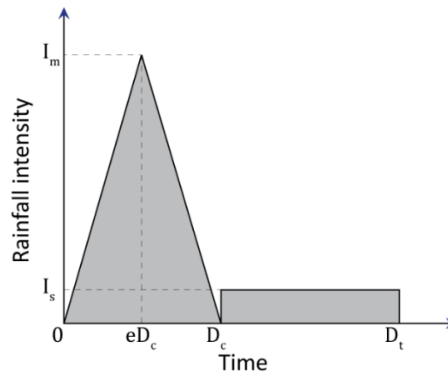


Figure 3.5 Disaggregated hyetograph.

where $R_c$ is the total precipitation of the convective part, $I_m$ is the maximum rainfall intensity, $R_s$ is the total precipitation of the stratiform part, $D_c$ is the duration convective of the convective part, $D_t$ is the total duration of the rainfall event and $I_s$ is the stratiform intensity. The coefficients, that were calibrated optimizing the efficiency of the disaggregated hyetograph to simulate the real precipitation events, are $a$=0.89, $b$=-0.08, $c$=2.01, $d$=0.53, $e$=0.5 and $I_s$=1.5 mm/h. The peculiarity of such model lies in the accurate replication of the peak rainfall intensity, the variable that mostly affects the runoff generation in this kind of arid and semi-arid environment.

The conceptual hyetographs for the two analysed events are displayed in Figure 3.6.
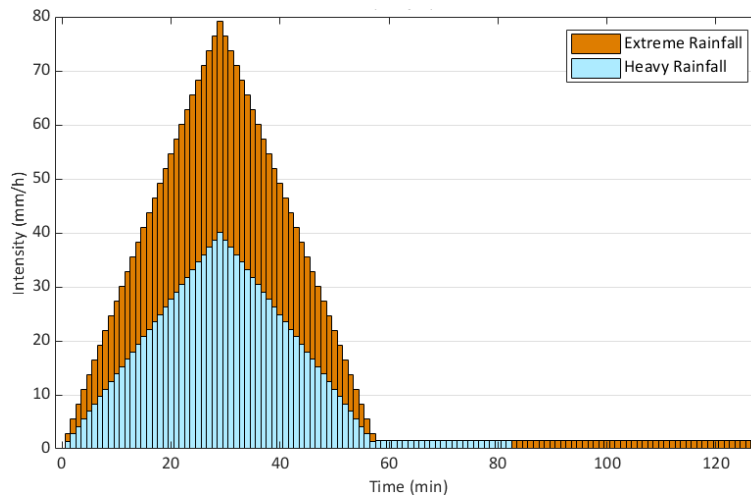
Figure 3.6 Conceptual hyetographs simulating the heavy and extreme rainfall events.

In order to test the proposed methodology on a real case, a small watershed located in the village of Touré (Niger), we collected the records of one of the worse years for the central Sahel, 2012. 2012 was characterized by high magnitude downpours which markedly increased the water level of Niger River, and its tributaries, giving rise to the highest flood ever registered in the Middle Niger Basin. The hyetograph with the highest intensity of the wet season 2012 was selected from the nearest rain-gauge station – Koyria station (13.76 N, 1.69 E, see Figure A.1) – to the village of Touré. Figure 3.7 displays the temporal distribution of the rainfall intensity during the event in which can be immediately recognized the typical OCS structure. The event was characterized by total precipitation of 49.7 mm, of which 92% fell during the first 50 minutes and a rainfall intensity peak of 162 mm/h. In Figure 3.7 is also reported the mean monthly rainfall for the twenty-year period 1997-2016 at the same station. The trend shows that on average the wet season begins between May and June, with sporadic rains in April, and usually ends in September or beginning of October. Most of the precipitation is concentrated in August.
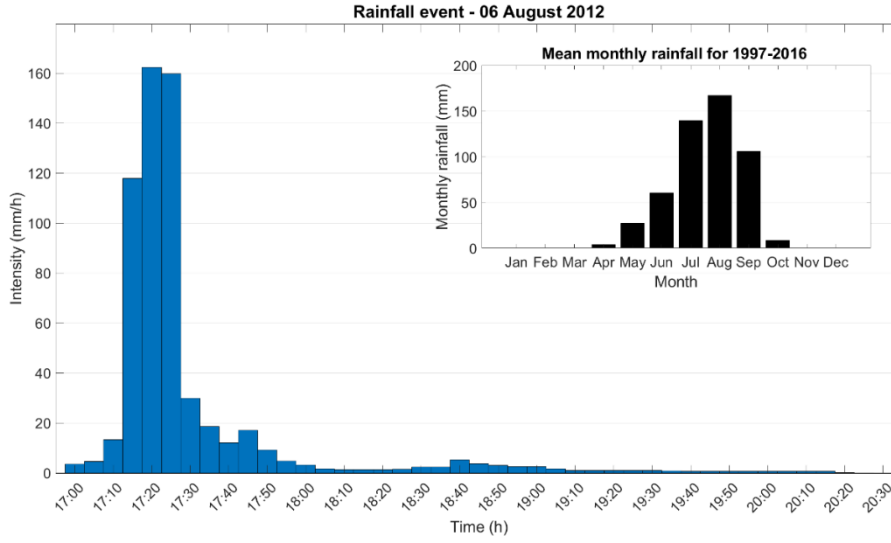
Figure 3.7 Rainfall intensity of the rainstorm of 06 August 2012 and mean monthly rainfall for the twenty-year period 1997-2016 at the Koyria station. The high intensity highlights the power of rainstorms that frequently strike these regions.

### Hydraulic efficiency estimation

The influence induced using RWHT to the overland flow dynamics was evaluated in terms of two different efficiency measures:

- Flow peak reduction: calculated as the reduction on the maximum flow rate that flows out of the domain with and without the implementation of RHWT ($Q.max_{RWHT}$ and $Q.max_{U-PS}$ respectively)

$$FPR = \left(1 - \frac{Q.max_{RWHT}}{Q.max_{U-PS}}\right) \cdot 100 \qquad (3.14)$$

- Volume reduction: calculated as the reduction on the cumulated volume of water that flows out of the domain with and without the implementation of RHWT ($Vol.out_{RWHT}$ and $Vol.out_{U-PS}$ respectively)

$$VR = \left(1 - \frac{Vol.out_{RWHT}}{Vol.out_{U-PS}}\right) \cdot 100 \qquad (3.15)$$

### 3.3.3 Results

### Conceptual model: RWHT performance evaluation

The hydraulic simulations showed up the different response of each RWHT to hydrometeorological pressures. The hydraulic performances of the analysed

RWHT were evaluated through comparisons between the outcomes coming from the different configurations.

The first hydraulic performance evaluated is the flow peak reduction related to each configuration. The calculated hydrographs at the outlet are displayed in Figure 3.8 showing how each RWHT configuration reacts to rainfall events.
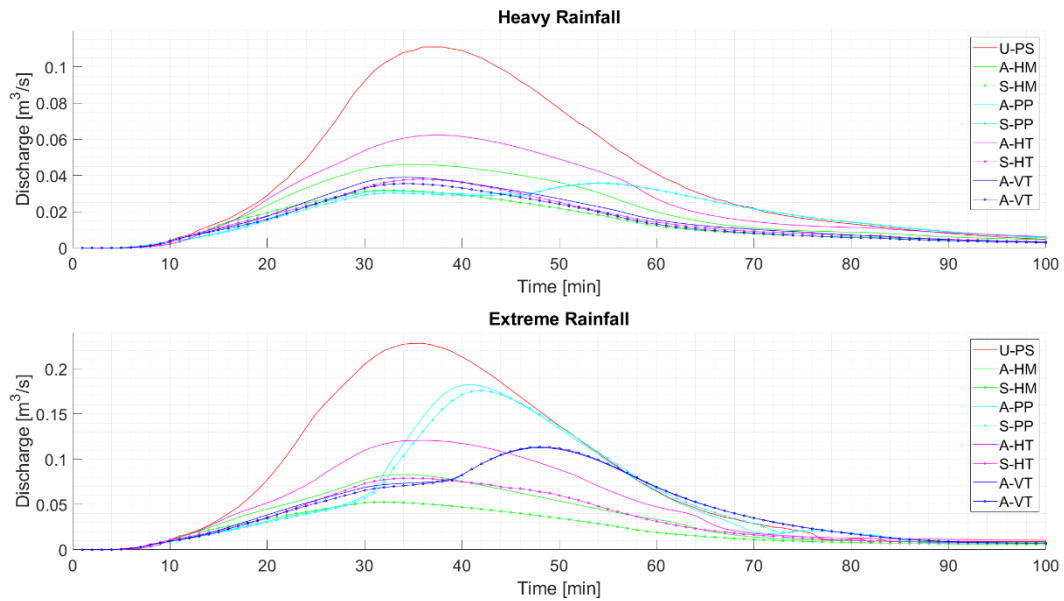


Figure 3.8 Hydrographs for the two parametrized rainfall events.

The maximum discharge with the related $FPR$ per each output is reported in Figure 3.9.
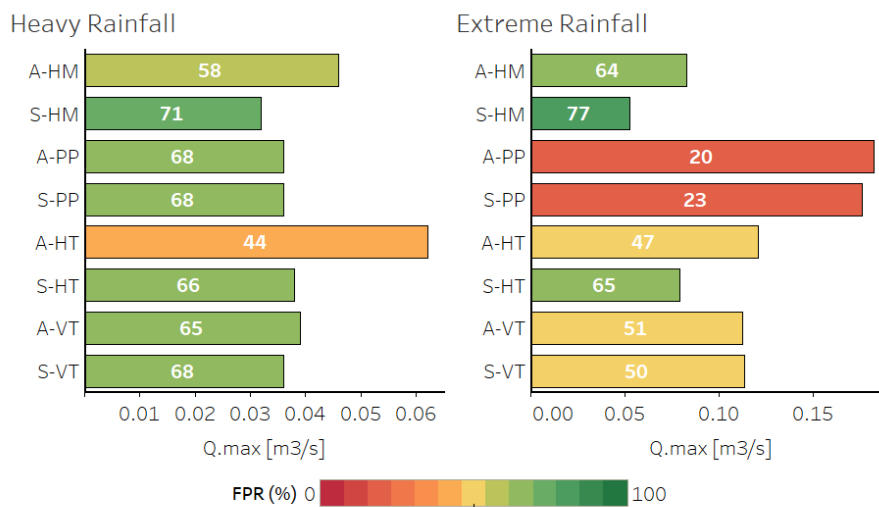


Figure 3.9 Simulation outcomes: $Q.max$ and $FPR$ for each configuration. Colouring: from the worst performance (red) to the best performance (green).

77

Both hydrographs and *FPR* demonstrate that the configuration S-HM (staggered half-moons) has the best performance. Indeed, the value of flow peak reduction is higher than 70% for both rainfall events.

Relevant is the difference in the performance of the two smallest RWHT, A-PP and S-PP. Observing the trend of the hydrograph can be highlighted two marked phases: before the filling and after the filling of the storage volume (see Figure 3.10). Before the filling, planting pits strongly slow the flow being homogeneously distributed on the ground. Despite this optimal behaviour, the small size of the ponds cannot retain a large amount of water and when pits are filled the global friction decreases and the outgoing discharge quickly increases.
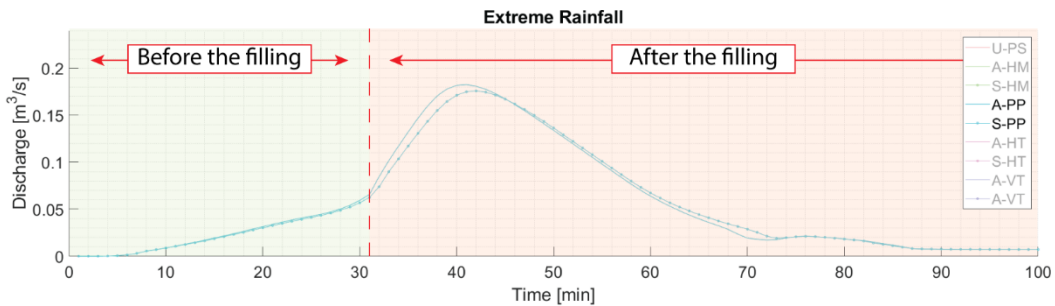


Figure 3.10 Focus on the hydraulic behaviour of PP configurations. The green area covers the range in which PP are not filled and still able to collect runoff. The red area highlights the range in which the retention capacity of PP is exhausted, and the flow reduction fails.

Figure 3.11 displays the different behaviour of the overland flow during the two phases. Before reaching the maximum storage capacity of RWHT, the flow vectors move towards the ponds; after the filling, the water inside of each basin is still and the runoff coming from upstream is deflected towards downstream. This phenomenon is equivalent to the "*principles of non-uniform floodplain storage*" explained in the Principles of River Engineering [167], where the volume of the flow wave exceeds the storage volume.
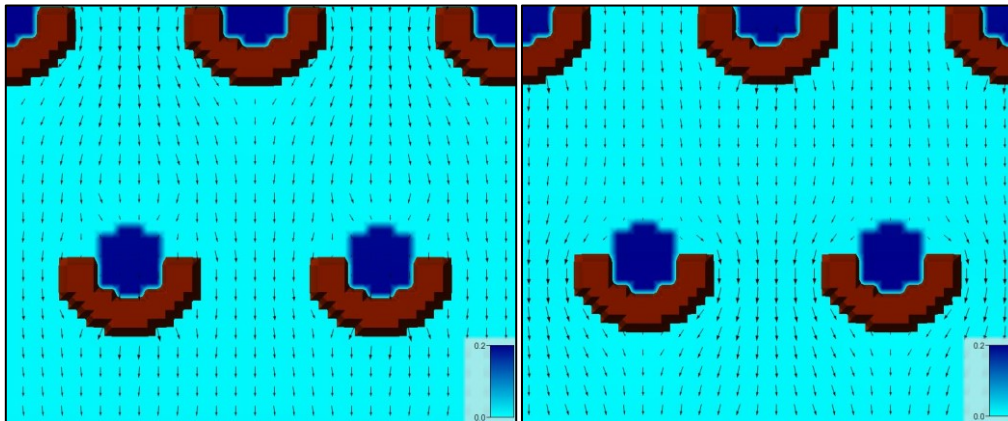
Figure 3.11 Extract from a hydraulic simulation with S-PP configuration. On the left: velocity vectors before filling. On the right: velocity vectors after filling. Colouring: water depth values from 0 (light blue) to 0.2 m (dark blue).

For the heavy rainfall, the A-PP and S-PP hydrographs show a "chopped head" wave up to the minute 46, then the retention capacity fails and the discharge increases. Instead, for the extreme rainfall, this behaviour is much more marked leading to a slight $FPR$ (20-23%). Indeed, the storage capacity already run out at minute 31. This behaviour can be observed also for the A-VT and S-VT. Both configurations fail in case of the extreme event showing an evident increase from the minute 39 to 49. On the contrary, heavy rainfall does not use up all the retention capacity of the Vallerani technique, avoiding the abrupt change of slope in the outflow hydrographs. Instead, even if with a different level of $FPR$, both HM and HT do not reach the overfilling.

The second performance evaluated is the volume reduction ($VR$) at the end of each simulation. Figure 3.12 displays the cumulated volume over time of each simulation.
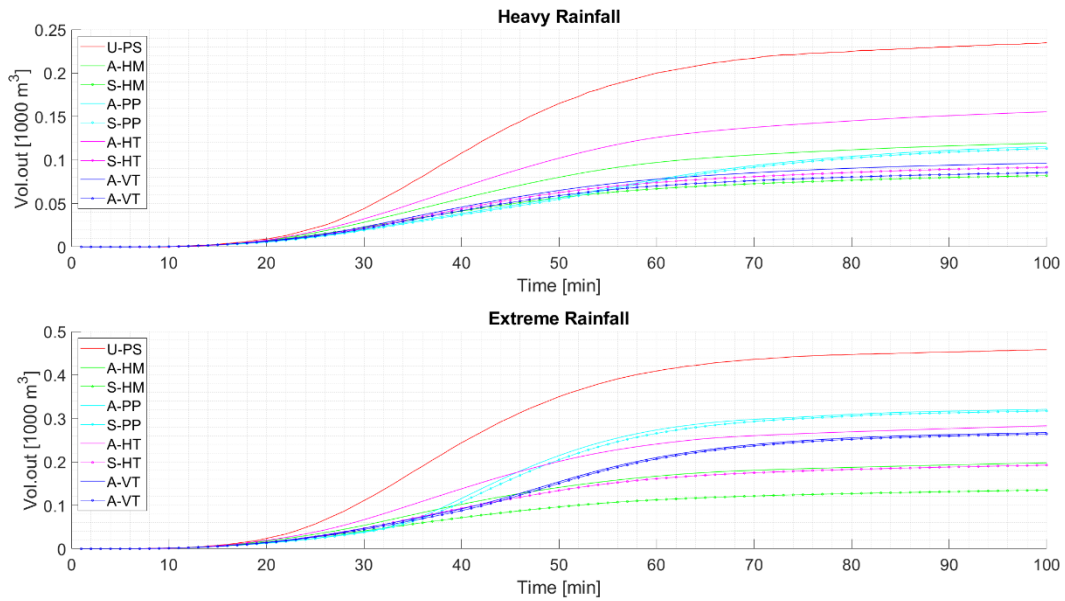
Figure 3.12 Cumulated volume for the two parametrized rainfall events.

The total volume flowed out of the domain during the simulation with the related $VR$ per each configuration is summarized in Figure 3.13.
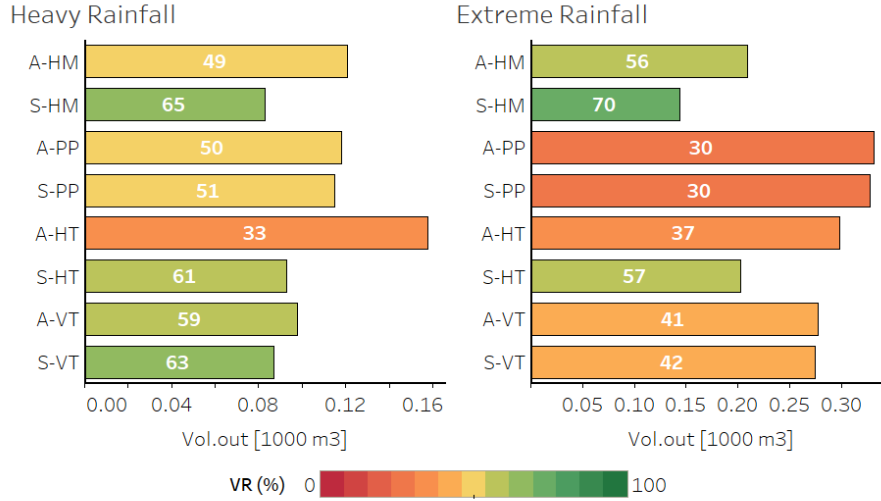


Figure 3.13 Simulation outcomes: $Vol.out$ and $VR$ for each configuration. Colouring: from the worst performance (red) to the best performance (green).

The difference between $Vol.out_{RWHT}$ and $Vol.out_{U-PS}$ quantifies the amount of retained volume by each RWHT. The retained volume is water that does not reach immediately the receptor water body (the main river or its tributary), slowing down the growth of the flood wave. As well as the previous performance, the values of $VR$ confirm that S-HM has the best performance and it intercepts a greater amount of runoff than the other configurations. S-HM and S-

VT have almost the same power of retention against heavy rainfall. Instead, for extreme rainfall, the $VR$ of HM increase due to their capability of collecting the whole runoff while the volume reduction of VT sharply drops down since they finish their storage capacity. A marked reduction in performances of 20% can be noticed for both PP and VT when the magnitude of the rainstorm increase.

Hydraulic simulations allowed to perform the transformation of the rainfall to runoff, calculating the partition between the volume of water retained by RWHT and the total amount of water flowed out the domain. Knowing this latter, the concept behind the SCS-CN was exploited to goes back to the value of CN that characterizes the modified surface. Moreover, it was possible to evaluate the relative runoff depth, meaning the net amount of precipitation that generated the cumulated volume. The outcomes are listed in Table 3.3.

Table 3.3 Curve Number of each configuration and the related runoff depth.

|  | Heavy Rainfall | | Extreme Rainfall | |
| --- | --- | --- | --- | --- |
|  | $CN$ [-] | $P_e$ [mm] | $CN$ [-] | $P_e$ [mm] |
| U-PS | 100 | 20 | 100 | 40 |
| A-HM | 95.4 | 10.3 | 89.2 | 17.7 |
| S-HM | 92.6 | 7 | 84.5 | 12.2 |
| A-PP | 95.1 | 10 | 95.3 | 28.2 |
| S-PP | 95 | 9.8 | 95.2 | 27.8 |
| A-HT | 97.2 | 13.4 | 93.9 | 25.3 |
| S-HT | 93.4 | 7.9 | 88.8 | 17.2 |
| A-VT | 93.8 | 8.3 | 93 | 23.6 |
| S-VT | 92.9 | 7.3 | 92.8 | 23.3 |

Since that SCS-CN method is based on a relation between $P$ and $P_e$ that follows a power-law (equation (3.11)), for a small amount of precipitation a slight variation of the $CN$ produces a great change of $P_e$. This means that, for example, precipitation of 40 mm on a field with staggered half-moons (Table 3.3, third row) produces the same runoff of an event with an amount of rainfall of 12 mm on a non-treated surface. On the other hand, the same amount of runoff can be observed on a surface with RWHT for rainfall events with an intensity much higher than on a plain surface. This asserts the capacity of RWHT to mitigate the dangerous impacts of rainstorms.

These results can be translated into the variation of runoff coefficient related to each adopted technique. The $R_c$ values are summarized in Table 3.4. Focusing on the most efficient practice, the application of staggered half-moons on a completely crusted soil (almost waterproof with a $R_c$ close to one) could lead to a

significative reduction of the runoff coefficient meaning that only one-third of the total amount of rain will flow downstream the cultivated field. On the contrary, PP with an $R_c$ of 0.7 can collect into the field only one-third of the precipitation allowing the rest of the water to leave the field as overland flow.

Table 3.4 Runoff coefficient for each configuration analysed.

|  | **Heavy Rainfall** | **Extreme Rainfall** |
|---|---|---|
|  | $R_c$ [-] | $R_c$ [-] |
| U-PS | 1 | 1 |
| A-HM | 0.51 | 0.44 |
| S-HM | 0.35 | 0.3 |
| A-PP | 0.5 | 0.7 |
| S-PP | 0.49 | 0.7 |
| A-HT | 0.67 | 0.63 |
| S-HT | 0.39 | 0.43 |
| A-VT | 0.41 | 0.59 |
| S-VT | 0.37 | 0.58 |

To evaluate whether the hydraulic efficiency of the analysed configurations is directly correlated to the design of the technique itself, a series of correlations have been explored. The most characterizing feature of each RWHT is the volume dug to build of the single micro-catchment, named excavation volume ($EV$). For this reason, the correlation between $FPR$, $VR$ and this geometrical feature has been investigated.

In a first attempt, the whole set of outcomes was evaluated and the correlation coefficients calculated are listed in Table 3.5.

Table 3.5 Correlation of $EV$ with $VR$ ($EV - VR$) and with $FPR$ ($EV - FPR$). The Pearson's correlation coefficient ($\rho_p$).

|  |  | $\rho_p$ |
|---|---|---|
| Heavy Rainfall | $EV - VR$ | 0.1 |
|  | $EV - FPR$ | -0.247 |
| Extreme Rainfall | $EV - VR$ | 0.886 |
|  | $EV - FPR$ | 0.909 |

The results show a discrepancy between the two simulated rainfall events. For extreme rainfall, all coefficients are close to 1 meaning that a significant correlation with both $VR$ and $FPR$ exists. Conversely, for heavy rainfall seems do not exist any correlations between the variables. To deeply understand whether the geometrical arrangement affects the analysis, correlation coefficients have

been calculated considering separately each configuration. The results are reported in Table 3.6.

Table 3.6 Correlation of $EV$ with $VR$ ($EV - VR$) and with $FPR$ ($EV - FPR$) for the two geometrical arrangements. The Pearson's correlation coefficient ($\rho_p$).

|  |  |  | $\rho_p$ |
| --- | --- | --- | --- |
| Heavy Rainfall | Aligned configuration | $EV - VR$ | -0.267 |
|  |  | $EV - FPR$ | -0.536 |
|  | Staggered configuration | $EV - VR$ | 0.83 |
|  |  | $EV - FPR$ | 0.524 |
| Extreme Rainfall | Aligned configuration | $EV - VR$ | 0.911 |
|  |  | $EV - FPR$ | 0.902 |
|  | Staggered configuration | $EV - VR$ | 0.993 |
|  |  | $EV - FPR$ | 0.967 |

According to the previous finding highlighted in Table 3.5, the strong positive correlation in case of an extreme event is also confirmed analysing separately the two geometrical configurations, $\rho_p$ always greater than 0.9. Observing the heavy rainfall, performances of staggered configurations show a visible correlation with $EV$. Instead, no correlation can be found for the aligned configuration. The demonstration can be found in the different behaviour of RWHT for the two geometrical configurations. Indeed, A-HM and A-HT show a much lower efficiency than the staggered equivalent.

### *Real watershed: flood mitigation assessment*

The results showed in the previous section have demonstrated that staggered half-moons configuration has the best hydraulic performances in terms of flow peak and volume reduction. Therefore, the optimal choice to decrease the $R_c$ of a target surface. In light of these reasons, S-HM was chosen as RWHT to be tested on the real topography, simulating what would happen whether the farmland owner decided to apply this technique.

Hydraulic simulations were carried out using as input geometry the original and modified topography. Figure 3.14 displays how the original surface has been modified with the addition of staggered half-moons and how the presence of these techniques affects the surface runoff.
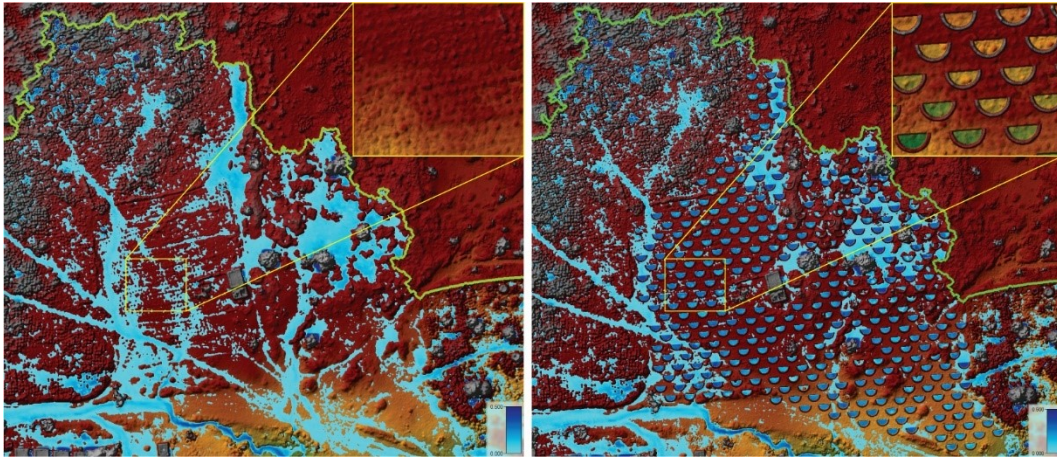
Figure 3.14 Overland flow pattern for the original (on the left) and modified (on the right) topography. Both images display the water depth at the peak of the rainfall event (colouring: from light blue = 0.05 m to dark blue = 0.5 m). The enlargements on the top-right part put emphasis on the morphological alterations applied to create the modified topography.

Three scenarios have been analysed: the two parametrized rainfall events and the rainstorm occurred on 06 August 2012. The precipitation was homogeneously distributed over the whole watershed and the outflow has been calculated at the closure section of the basin. The outcomes calculated for the two topographical inputs have been compared. Hydrographs are reported in Figure 3.15.
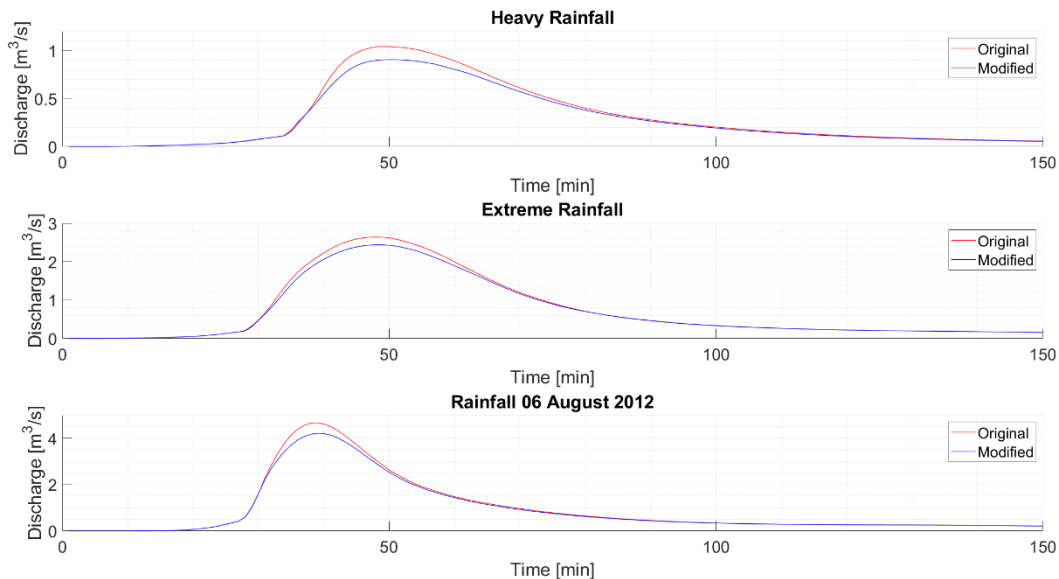


Figure 3.15 Hydrographs calculated for the three analysed scenarios.

The shapes of the hydrographs are similar for the three scenarios, with the occurrence of the flood wave peak after 48 minutes and 36 minutes, respectively for parametrized hyetographs and real rainfall, from the beginning of the event.

The mitigation effect of the RWHT leads to the generation of smoother flood wave along the basin. Despite only the 5% of the basin surface was treated with S-HM, all hydrographs show a significant $FPR$ around 10% highlighting the benefit of the presence of RWHT (see Table 3.7). Conversely to the results obtained for the conceptual model, in this configuration S-HM show a higher $FPR$ against a heavy rainfall than an extreme rainfall.

Table 3.7 Simulation outcomes: $Q.max$ and the related $FPR$ for both configurations.

|  |  | **Heavy Rainfall** | **Extreme Rainfall** | **Rainfall 06 August 2012** |
|---|---|---|---|---|
| Original | $Q.max$ [m³/s] | 1.041 | 2.641 | 4.668 |
| Modified | $Q.max$ [m³/s] | 0.905 | 2.447 | 4.214 |
|  | $FPR$ [%] | 13% | 7% | 10% |

In terms of $VR$, the modified layout shows a decrease in performance as the intensity of the rainfall increases. It can be visualized by the increasing closeness of the original and modified $Vol.out$ trends in Figure 3.16.
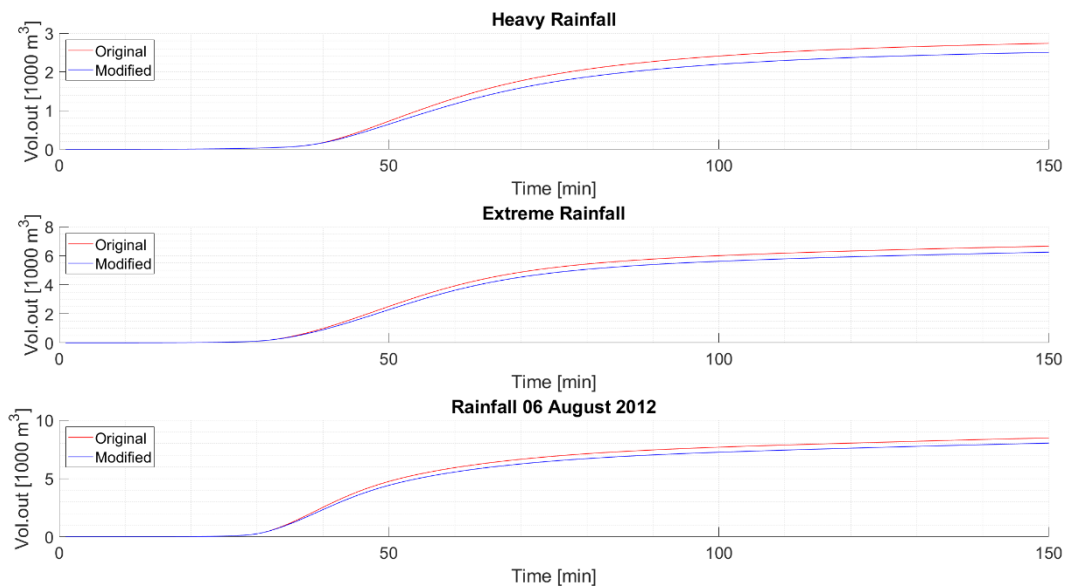


Figure 3.16 Cumulated volume for the three analysed scenarios.

The quantification of the $VR$ is reported in Table 3.8. This negative trend is due to that most of half-moons have been overfilled by the increasing overland flow coming from the headwater during the event.

Table 3.8 Simulation outcomes: $Vol.out$ and the related $VR$ for both configurations.

|  |  | **Heavy Rainfall** | **Extreme Rainfall** | **Rainfall 06 August 2012** |
|---|---|---|---|---|
| Original | $Vol.out$ [1000 m³] | 2.868 | 7.005 | 8.98 |
| Modified | $Vol.out$ [1000 m³] | 2.628 | 6.584 | 8.537 |
|  | $VR$ [%] | 8% | 6% | 5% |

Comparing the values of $FPR$ and $VR$ can be noticed that they have not the same trend (see Table 3.7 and Table 3.8). Observing the $FPR$, S-HM seems to be more efficient for the real rainfall even though the magnitude ($P \approx 50$ mm) is higher than the extreme rainfall ($P=40$mm). This is due to the shorter duration of the event which allows collecting the initial runoff more efficiently. Focusing on the real event, S-HM configuration performs a marked reduction of the flood peak reducing the hazard level over the basin. Notwithstanding this positive aspect, it leads to a slight volume reduction with does not significantly mitigate the rising of the water level at the confluence with the main river.

As previously done, these results were converted in the alteration of the runoff coefficient characterizing the area. The $R_c$ values evaluated for the three scenarios are reported in Table 3.9.

Table 3.9 Simulation outcomes: $Vol.out$ and the related $VR$ for both configurations.

|  |  | **Heavy Rainfall** | **Extreme Rainfall** | **Rainfall 06 August 2012** |
|---|---|---|---|---|
| Original | $R_c$ [-] | 0.54 | 0.66 | 0.68 |
| Modified | $R_c$ [-] | 0.5 | 0.62 | 0.65 |

In accordance with $VR$, $R_c$ values show an opposite trend concerning the precipitation intensity.

## 3.4 Methodology 2

The procedural steps followed in the implementation of the second methodology are schematized in Figure 3.17. The diagram shows all input data required (specifying among data related to the geometry, the hydrology and model's parameters varied during the Monte Carlo analysis) and the phases followed to achieve the hydrological efficiency estimation of the analysed RWHT.
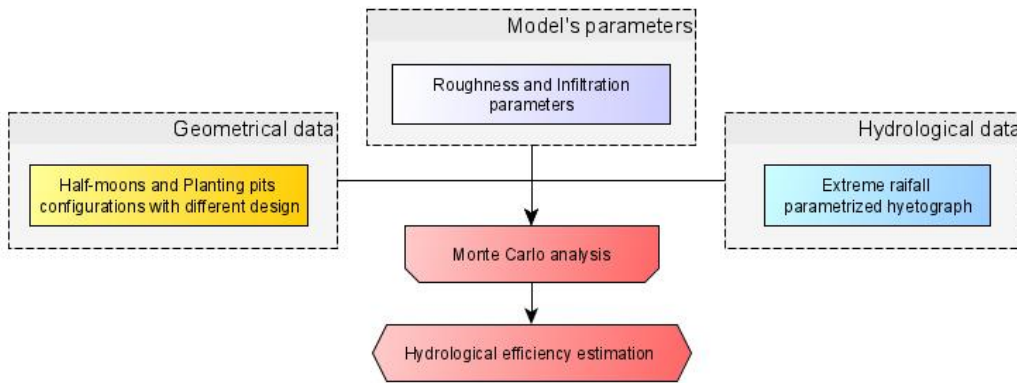


Figure 3.17 Workflow of methodology 2. Colouring: geometrical data (yellow), hydrological data (blue), model's parameters (violet), processing and outcomes related to the conceptual geometries (red).

### 3.4.1 The numerical model

Iber is a two-dimensional distributed model originally developed for hydraulic computations of overland and river flow [151,168], and later on, expanded to the simulation of hydrological processes of rainfall-runoff transformation [169,170], and subsurface flow [171,172]. The surface runoff depth and velocity fields are obtained from the resolution of the 2D Shallow Water (SW) equations, computing the bed friction with the Manning formulation, and including rainfall and infiltration as source terms. The equation system can be written as follows:

$$\frac{\partial h}{\partial t} + \frac{\partial q_x}{\partial x} + \frac{\partial q_y}{\partial y} = R - I$$

$$\frac{\partial q_x}{\partial t} + \frac{\partial}{\partial x}\left(\frac{q_x^2}{h}\right) + \frac{\partial}{\partial y}\left(\frac{q_x q_y}{h}\right) = -gh\frac{\partial z_s}{\partial x} - g\frac{n^2}{h^{7/3}}|\boldsymbol{q}|q_x \qquad (3.16)$$

$$\frac{\partial q_y}{\partial t} + \frac{\partial}{\partial y}\left(\frac{q_y^2}{h}\right) + \frac{\partial}{\partial x}\left(\frac{q_x q_y}{h}\right) = -gh\frac{\partial z_s}{\partial y} - g\frac{n^2}{h^{7/3}}|\boldsymbol{q}|q_y$$

where $h$ is the water depth, $q_{x,y}$ are the unit discharge components along x and y, respectively, $R$ is the rainfall intensity, $I$ is the infiltration rate, $g$ is the gravity acceleration, $z_s$ is the free surface elevation and $n$ is the roughness coefficient of Manning. The model equations are solved with a finite volume solver on an unstructured computational grid. The numerical scheme adopted for the calculation of hydraulic variables is a variant of the decoupled hydrological discretization (DHD) scheme [169], internally called DHD_basin. Unlike the DHD scheme, the DHD_basin directly calculates the water level at the wet-dry fronts as the linear interpolation between the free surface elevation of the wetted node and the bed elevation of the dry node. For further details on the model equations and numerical schemes see the studies of Cea and Bladé [151,168,169].

The infiltration term $I$ is calculated through the Green-Ampt formulation [173]. The method directly relates the infiltration losses to the surface hydraulic conditions, computed through the resolution of SW equations, and the physical properties of the soil. The Green-Ampt method is based on the assumption that exists a sharp boundary (wetting front) which divides the upper saturated soil layer, next to the surface, from the lower unsaturated soil layer characterized by a soil moisture content of $\theta$. As water penetrates the ground, the wetting front descends to a depth $L$, representing the thickness of the saturated region. The infiltration rate ($I$) and cumulative infiltration ($I_{cum}$) are computed as:

$$I(t) = k_s \left( 1 + \frac{(h + \Psi)}{L(t)} \right)$$

$$I_{cum}(t) = \int_0^t I(t)\, dt$$

(3.17)

in which

$$L(t) = \frac{I_{cum}(t)}{\Delta\theta} \qquad \Delta\theta = \eta - \theta_i \qquad (3.18)$$

The physical parameters that describe the soil are the saturated hydraulic conductivity ($k_s$), the suction head in the non-saturated layer ($\Psi$), the soil porosity ($\eta$), and the initial soil moisture content ($\theta_i$). The infiltration rate tends to the value of $k_s$ when the entire soil layer reaches the saturation ($\theta = \eta$).

*Statistics*

In order to investigate the correlation between physical features and hydraulic performance of the analysed domains, the statistical dependence between these variables has been searched. The Spearman's correlation coefficient was calculated to evaluate the correlation between variables. The coefficient values range from -1 to 1, where ±1 is the perfect positive (or negative) correlation and 0 states the absence of correlation.

## 3.4.2 Model set up

*Geometrical data*

The geometrical inputs that have been used to represent each RWHT follow the conceptualization of the agricultural field delineated in the section "*Geometrical data*" of the previous method. For this analysis, we have focused on the 2 most used micro-catchment RWHT (half-moons and planting pits) as described in the guidelines of Mekdaschi Studer and Liniger [63]. Frequently, semi-circles with a radius of 4 meters, spaced 2 meters, are dug for half-moons, while circles with a diameter of 0.4 meters, spaced about 1 m apart in each direction, are dug for small planting pits. The geometrical schemes and features of the spatial domains are reported in Figure B.2 (see Appendix B).

The outcomes presented for the first methodology revealed that exists a strong correlation between hydraulic performances and the storage volume (excavated volume) of each micro-catchment. Consequently, supplementary simulations have been carried out varying the entity of the excavation in order to observe how the storage volume affects the hydrological performances. The hydrological efficiency of these RWHT was compared to a plain configuration that represents the case in which no agricultural techniques are implemented.

Identification codes are used to label each configuration, as shown in Table 3.10.

Table 3.10 Characteristics and identification codes for the different RWHT configurations analysed.

| Identification code | Excavation depth [cm] | Configuration |
|---|---|---|
| PL | 0 | Plain |
| $HM_{30}$ | 30 | |
| $HM_{20}$ | 20 | Half-moon |
| $HM_{10}$ | 10 | |
| $PP_{20}$ | 20 | Planting pits |
| $PP_{10}$ | 10 | |

### *Hydrological data*

The meteorological input used to test the rainfall-runoff model is the extreme rainfall hyetograph previously computed and used as input for the HEC-RAS model. This hyetograph is characterized by a rain depth of 40 mm with a peak intensity of 80 mm/h. The shape of the hyetograph shows that almost 95% of the entire precipitation falls with high intensity in an interval shorter that one hour, and the rest drops as a low-intensity tail (Figure 3.18). To enhance the correct representation of the phenomena, the hyetograph has been generated with a high temporal resolution of 1 minute.



(a)
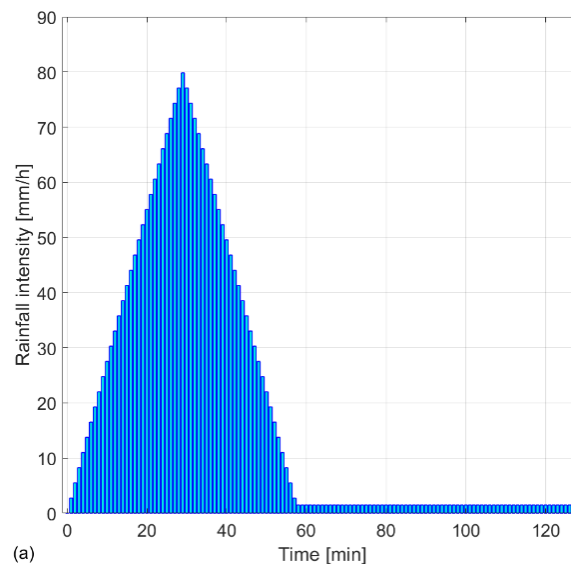
Figure 3.18 Hydrological input for the rainfall/runoff model: the extreme rainfall hyetograph.

*Input parameters*

The rural sub-Saharan regions present a vast range of land cover types that characterize the hydrological properties. These properties are essential for analysing the hydrological processes, meaning the fluxes exchanges at the transition zone between the atmosphere and the sub-surface. Since the methodology examined in this study was not calibrated on a set of physical properties describing a specific area, the intention was to test the numerical model on a vast range of cases characterizing the Sahelian farm fields. In order to achieve the goal, a series of Monte Carlo analyses were carried out where several simulations were run using different sets of model parameters. In a Monte Carlo analysis, a probabilistically-based sampling method is used to design the analysis inputs [174]. Among many sampling procedures, the Latin Hypercube Sampling (LHS) method has been used to generate the sets of parameters [175]. LHS is commonly used to decrease the computational demanding when running Monte Carlo simulations. Many authors have revealed that LHS can significantly cut down on processing time versus a standard Monte Carlo random sampling [176].

For each analysis, 300 simulations were performed with as many parameter sets generated within defined ranges. The LHS method creates a uniformly distributed set of parameters into the selected range.

Each set is composed of six parameters that we have identified as the most influential on model performances. The first one is the roughness expressed by the Manning's coefficient and the others are parameters of the infiltration model. The parameter ranges were obtained from previous studies which investigated hydrological processes in those areas and guidelines. They are summarized in Table 3.11.

Table 3.11 Parameter ranges used in the Monte Carlo analysis.

| Parameter | Sampling range | Unit | Source |
|---|---|---|---|
| Manning coefficient ($n$) | [0.02-0.7] | sm$^{-1/3}$ | [177–179] |
| Suction ($\Psi$) | [110-290] | mm | [173] |
| Total porosity ($\eta$) | [0.30-0.48] | - | [85,173] |
| Initial saturation ($I_s$) | [0.07-0.1] | - | [180] |
| Hydraulic conductivity ($k_{s,surface}$) ($k_{s,hole}$) | [0.5-3] [1] [10-40] [2] | mm/h | [173,177,178,180,181] |

[1] set for crusted surface

[2] set for tilled surface

In order to take into account the effect of crusting on the infiltration process, two different ranges of hydraulic conductivity have been adopted. Lower values

of $k_s$ (named $k_{s,surface}$ ) were set to those areas characterized by crusted soil and higher values (named $k_{s,hole}$) characterize the subcrust soil where the crust is broken during the tillage. The study of Esteves et al. [182] reported the importance of differentiating between abovementioned soil characteristics to enhance the capability of a hydrological model to properly simulate the process of runoff formation.

### *Hydrological efficiency estimation*

The impact of the analysed configurations in the hydrological processes related to rainfall-runoff transformation was evaluated in terms of three different efficiency measures:

- Flow peak reduction: calculated as the reduction on the maximum flow rate that flows out of the domain with and without the implementation of RHWT ($Q.max_{RWHT}$ and $Q.max_{PL}$ respectively)

$$\phi_Q = \left(1 - {Q.max_{RWHT}}/{Q.max_{PL}}\right) \cdot 100 \qquad (3.19)$$

- Volume reduction: calculated as the reduction on the cumulated volume of water that flows out of the domain with and without the implementation of RWHT ($Vol.out_{RWHT}$ and $Vol.out_{PL}$ respectively)

$$\phi_V = \left(1 - {Vol.out_{RWHT}}/{Vol.out_{PL}}\right) \cdot 100 \qquad (3.20)$$

- Infiltration increase: calculated as the increase on the cumulated volume of water infiltrated in the sub-surface with and without the implementation of RWHT ($I_{RWHT}$ and $I_{PL}$ respectively)

$$\phi_I = \left({I_{RWHT}}/{I_{PL}} - 1\right) \cdot 100 \qquad (3.21)$$

### 3.4.3 Results

*Hydrological behaviour*

The hydrological response to the simulated meteorological event was analysed in terms of runoff and infiltration generated by each RWHT configuration. The Monte Carlo simulations performed with the fully distributed hydrological model provided a wide range of outcomes. The computed hydrographs at the outlet of the considered Sahelian farming plot are displayed in Figure 3.19. In addition to all the Monte Carlo results, the average and the 25–75% percentiles were added to each graph.

Observing the computed hydrographs one by one, it is important focusing on the shape of them, meaning how the discharge evolves over time. We can identify the configurations that produce a regular hydrograph, characterized by an upward and downward phase, and an irregular hydrograph. The irregular hydrographs show two distinct branches. At the beginning of the event, the discharge increases very slowly because the ponds are still being filled with water. Then, once they get filled, there is a sharp increase in the hydrographs until the peak. This behaviour showing two branches and a delayed peak has been described in the section "*Conceptual model: RWHT performance evaluation*" of the methodology 1.

The PL, $HM_{30}$ and $HM_{20}$ configurations produce a regular hydrograph even if with a wide difference in magnitude. The half-moons are big enough to collect the runoff without getting filled and just the rainfall that is not intercepted by them contributes to the outlet hydrograph. On the other hand, both the PP configurations produce irregular hyetographs. At the beginning of the rainfall, the small runoff is efficiently collected into the ponds since PP are homogenously spread over the plot. Once they get filled, the hydrographs quickly rise, reaching peak discharges in between the PL and the $HM_{30}$ configurations.

A result at the midpoint, between the previous cases, is presented by the $HM_{10}$ configuration in which it is possible observing both hydrographs kinds. For most of the accomplished simulations, the $HM_{10}$ displays regular hydrographs as well as the deeper half-moons. Only a few sets of parameters lead to an irregular hydrograph, meaning that the $HM_{10}$ configuration is close to being overfilled by the extreme rainfall and its performance is solidly related to the input parameters. Especially, only one simulation leads to the failure of the retention capacity (see Figure 3.19 (d)).
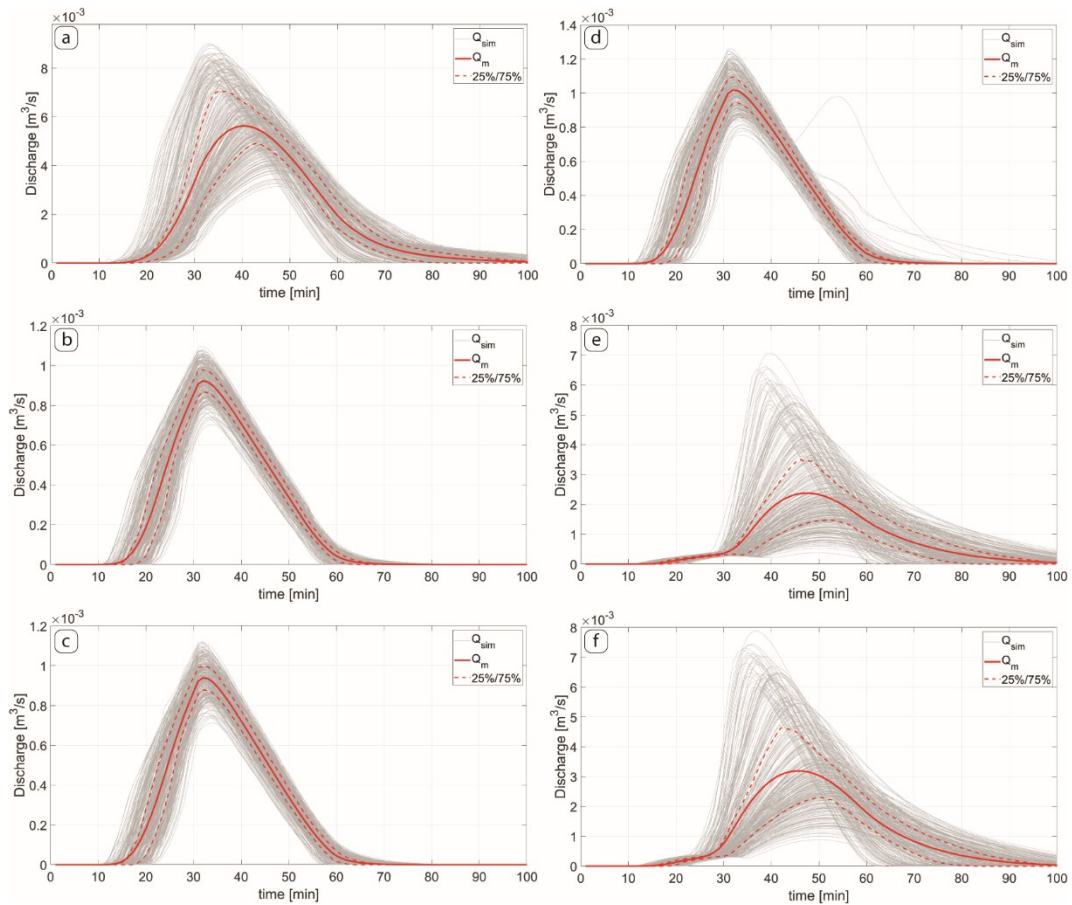
Figure 3.19 Hydrographs computed for the Monte Carlo simulations in the PL (a), $HM_{30}$ (b), $HM_{20}$ (c), $HM_{10}$ (d), $PP_{20}$ (e), and $PP_{10}$ (f) configurations. Red solid line represents the mean discharge. Red dashed lines represent the first and third quartile of the distribution. Light grey solid lines are the outcomes of each simulation.

The amplitude of the results range is directly correlated to the sensitivity of model output to the input parameters. For the PL and PP configurations, the Monte Carlo simulations produce hydrographs significantly different from each other, meaning that the hydraulic behaviour of this type of configurations is strongly affected by the input parameters (the surface roughness and soil characteristics). Conversely, the HM configurations are less affected by the input parameters, being the shape and magnitude of the hydrograph mostly determined by the geometry.

Observing the infiltration trends in Figure 3.20, each configuration presents a different infiltration capacity. For the plain PL configuration, given the absence of harvesting structures, the infiltration trend equally follows the rainfall trend. Thus, the infiltration finishes with the end of the rainfall. On average, PL leads to a total infiltration slightly lower than 50% of the total precipitation. For the half-moons, there is, on average, a return to the dry condition (when the infiltration curve becomes horizontal) at 300 minutes, whereas the planting pits present a positive

infiltration trend up to 400 minutes. The infiltration trends for HM end and attest a total infiltration close to the 95% of the rainfall amount. Instead, PP show an infiltration capacity of 78% and 70% of the total precipitation for $PP_{20}$ and $PP_{10}$ respectively.
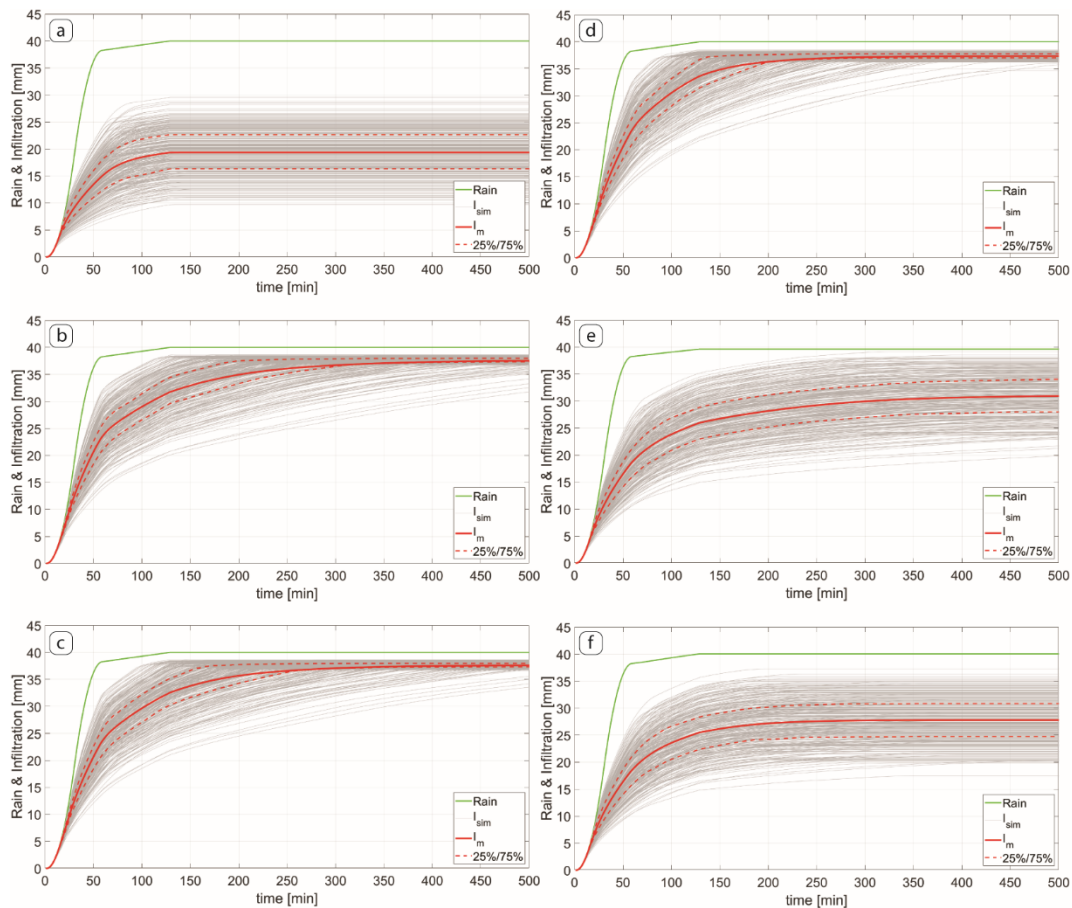


Figure 3.20 Infiltration trend computed for the Monte Carlo simulations in the PL (a), $HM_{30}$ (b), $HM_{20}$ (c), $HM_{10}$ (d), $PP_{20}$ (e), and $PP_{10}$ (f) configurations. Red solid line represents the mean infiltration. Red dashed lines represent the first and third quartile of the distribution. Light grey solid lines are the outcomes of each simulation.

### *Hydrological Efficiency Assessment*

The three measurements selected to evaluate the hydrological efficiency of each RWHT represent the degree of improvement that the farmers could obtain whether these techniques are adopted. The comparison was made simulation by simulation in order to compare couples of configurations with the same input parameters.

The effectiveness in reducing the maximum discharge flowing out of the domain $\phi_Q$ has been found considerably different between the analysed

configurations (Figure 3.21). The HM configurations are averagely 23% and 40% more efficient the $PP_{20}$ and $PP_{10}$, respectively. Despite among the different designs of the half-moons the $\phi_Q$ is almost constant, the shallower planting pits show an efficiency 16% lower than the deeper one. For example, the boxplot of $MH_{30}$ illustrates an average $\phi_Q$ of 84% with a maximum of 89% and a minimum of 77%, while for $PP_{20}$ the average is set at 60% and the maximum and minimum are 88% and 21%, respectively. Moreover, from the results shown in Figure 3.21, it is clear how the input parameters strongly influence the PP results, while they slightly impact the efficiency of the HM configurations.
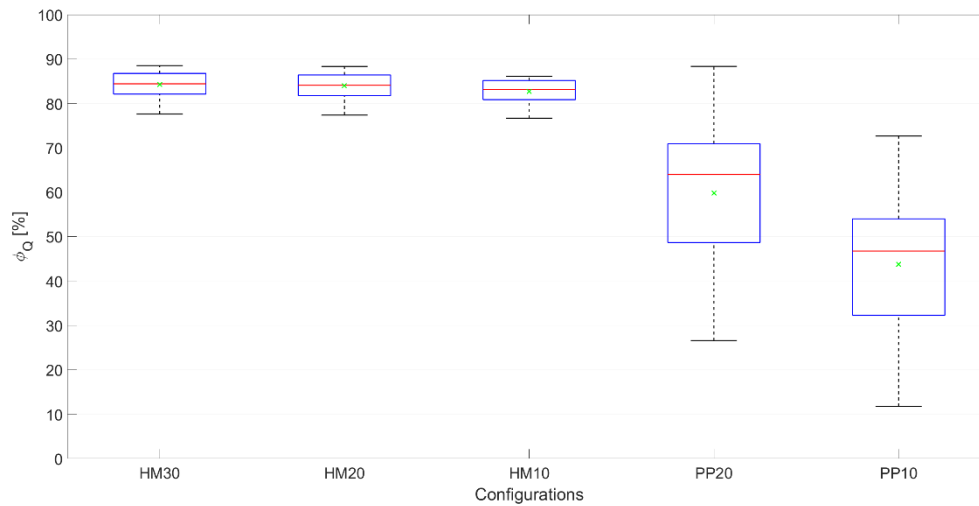


Figure 3.21 Boxplot of the flow peak reduction efficiency. In each box, the upper and lower edges indicate the first and third quartile, respectively, the red central line is the median and the green x symbol is the mean. The whiskers length was set equal to the interquartile distance. Outliers have been hidden.

Considering outflow reduction (Figure 3.22), the values of $\phi_V$ are similar to the $\phi_Q$. The major difference lies in the size of the boxplots. The smaller sizes of the $\phi_V$ boxes indicate the smaller variability of $Vol.out$ among the different simulations compared to the $\phi_Q$. On average, the efficiency of the HM configurations is more than 30% higher than the PP configurations. For both RWHT, the configurations with the bigger excavation have a higher performance than the smaller ones. For half-moons, the efficiency shows a very slight variation between the three configurations, from 87% to 85% for the deeper hole and the shallower hole, respectively. Instead, in the PP configurations, the depth of the ponds has a higher impact on the water volume retained within the plot. Indeed, halving the depth of the excavation leads to a 15% drop in $\phi_V$.
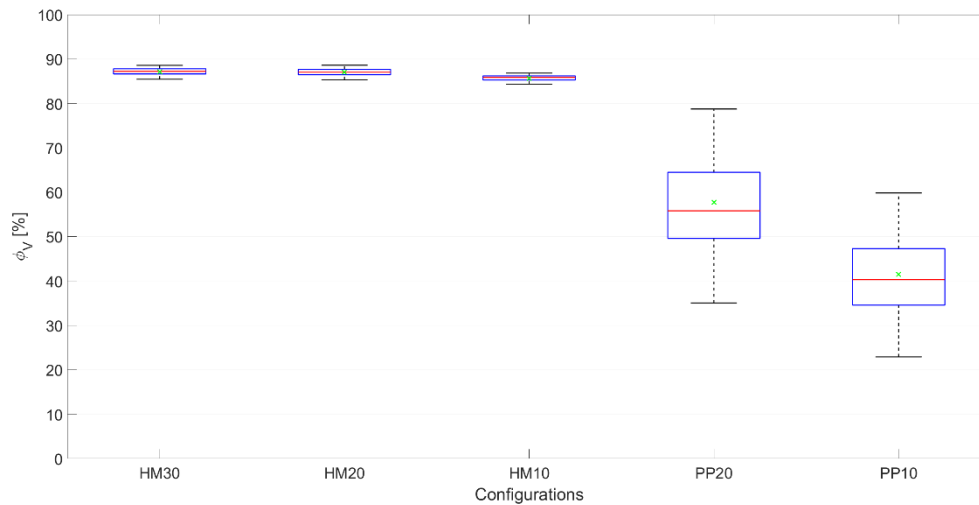
Figure 3.22 Boxplot of the volume reduction efficiency. In each box, the upper and lower edges indicate the first and third quartile, respectively, the red central line is the median and the green x symbol is the mean. The whiskers length was set equal to the interquartile distance. Outliers have been hidden.

Commonly, the Sahelian storms drop down a consistent amount of rain in a few minutes. Thus, the process of water retention starts with catching the rainfall and the runoff inside the micro-basins and continues with the infiltration of this amount of water into the subsurface. Thus, the infiltration efficiency $\phi_I$ increases over time until the surface returns dry. For this reason, it was evaluated for different times lags after the extreme event occurs, labelling the results with the subscript of the related time lag. The $\phi_I$ calculated are displayed in Figure 3.23.
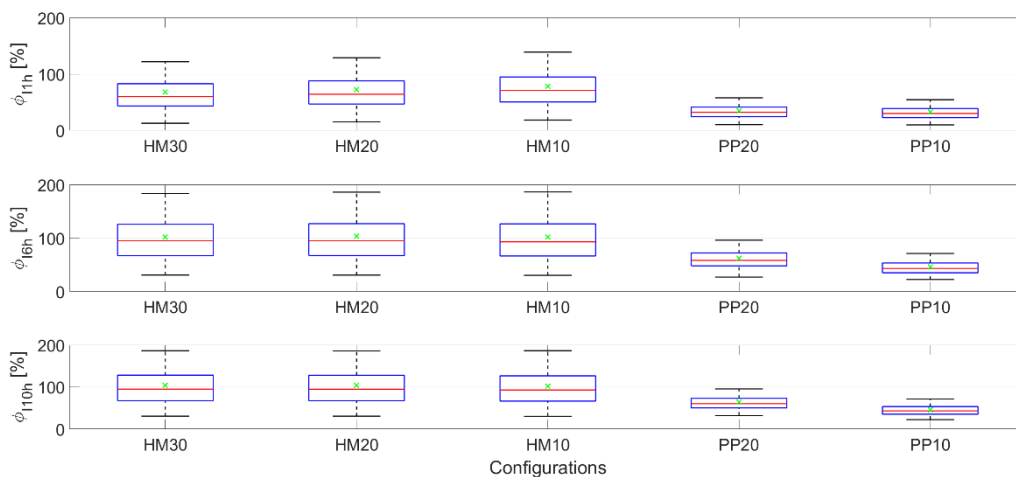


Figure 3.23 Boxplot of the infiltration increase efficiency. In each box, the upper and lower edges indicate the first and third quartile, respectively, the red central line is the median and the green x symbol is the mean. The whiskers length was set equal to the interquartile distance. Outliers have been hidden.

HM configurations have a storage volume large enough to harvest all the water that falls during the simulated extreme event in almost all simulations, i.e., independently of the input parameters. This means that each half-moon has the same volume of water that will infiltrate into the soil, although the infiltration rate will vary depending on the soil parameters. Observing the differences between the deepest and shallowest HM configurations ($HM_{30}$ and $HM_{10}$, respectively), the variation of $\phi_I$ overtime is marginally noticeable. At the end of the event ($\phi_{I1h}$), the $HM_{10}$ shows an efficiency 10% higher than $HM_{30}$ (and 6% higher than $HM_{20}$) meaning that more water has been infiltrated during the precipitation. At such early stages, the infiltration in the shallower HM is higher due to the conformation of the excavation, that presents a rather wider pond bottom than in the $HM_{30}$. Thus, even though the water depth is greater in $HM_{30}$, i.e. higher hydraulic pressure that pushes the water towards the subsurface, the wider surface of $HM_{10}$ bottom on which the hydraulic head insists leads to a higher infiltration rate.

After 6 h ($\phi_{I6h}$) the two efficiencies are equal, while later on the efficiency of $HM_{30}$ becomes higher than that of $HM_{10}$. At the end of the infiltration process, the values of $\phi_{I10h}$ are equal for $HM_{30}$ and $HM_{20}$ while $HM_{10}$ displays a value 2% smaller. The slight discrepancy is related to those few simulations that have been overfilled (see Figure 3.19(d)). This highlights that, for this RWHT, the infiltration process is more affected by the geometry rather than by differences in water depth inside the hole.

For the PP technique, the gap between the two configurations increases over time. Since both configurations are overfilled during the event, the $PP_{20}$ has a higher volume of water retained, and it produces a greater infiltration. Thus, the efficiency of $PP_{20}$ is only 4% higher than $PP_{10}$ at a time lag of 1 h ($\phi_{I1h}$), while it reaches a difference of 28% at 10 h ($\phi_{I10h}$).

Conversely to the previous efficiency measures considered, the variability of $\phi_I$ is larger for HM configurations than PP configurations. This is due to the similarity of the infiltration trends between PL and PP rather than HM.

Focusing on the average values of $\phi_{I10h}$, all HM configurations are higher than 100% meaning that they lead considerably improve the hydrological efficiency of the farmland doubling the infiltration capacity. Instead, PP configurations produce a total improvement of 64% and 46% using planting pits 20cm and 10cm deep, respectively.

### *Influence of parameters*

The previous results showed that the model parameters play a crucial role in the assessment of the hydrological performances of RWHT. Thus, the influence of each input parameter on model output was also investigated. The correlation between the runoff coefficients evaluated as the ratio between the volume of water flowing out of the domain and the cumulated rainfall, and the input parameters were investigated. All correlation coefficients are summarized in Table 3.12.

Knowing that the degree of correlation is as stronger as the value of the coefficient is closer to $\pm 1$, the results show that the hydraulic conductivity outside of the holes ($k_{s,surface}$) plays the main role in the formation of the outflow discharge. This is explained by the fact that it is the parameter that mostly controls the amount of water that infiltrates and does not reach the field outlet.

Table 3.12 Spearman's correlation coefficients ($\rho_s$) between the runoff coefficient and input parameters for each configuration.

| | PL | HM$_{30}$ | HM$_{20}$ | HM$_{10}$ | PP$_{20}$ | PP$_{10}$ |
|---|---|---|---|---|---|---|
| Manning coefficient ($n$) | $-0.34$ | $-0.13$ | $-0.09$ | $-0.30$ | $-0.41$ | $-0.45$ |
| Suction ($\Psi$) | $-0.32$ | $-0.33$ | $-0.33$ | $-0.33$ | $-0.37$ | $-0.37$ |
| Total porosity ($\eta$) | $-0.20$ | $-0.21$ | $-0.21$ | $-0.20$ | $-0.20$ | $-0.20$ |
| Initial saturation ($I_s$) | $0.01$ | $-0.02$ | $-0.02$ | $0.02$ | $0.02$ | $0.02$ |
| Hydraulic ($k_{s,surface}$) | $-0.82$ | $-0.86$ | $-0.86$ | $-0.83$ | $-0.73$ | $-0.71$ |
| conductivity ($k_{s,hole}$) | - | $0.08$ | $0.09$ | $0.07$ | $-0.16$ | $-0.15$ |

The differences between the HM and PP configurations show that the $k_{s,surface}$ affects more the half-moons than planting pits configurations, while the influence of the roughness is more marked on PP than HM (Figure 3.24). The explanation lays in the behaviour of PP which get overfilled during the event. When the PP retention fails, more water flows on the surface between the ponds and this makes the correlation with $k_{s,surface}$ weaker and the correlation with the roughness coefficient stronger. This is also confirmed by the increase of $\rho_s$ value related to $n$ in the HM$_{10}$ configuration. The specular behaviour might be seen in the correlation with the total volume of water infiltrated during the event. Thus, with all positive correlations. The weak correlation with $k_{s,hole}$ might be linked with the fact that the entire runoff harvested by the RWHT is however infiltrated independently by the entity of the hydraulic conductivity. This is even more marked for HM where $\rho_s$ values are almost zero.
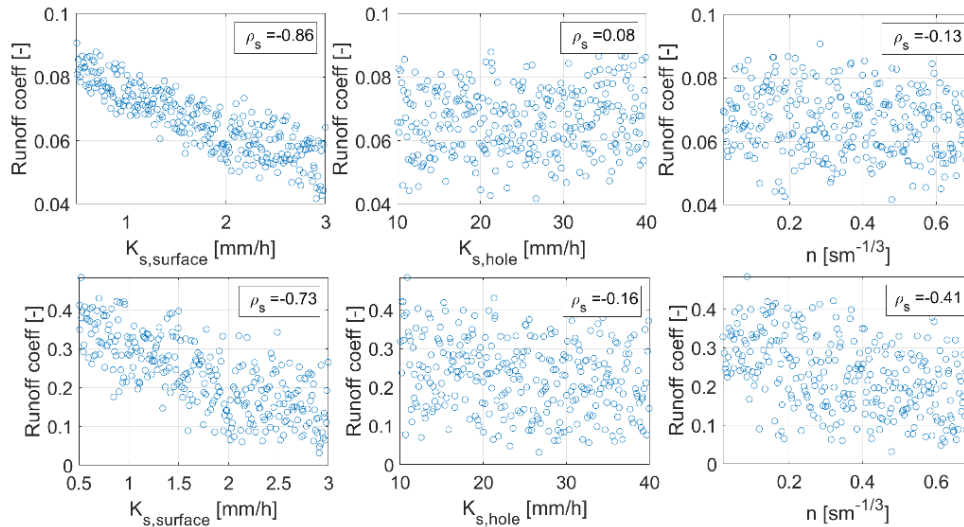
Figure 3.24 Correlation between runoff coefficient and input parameters for $HM_{30}$ (first row) and $PP_{20}$ (second row). $\rho_s$ is the Spearman's correlation coefficient between couple of datasets.

The results in Table 3.12 underline how the model is more sensitive to three parameters: $k_{s,surface}$, $n$ and $\Psi$. The role played by these parameters in alternating the hydrograph at the outlet has been evaluated plotted the maximum discharge in a parameter space Figure 3.25. The figure shows that the $Q.max$ is insensitive to the suction, since all red dots are parallel to the $\Psi$ axis. Focusing on the influence of the other two parameters (Figure 3.25, third column), all configurations delineate a similar trend in which as the value of the two parameters increases, the amount of $Q.max$ decreases.

The different distribution of dots for the two RWHT confirms that the HM performance is more conditioned by the $k_{s,surface}$, whereas PP is roughly insensitive to $k_{s,surface}$ and is more influenced by the roughness.
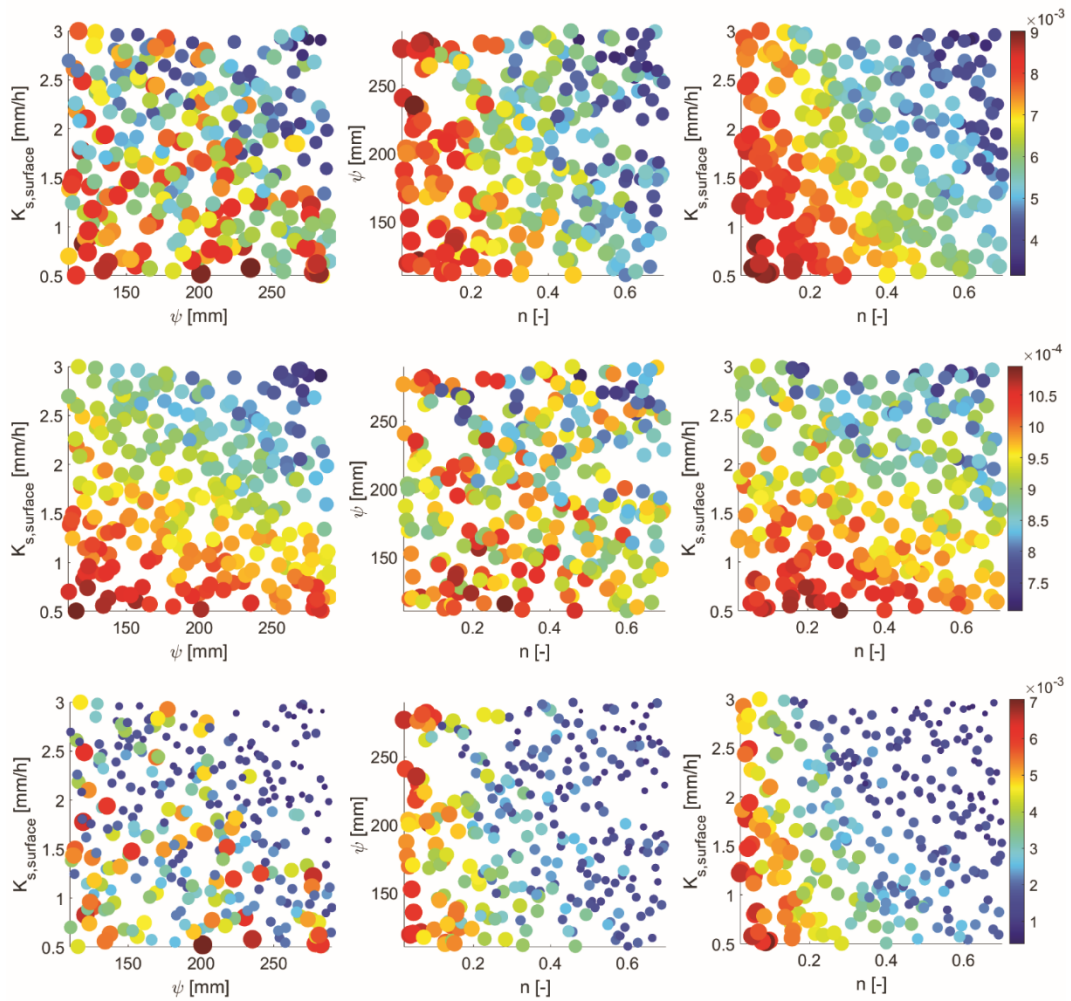
Figure 3.25 Simulations plotted in a parameter space. The first row is related to the PL configuration, the second to the HM$_{30}$ configuration and the third to the PP$_{20}$ configuration. In all plots, each dot represents a simulation, while the size and colour of the dot are set proportional to the flow peak ($Q.max$).

## 3.5   Comparing methodologies

The previous sections have reported the description of the two methodologies implemented and tested to achieve the assessment of the functioning and performances of some indigenous rainwater harvesting techniques, primarily utilized in arid and semi-arid contexts. In each method, a different software has been used for implementing rainfall-runoff models. Comparing the common results obtained from them, it is possible to analyse the benefits and constraints induced by a hydrological modelling or a pure hydraulic modelling.

The two common performances analysed were the flow peak reduction and the volume reduction for the two configurations, the staggered half-moons with a depth of 30cm and staggered planting pits with a depth of 20 cm, under the extreme rainfall condition. The results for both methodologies are summarized in Table 3.13.

Table 3.13 Flow peak and volume reduction for the two tested methodologies. Nb: for the second method, the values are referred to the average value of the performance measure.

|  |  | Hydraulic model (Methodology 1) | Hydrological model (Methodology 2) |
|---|---|---|---|
| Flow peak reduction | HM | 77 | 84 |
| [%] | PP | 23 | 60 |
| Volume reduction | HM | 70 | 87 |
| [%] | PP | 30 | 58 |

Firstly, observing the flow peak reduction, a rather slight difference of 7% can be observed for HM configuration. This is because, since the ponds are big enough to collect the entire runoff, only the terminal part of the domain generates the outflowing runoff and the additional computation of the infiltration slightly affect the hydrograph at the outlet. This explanation is also supported by the smaller values of $\phi_Q$ displayed in Figure 3.21, where the lower end of the whisker marks the value of 77%. According to Figure 3.25, the higher values of $Q.max$, i.e. the lower values of $\phi_Q$, occurs for small values of the hydraulic conductivity. This condition is similar to the waterproofness condition that characterizes the HEC-RAS model. Indeed, the two models lead to a similar result. On the contrary, a significant difference, up to 37%, can be observed for PP configuration. In this case, in which ponds are overfilled during the rainfall, the whole domain is covered by the water overflowing from the pits and the computation of the infiltration heavily weighs on the outcomes.

Analogous considerations can be delineated for the runoff reduction at the outlet. Accounting for the infiltration leads to an increase of 17% and 28% for the HM and PP configurations, respectively. This means that even though the main role is played by the geometrical features of the RWHT, neglecting the hydrological components of the water balance leads to a consistent underestimation.

Besides the simulation outcomes of the two methodologies, some interesting considerations could be elaborated regarding the spatial discretization utilized by the two selected software. The RWHT analysed are micro-catchment practices, meaning that the morphological alterations practised during their realization are confined to a few metres or even centimetres. To take into account such small geometries is often a tricky issue for hydraulic modelling. This issue is partially overcome in HEC-RAS thanks to the sub-grid bathymetry approach, which allow using larger computational cells without losing the geometrical information. A low number of cells lets to simulate larger domains without increase the computational load. Instead, Iber needs an unstructured mesh to solve the equation systems. An unstructured grid strictly follows the shapes of the surface analysed and, therefore, each cell will necessarily be smaller than the minimum size of the geometry. This implicates the design of an unstructured mesh with a high number of small computational cells and consequently a high computational load.

## 3.6   Discussion

Over history, farmers have developed many types of RWHT to address many necessities. The main scope that drives thousands of drylands inhabitants in building RWHT is to collect as much water as possible during the rainy season minimizing variability in water availability to prevent deficits during dry spells [183]. The application of RWHT induces a series of positive impacts that lead to an improvement of the whole dryland ecosystems [65]. Indeed, in recent years, these techniques are used not only for crop production but also as support to agrosilvopastoral systems to promote the cover rehabilitation of shrubs and trees.

In addition to these important issues, impellent is the necessity to find solutions to cope with the harsh consequences of climate changes. On the wave of research, the focus flew on the exploration of the use of RWHT as a smart and sustainable solution to mitigate flood hazard. The investigation led to the implementation of two methodologies detailed in the previous sections.

The first methodology exploits the numerical modelling to understand the hydraulic performances of the most used RWHT in the Sahel. Results show how the harvesting capacity of some RWHT may lead to a remarkable reduction of the runoff, both at the scale of the agricultural field and at the basin scale. From the different RWHT and geometrical configurations examined, it was found that in all cases the staggered configuration has superior performance than the aligned configuration. For this reason, independently on the technique, farmers should be inclined to opt for staggered arrangements as good practice. Moreover, S-HM has demonstrated to have has the best performance among the different precipitations. The capacity of runoff reduction is also comparable with other works that studied this issue directly with on-site measurements [78]. The good performance of planting pit and Vallerani trenches, for heavy rainfall, indicates that these techniques should be preferably used in arid areas (northern border of the Sahelian strip) where the lower precipitation per event does not exceed their storage capacity. In semi-arid regions characterized by more intense precipitation, half-moon or hand-dug trenches are preferable rather than micro-basins with very small size.

Collecting and reducing the overland flow, RWHT provide a notable reduction of the runoff coefficient of treated areas. This parameter will identify the hydrological response to rainstorms of the improved agricultural field. The wider use of these techniques could stop the uninterrupted increase of runoff coefficient that is affecting Sahelian watersheds since the 1960s [14]. This hydrological phenomenon was designated as "Sahelian Paradox" and many studies have tried to explain which the natural or anthropological drivers are. First of all, the long dry spell called "the great drought" (1970-1990) led to a heavy land use/land cover modification characterized by vegetation dying with consequent formation of bare soil exposed to crusting and erosion [31,36]. This drastically changed the surface hydrological features reducing the water holding capacity of the soil with a direct increase of the $R_c$. Therefore, the development of policies aimed to spread the use of RWHT could be the solution to reverse the hazardous positive trend of $R_c$.

An additional finding was the positive correlation that exists between RWHT design (storage volume) and hydraulic performance, mainly for extreme events. Knowing that, it is fundamental keeping constant the maintenance of each micro-basin over time, planning the restoration works at the beginning of each rainy season. The displacement of topsoil caused by sheet erosion (induced by raindrops or sheet flow) and consequent sedimentation might reduce the storage capacity

during the monsoon season. For this reason, the RWHT design should avoid excessive spacing between structures.

The major weakness identified in the use of a hydraulic model is surely the neglection of the hydrological balance components. To overcome such constraint, the second methodology exploited the use of a numerical model able to compute the losses due to the infiltration processes. The coupled use of Iber and Monte Carlo simulations provide a deep analysis of the functioning of indigenous RWHT under a wide range of possible scenarios that might be faced in Sahelian rural areas. According to the strong correlation between design and performances found from the application of the first methodology, different designs were also examined.

The investigation of multiple cases allowed to discover that the hydrological behaviour of planting pits is strongly affected by the input parameters, given the wide range of variation of the numerical results. Hence, the project should be preceded by a campaign of on-site surveys and sampling to accurately evaluate the physical parameters characterizing the site. On the contrary, for HM, the small sensitivity of model output to the soil parameters means that the hydrological efficiency is mostly controlled by the geometry. Thus, during the planning phase, the design is more important than the characterization of the site. In fact, from $\phi_I$ results, we can assert that (under the same hydrological conditions as the simulated ones) it is preferable to shape RWHT with shallower and wider holes instead of deeper and smaller holes. During the planning phase, once the project rain has been detected, the critical volume that avoids the overfilling of RWHT should be calculated and used to define the shape of the optimal agricultural practice. Furthermore, the design of the volume should consider the type of purpose for which RWHT are used. For example, RWHT for food production are often filled with organic manure or compost to enhance the nutrient supply rising the soil fertility [58,61,184,185] but in doing so the storage capacity of the single structure drastically drops down, reducing the efficiency in terms of runoff mitigation.

Sahelian countries are among the poorest in the world and, often, farmers have no access to tillage machines and all phases of the cultivation are handmade. Therefore, the entity of manual labour is strongly correlated to the RWHT design. The results showed in Figure 3.21, Figure 3.22 and Figure 3.23 show that it is worth excavating deeper RWHT only if there is a relevant efficiency improvement. Especially for HM, it would be preferable to choose $HM_{10}$ instead of deeper ponds, saving in that way many hours of manual labour, since the volume of earth to dig is almost one-third of $HM_{30}$. On the contrary, making the

effort of digging deeper planting pits leads to consistent improvements, harvesting more water into the farming field and promoting soil water storage recharge.

Observing the relation between parameters and the runoff coefficient, the strong correlation between the $R_c$ and $k_{s,surface}$ means that is also important to treat the surface between ponds in order to reduce the overland flow and to keep the water inside the farm field.

Zooming out at a larger scale, all the findings convey that building a large number of RWHT will increase the water holding capacity of the whole basin reducing the runoff and preventing potentially dangerous floods downstream.

Besides, decreasing runoff triggers a reduction of sediment transport capacity of the overland flow preventing topsoil erosion. Surface runoff running on bare crusted soil has a high erosive potential, also in flatland, and often digs rills and gullies. The ongoing propagation of these gullies is developing a vast drainage network visible, in various zones, also from satellites. The impoverishment of vegetative coverage during the great drought strongly pushed the propagation of this phenomenon [186–188]. Thus, RWHT may also accomplish the task of anti-erosion action against flash floods.


## 3.7    Concluding remarks

Considering the long series of catastrophic floods that are sub-Saharan countries, more effort is requested to develop effective strategies aimed to reduce the flood hazard. Climate changes and environmental degradation have been identified as the drivers that are causing the exacerbating of flooding events. Therefore, sustainable land management aimed at the use of climate-smart agriculture practices would be a valid solution to face these problems.

In this chapter, we explored the applicability of RWHT as a reliable strategy for flood prevention and mitigation. Numerical models were set out to investigate the capability of these techniques to reduce the runoff generated by severe rainstorms and improve the hydrological functioning of farmlands.

The two methodologies presented highlighted some important aspects that should guide the project phases of these techniques. Our findings suggest that RWHT always enhance the hydrological efficiency of agricultural fields, but the level of efficiency is strongly related to their design.

To be more specific, whatever technique is chosen, the staggered arrangement gives always better performance than an aligned layout. Among the tested RWHT, staggered half-moons were found to be the most efficient.

Identified the spatial configuration, the best design should be evaluated based on the meteorological features of the target area. The evaluation of different designs demonstrated that, for equal meteorological forcing, opting for the right design could save up to two-third of manual labour. These energies could be employed to upscale the realization of these practices.

Moreover, looking at the watershed management, treating the land surface with RWHT lead to a remarkable reduction of the runoff coefficient of the whole basin. The sharp correlation found between the runoff coefficient and the soil properties outside of the ponds (pointing out the surface hydraulic conductivity) underlines the importance of not neglecting the treatment of the whole surface. Hence, combining RWHT with other surface treatments, such as soil scarifying, will optimize the hydrological efficiency of the whole system.

The comparison between the two proposed methodologies showed that, despite the short temporal scale of simulations, the neglection of some hydrological processes, i.e. infiltration, could lead to considerable underestimations of RWHT performances. Therefore, future studies cannot disregard the use of a hydrological model for the study of all processes involved in runoff formation and propagation.

# Chapter 4

# Climate-Smart Agriculture as adaptive behaviour against hydrometeorological hazards: Rainwater Harvesting Techniques to mitigate the plant water stress induced by rainwater shortage

*"We never know the worth of water till the well is dry."*

*Thomas Fuller*

# 4.1    Preface

The work described in this chapter has been partially derived from the paper "*Rainwater Harvesting Techniques to Face Water Scarcity in African Drylands: Hydrological Efficiency Assessment*" published in Water [147].

The sub-Saharan climate is experiencing a marked increase in temperature and intensification of extreme weather phenomena. Besides, longer and severe dry spells are compromising the reliability of local agricultural practices. This induces the crop to suffer more and more water stress, inevitably leading to a decline in agricultural productivity [189].

To deal with drought-related threats, farmers have improved their fields with various rainwater harvesting techniques aiming to capture rainfall, increase the water use efficiency, reduce crop water stress, and increase the crop survival expectation. Furthermore, climate projections predict an increase in rainwater availability in Sahelian countries [71]. Despite the rainfall pattern will be characterized by a greater spatial and temporal variability, this type of climate affords vast opportunities for water harvesting practices.

In this chapter, a comprehensive assessment of the ecological benefits induced by RWHT and their performances in minimizing crop water stress is accomplished. To achieve the objectives, a series of ecohydrological analyses are carried out through numerical simulations with Iber [151]. The hydrological processes at the field scale are evaluated computing the entire hydrological balance over the growing season of typical Sahelian crops. In order to account for the crop life cycle into the water balance, a new approach was implemented in the model and tested. The proposed calculation of the evapotranspiration rate intents to provide a fast application method and curtail the number of input parameters required dealing with the data scarcity that often characterize developing countries.

The performances of RWHT are compared to a traditional sowing method, highlighting the remarkable advantages induced by the use of such practices.

The outcomes reveal that intercepting and storing runoff, RWHT increase the water content in the root zone preventing crop failure and maximizing the yield. The right design can bring to zero the crop water stress avoiding the necessity of supplementary irrigation. Furthermore, the results show that adopting RWHT makes it possible to extend the growing season up to 20 days, maximizing the productive period of crops.

The improved infiltration provides a faster recharge of groundwater, which is available early for crop and later represents precious storage for plants with a

deeper root system. From an agronomic perspective, this could improve the water-use efficiency of an intercropping system, simultaneously enhancing the ecological value of the landscape. In terms of water management, this means an increase in green water availability for the benefit of a reduction in blue water consumption (groundwater extracted for irrigation) [190,191]. Upscaling the diffusion of these simple and affordable techniques would represent the first step towards the enactment of adaptation strategies to cope simultaneously with climate changes and food scarcity.

## 4.2 Soil water balance assessment

Iber, besides the accurate resolution of overland flow movement described in section 3.4.1, includes the capability of calculating the entire water balance computing the incoming and outcoming fluxes from the subsurface. The procedural steps followed in the implementation of this methodology are schematized in Figure 4.1. The diagram shows all input data required (specifying among data related to the geometry, the meteorology and model's physical parameters) and the phases followed to achieve the ecohydrological efficiency estimation of the analysed RWHT.
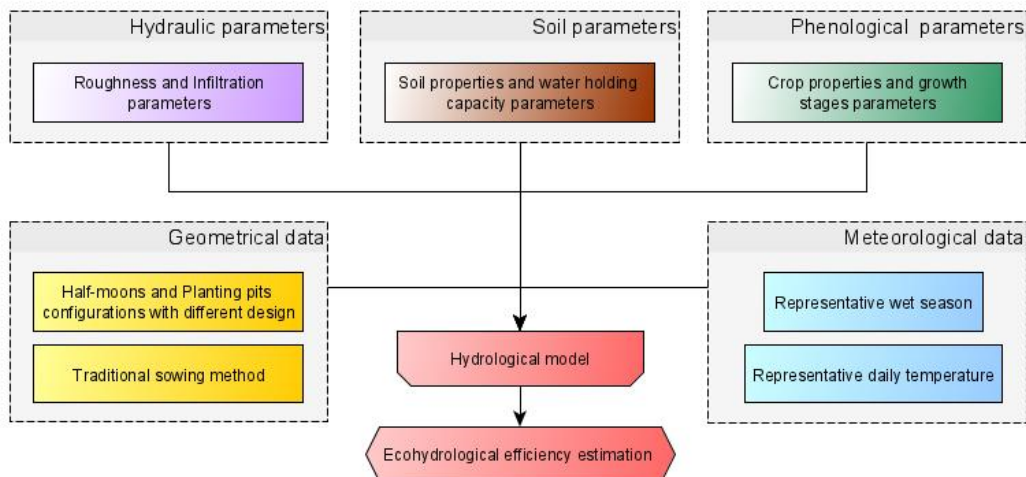


Figure 4.1 Workflow of the methodology. Colouring: geometrical data (yellow), meteorological data (blue), hydraulic parameters (violet), soil parameters (brown), phenological parameters (green), processing and outcomes related to the hydrological model (red).

The Green-Ampt model allows linking the spatio-temporal distribution of surface water with the subsurface flow through the soil water content variation. The mass conservation between the surface and subsurface is based on the 2D

Boussinesq equation-based model for homogeneous unconfined aquifer and can be written as

$$\eta \frac{\partial L}{\partial t} = \frac{\partial}{\partial x}\left(T\frac{\partial H}{\partial x}\right) + \frac{\partial}{\partial y}\left(T\frac{\partial H}{\partial y}\right) + I - DP - ET \qquad (4.1)$$

where $T$ is the horizontal transmissivity, H is the hydraulic head, $DP$ is the deep percolation rate and $ET$ is the evapotranspiration rate.

The left-hand term represents the variation of the soil moisture over time, considering the following relation guaranteed by the infiltration model:

$$\theta = \eta \frac{L}{D_s} \qquad (4.2)$$

where $D_s$ is the considered soil layer extent.

The right-hand side includes all incoming/outcoming fluxes from the sub-surface domain. In every analysis presented in this manuscript, the horizontal transmissivity has been neglected, considering only vertical exchanges.

The water that percolates out of the considered soil layer towards deeper layers is estimated by using the relation proposed by Famiglietti and Wood [192]

$$DP = k_{s,p}\left(\frac{\theta}{\eta}\right)^{(3+2/\lambda)} \qquad (4.3)$$

where $k_{s,p}$ is the saturated hydraulic conductivity of the deep soil, and $\lambda$ is a model parameter, meaning the pore size distribution index based on the soil layer texture. The soil structure might change along with the vertical profile, varying its permeability. Seeing as how the infiltration and percolation processes occur at a different depth, distinct values of hydraulic conductivities have been adopted. The infiltration model's $k_s$ represents the topsoil-saturated hydraulic conductivity that controls the partition of rain between surface runoff and infiltration. On the other hand, the percolation model's $k_{s,p}$ is the saturated hydraulic conductivity that characterizes deep percolation.

The formulation adopted to calculate the evapotranspiration rate has been designed to pursue a twofold intention: a) to be an easy formulation able to carry out an ET assessment dealing with the lack of data that commonly characterize developing countries, b) to take into account the crop influence into the water balance. The evapotranspiration rate depends on many factors such as climate, soil properties, land use/land cover, agricultural practices. Hence, various data and parameters are required to correctly represent the physics of the phenomenon. The

formulation proposed is based on the widely used single-crop coefficient method reported in the FAO Irrigation and Drainage Paper-56 [193]. To overcome the large amount of input data required by the Penman-Monteith equation, the potential evapotranspiration ($ET_p$) is computed through the empirical relation reported in the work of Doorenbos and Pruitt [194]. Thus, the required input is reduced to a single climatic data, usually widely available, the temperature [195]:

$$ET_P = -2 + c\,[\omega\,(0.46\,T_a + 8.13)] \qquad (4.4)$$

where $T_a$ is the air temperature in °C, $\omega$ is the percentage of total daytime hours in which the evapotranspiration occurs (approximately 12h) out of total daytime hours of the year (365x12h) and $c$ is coefficient used for calibration. The actual evapotranspiration ($ET$) is then calculated modulating the $ET_P$ with two coefficients to account for the crop evapotranspiration capabilities under the condition of water availability or scarcity. $ET$ is defined as

$$ET = ET_c\,K_s = ET_P\,K_{c,ij}\,K_s \qquad (4.5)$$

where $ET_c$ represents the crop evapotranspiration, $K_{c,ij}$ is the crop coefficient and $K_s$ is the water stress coefficient depending on the available soil water content.

The crop coefficient $K_{c,ij}$ accounts for the evapotranspiration capability during each growth stage $i$ of specific crop $j$. It varies prevalently with the specific crop characteristics since climate influence is demanded to the $ET_P$. During the growing period, the evapotranspiration of the given crop will vary accordingly to the development of its height and leafage. The growing season can be divided into four different growth stages that can be labelled as: $L_1$ (initial phase), $L_2$ (development stage), $L_3$ (mid-season), $L_4$ (late-season). $L_n$ represents the number of days over which span each stage. Each day of the growing period $i$ will be characterized by a specific value of crop coefficient, see Figure 4.2. Values of $K_{c,i}$ over the development stage and late season have been calculated as the linear variation between $K_{c,ini}$ and $K_{c,mid}$ and between $K_{c,mid}$ and $K_{c,end}$, respectively.
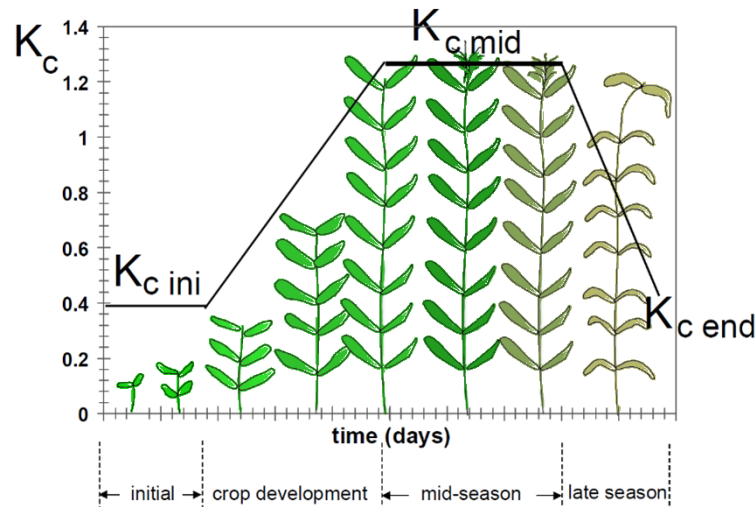
Figure 4.2 Trend of the crop coefficient over the growing season. $K_c$ values range accordingly to the plant development. At the early stage, the value for $K_c$ is small and then increases as the plant grows, reaching the maximum $K_{c,mid}$ when the leafage is completely developed. Towards the late season period, $K_c$ drops down to $K_{c,end}$ due to the plant reaches the senescence. The minimum value of $K_{c,end}$ depends by the crop and the moisture condition at the harvest. Crops that are dried out in the fields before to be harvested, such as cereals, are characterized by a $K_{c,end}$ relatively small (adapted from [193]).

Values for the constants $K_{c,ini}$, $K_{c,mid}$, $K_{c,end}$ and $L_{1,2,3,4}$ have been extracted from table 18 and 11, respectively, of the FAO Irrigation and Drainage Paper-56 [193].

Often the growing season intercepts different environmental season characterized by a different rainfall pattern. This is especially marked in arid and semi-arid areas, where it is possible to identify a strong contrast between the wet and dry season. When no rain or irrigation occurs, the soil becomes dry and a limited amount of water is available for plant root extraction. When the depletion of the soil water storage overcomes a threshold value, the stomata of the leaves begin to close, the crop transpiration capability is reduced, and the crop is said to be water stressed. The threshold value represents the fraction of the total available soil water content ($TAWC$) that the plant can uptake before suffering water stress. This amount represents the readily available water ($RAWC$) and it is expressed as

$$RAWC = p\,TAWC = p\,(\theta_{FC} - \theta_{WP}) \qquad (4.6)$$

where $\theta_{WP}$ and $\theta_{FC}$ are the water content at wilting point and field capacity, respectively, and $p$ is the soil water depletion fraction, which is characteristic for each species. The value of $p$ is assumed to be constant during the growing period and its values are reported in table 22 of the manuscript of Allan et al. [193].

The effect of soil water shortage on crop evapotranspiration is described by the water stress coefficient $K_s$. In terms of water content, $K_s$ can be expressed by the following formulation

$$K_s = \frac{\theta - \theta_{WP}}{(\theta_{FC} - \theta_{WP})(1 - p)} \tag{4.7}$$

The values of $K_s$ vary into the range [0-1] during the growing period. $K_s$ is equal to 1 when the soil water content is higher than the threshold value $\theta_t$, instead, it linearly decreases towards zero when reaching the permanent wilting point (Figure 4.3). The threshold depends on the soil characteristics and type of crop, according to

$$\theta_t = \theta_{FC} - p\,(\theta_{FC} - \theta_{WP}) \tag{4.8}$$
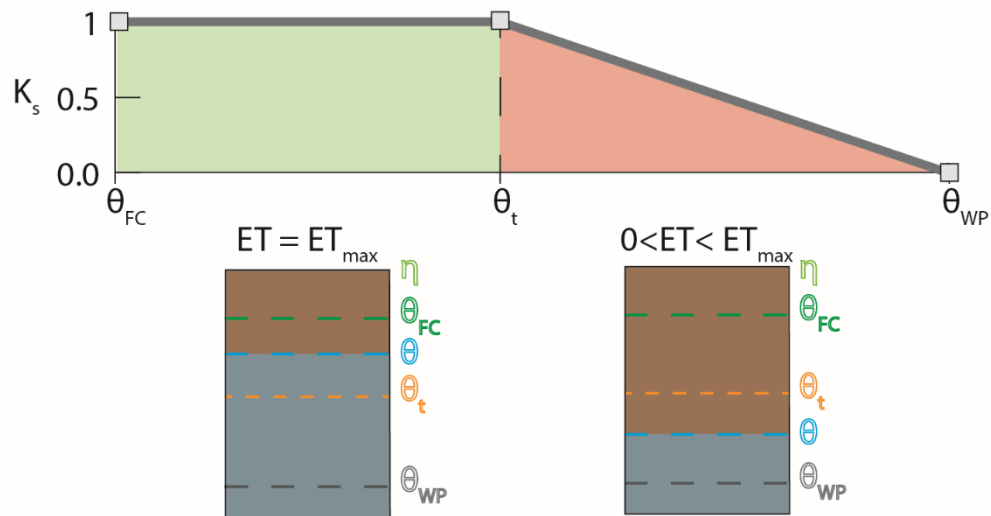


Figure 4.3 Trend of the water stress coefficient according to the soil water content and visualization of the moisture content in a control unit.

**115**

## 4.2.1 Model set up

### *Geometrical data*

The digital representations of the farm fields tested in these ecohydrological analyses are the five RWHT configurations described in section 3.4.2 "*Geometrical data*". The hydrological efficiency of half-moons and planting pits has been compared to a traditional sowing method used by Sahelian farmers. This method consists in breaking the surface crust along rows with rudimentary hand hoes or pickaxes (locally called " iler " or "daba"). Then, seeds are planted in these lines. The rows are commonly tilled 1 meter apart transversely to the slope.

The identification codes used to label each configuration are shown in Table 4.1.

Table 4.1 Characteristic and identification code for the different configurations analysed.

| Identification code | Excavation depth [cm] | Configuration |
|---|---|---|
| TM | 0 | Traditional sowing method |
| $HM_{30}$ | 30 | |
| $HM_{20}$ | 20 | Half-moon |
| $HM_{10}$ | 10 | |
| $PP_{20}$ | 20 | |
| $PP_{10}$ | 10 | Planting pits |

The geometrical schemes and features of the spatial domains are reported in Figure B.3 (see Appendix B).

### *Meteorological data*

Iber is a fully-distributed hydrological model which needs meteorological inputs to compute the intensity of incoming and outgoing hydrological fluxes from the study domain [169]. The spatial and temporal resolution of these inputs depends on the timescale of the simulations. The ecohydrological analyses span over the entire wet season and the hyetograph representative of a rainy season was used. In this kind of approaches, it is common to extrapolate data with a large time scale (daily, weekly, or monthly data). Given the speedy nature of the hydrometeorological events, described in previous sections, it was necessary to consider records with a fine time resolution. For this reason, we selected the Koyria station, installed in the central Sahel, as gauging station from which

extracting rainfall records. The gauging station is equipped with an automatic rain gauge which measures the precipitation amount every 5 minutes and the rainfall time series can be freely downloaded from the AMMA-CATCH database [166]. The representative wet season was identified from the analysis of the twenty-year period 1997-2016 of the rainfall time series. From this temporal range, a representative year has been selected as the one with the highest correlation with the following three statistical parameters calculated for the entire time series:

1.  mean annual rainfall depth: calculated as the average of the yearly precipitation amount. The parameter used to quantify the available resource.
2.  mean maximum rainfall intensity: calculated as the average of the maximum hourly intensity peaks of each year. The parameter used to detect the power of the hydrometeorological events.
3.  mean number of rainy days: calculated as the average of the number of days in which rainfalls occur. The parameter used to investigate the temporal distribution of precipitations.

The daily precipitation over the target wet season is shown in Figure 4.4. As a typical Sahelian rain season, after few isolated precipitations that drop in May/June, the rainfall pattern spans from July to the end of September and the most abundant precipitations fall in August.

According to the equation (4.4), air temperature data are needed to compute potential evapotranspiration and, then, the water balance. The variability of temperature over one characteristic year was calculated as the mean temperature registered in the decade 2004-2014 at the Wankama gauging station (see Figure A.1). This gauging station is located in the heart of the "Superscale observation site" managed by the AMMA-CATCH observatory [166], a few kilometres from the Nigerien capital. It is installed at the same latitude of the Koyria pluviometer and is set about 100 km east of this latter. The gauging system measures and records the air temperature (°C) with a time resolution of 30 min.

The average daily temperature over the year is shown in Figure 4.4. The temperature trend is characterized by two peaks and in opposition to the precipitation trend. A first major peak precedes the rainy season, while a negative trend begins with the onset of rainfall and the second peak occurs at the end of the wet season.
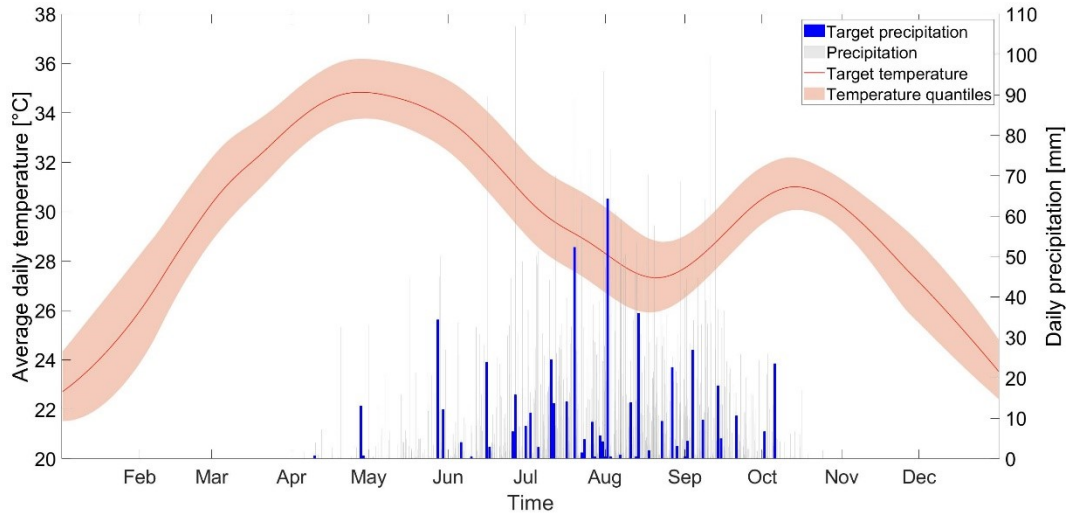
Figure 4.4 Meteorological input: the target temperature (red line) and target precipitation (blue bars). The red area delineates the range of average daily temperature included between the first and the third quartile of the analysed temperature time series. The grey shaded bars represent all the daily precipitation of the analysed rainfall time series.

### *Input parameters*

The computation of the entire water balance requires a large number of parameters to solve the equations systems. They may be clustered in 3 groups:

- Hydraulic parameters: these are the six parameters used to run the hydraulic module, previously explained in section 3.4.1. The set of parameters was chosen based on the results obtained during the Monte Carlo analyses illustrated in the previous chapter. The six parameters were selected from the simulation that generated the hydrograph closest to the mean model behaviour. The set is reported in Table 4.2.

Table 4.2 Hydraulic parameters used in the ecohydrological model.

| Parameter | | Values | Unit |
|---|---|---|---|
| Manning coefficient ($n$) | | 0.34 | $sm^{-1/3}$ |
| Suction ($\Psi$) | | 122.16 | mm |
| Total porosity ($\eta$) | | 0.3 | - |
| Initial saturation ($I_s$) | | 0.5 | - |
| Hydraulic conductivity | ($k_{s,surface}$) | 0.89 | mm/h |
| | ($k_{s,hole}$) | 18.11 | |

- Soil parameters: the parameters characterizing the soil properties are the two parameters needed into the percolation model (i.e. equation (4.3)) and

the two parameters describing the soil water holding capacity. Parameters are listed in Table 4.3.

Table 4.3 Soil parameters used in the ecohydrological analyses [193,195].

| Parameter | Values | Unit |
|---|---|---|
| Hydraulic conductivity $(k_{s,p})$ | 0.5 | mm/h |
| Pore size distribution index | 0.5 | - |
| Field capacity | 0.25 | - |
| Wilting point | 0.15 | - |

- Phenological parameters: we selected three crops at the base of the Sahelian diet: one cereal (millet), one oilseed (sesame), and one root crop (sweet potato). A distinct value of crop coefficient $K_{c,ij}$ is associated with each analysed crop for any stage of the growing period. Phenological parameters are summarized in Table 4.4.

Table 4.4 Phenological parameters used to describe the growth stages of selected crops [193,196].

| Crop | $p$ [-] | Crop coefficient [days] | | | Lengths of growth stages [days] | | | | Growing season | |
|---|---|---|---|---|---|---|---|---|---|---|
| | | $K_{c,j}^{[1]}$ ini | $K_{c,j}^{[1]}$ mid | $K_{c,j}^{[1]}$ end | $L_1$ | $L_2$ | $L_3$ | $L_4$ | length [days] | period |
| Millet | 0.55 | 0.3 | 1 | 0.3 | 15 | 25 | 40 | 25 | 105 | Jul-Oct |
| Sesame | 0.6 | 0.35 | 1.1 | 0.25 | 20 | 30 | 40 | 20 | 110 | Jun-Sep |
| Sweet potato | 0.65 | 0.5 | 1.15 | 0.65 | 15 | 30 | 50 | 30 | 125 | Jun-Oct |

[1] linear variation between extremes.

The rainfall season in the Sahel is always preceded by a long dry period in which no precipitations occur. Thus, the initial conditions were considered strongly arid, meaning a dry surface and subsurface with the soil water content equal to the permanent wilting point [78].

*Ecohydrological efficiency estimation*

The benefits induced by the presence of the analysed RWHT were quantified in terms of:

- Water stress mitigation: calculated as the increase on soil moisture needed to reach the availability threshold with and without the implementation of RHWT ($\theta_{RWHT}$ and $\theta_{TM}$ respectively)

$$\phi_S = \left.(\theta_{RWHT} - \theta_{TM})\middle/(p \cdot \theta_{FC} - \theta_{WP})\right. \cdot 100 \qquad (4.9)$$

- Plant water deficit reduction: mitigation: calculated as the reduction on cumulative plant water deficit with and without the implementation of RHWT ($PWD_{RWHT}$ and $PWD_{TM}$ respectively). The $PWD$ has been calculated as the difference between the crop evapotranspiration $ET_c$ (evapotranspiration under unstressed condition, see equation (4.5)) and the actual evapotranspiration $ET$.

$$PWDR = \left(1 - \left.PWD_{RWHT}\middle/PWD_{TM}\right.\right) \cdot 100 \qquad (4.10)$$

## 4.3 Results

The numerical model was set up whit the purpose of investigating the impact of RWHT on soil water dynamics and their influence on the crop conditions over the growing season. The soil storage recharge, uptake, and the resulting variation in soil moisture were calculated over the entire growing period, from the onset of the rainy season, and therefore the sowing, to the harvesting moment. The feature of the hydrological model of being totally distributed allowed to deeply investigate the dynamics and gradient of soil water content in each point if the domain. Indeed, different studies revealed that the percolation is a strictly vertical process and the increase in soil moisture is essentially limited under the pond [78,197]. To account for this spatial unevenness, the analyses were focused on two scales:

(1) the field scale, in which all outcomes from the hydrological simulations are aggregated over the whole domain. All outcomes coming from the analyses at the field scale are based on millet phenological parameters. At this level, the purpose is to highlight the degree of improvement led by RWHT to the whole domain.

(2) the small scale, in which hydrological processes are examined inside of each basin, where crop seeds are actually sown and grow. Zooming out at the pond level, it is possible to appreciate the real benefit brought by smart agriculture.

## 4.3.1 Hydrological processes at the field scale

The analyses carried out and described in section 3.4 have highlighted how the presence of RWHT markedly increases the fraction of precipitation that infiltrates and fills the soil water storage. The upper graph in Figure 4.5 shows the infiltration outline over the entire wet season. Above all configurations, the $HM_{30}$ leads to the best improvement, with a cumulative infiltration two times greater than TM. However, the differences between the deeper and shallower HM are roughly slight. Indeed, the gap between the deepest and shallowest HM is lower than 10%. On the contrary, both PP configurations do not seem to be effective since the amount of water collected over the season is even smaller than the traditional methods.

In correspondence of each rainfall, the moisture content into the root zone varies according to the amount of water that infiltrates into the ground. The soil moisture dynamics over the wet season is displayed in Figure 4.5 (lower graph).
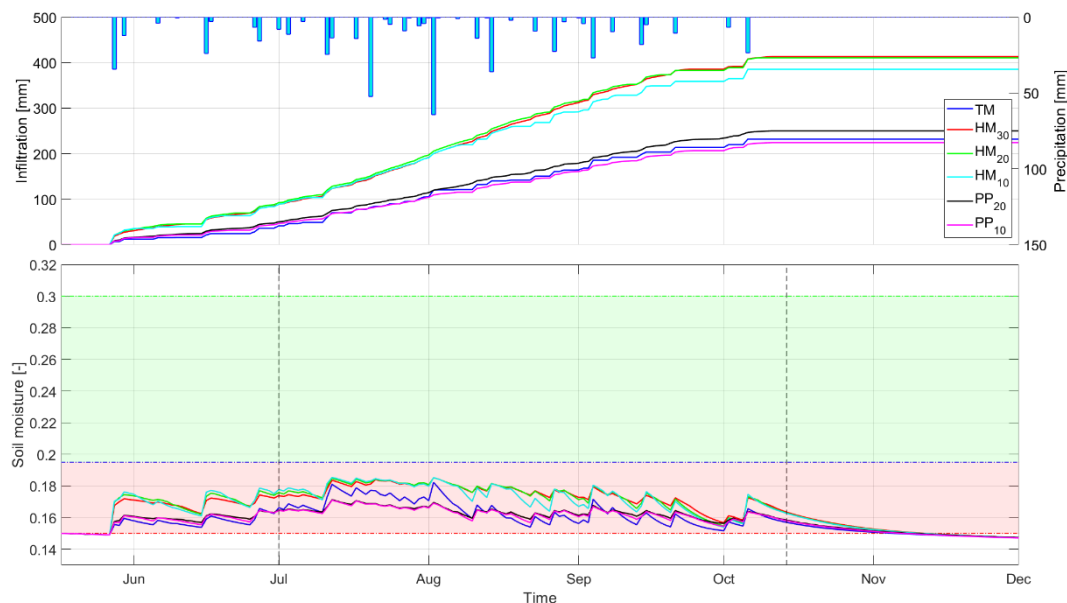


Figure 4.5 Precipitation (blue bars), cumulative infiltration and soil moisture trend (coloured lines) at the field scale over the wet season for millet. The red area represents the level of water content lower than the threshold in which the crop is water stressed. The green area highlights the range in which soil water availability is enough to meet the demand of the crop. The boundary between the two areas corresponds to the threshold of readily available water (blue dash-dotted line). The upper and lower limits are the soil moisture at saturation and permanent wilting point, respectively. The vertical dashed lines represent the growing period, from the sowing (left) to the harvest (right).

The soil moisture trend for the other crops are reported in Figure A.3 (see appendix A).

The aggregation of zones influenced by water retention (dug ponds) and not produces a trend that even if it is always below the threshold, constant permanence of stress condition (red zone), it is closer to the green zone when RWHT are adopted. For all HM configurations, the level of soil moisture is always higher than TM. The gap is lessened only in correspondence of the two more severe precipitation events, where even the retention capacity of HM is surmounted. Indeed, these events are so intense that they almost totally minimize the impact of the PP. All RWHT show to be more effective at the beginning and at the end of the wet season due to the capability to collect more efficiently the surface runoff.

Focusing on the growing period of the analysed crops, the water stress is stated by a level of soil moisture lower than the threshold. The higher level of soil water content induced by the RWHT indicates that there is an improvement of the hydrological efficiency of the whole farmland. In terms of water stress mitigation ($\phi_S$), HM configurations show an efficiency comprised between 21% and 40% while PP lead to significantly lower values from 3% to 11% (Table 4.5). Even in this context, deeper ponds are averagely more efficient than shallower ones. Only for sesame and sweet potato, $HM_{20}$ show the best performance with values of $\phi_S$ slightly higher than the deepest HM. For millet, the values related to the PP configurations are very low because for almost the first third of the growing season, from July to mid of August, the water content results lower than TM. Conversely, for sweet potato, $\phi_S$ values are sensibly higher since the soil moisture of PP is higher than TM most of the time.

Table 4.5 Water stress mitigation efficiency at the field scale for the three typical Sahelian crops.

| **RWHT** | $\phi_{S,millet}$ [%] | $\phi_{S,sesame}$ [%] | $\phi_{S,sweet\ potato}$ [%] |
|---|---|---|---|
| $HM_{30}$ | 23.02 | 34.88 | 39.72 |
| $HM_{20}$ | 22.92 | 36.65 | 39.91 |
| $HM_{10}$ | 20.72 | 33.72 | 35.43 |
| $PP_{20}$ | 3.75 | 7.74 | 12.93 |
| $PP_{10}$ | 2.85 | 6.49 | 11.15 |

## 4.3.2  Hydrological behaviour at the pond scale

The presence of zones characterized by different soil physical characteristics and morphology implies a slightly large spatial variability of hydrological conditions, see Figure 4.6.
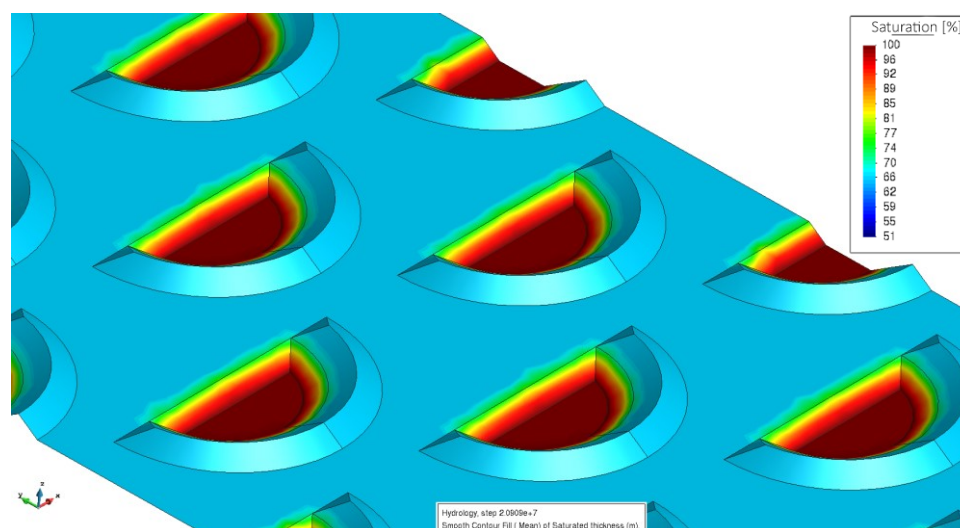


Figure 4.6 Overview of the hydrological behaviour of the $HM_{30}$ configuration. The colouring shows the saturation gradient over the domain.

Downscaling the observation from the field scale to the single row/pond it is possible to deeply investigate the impact of agricultural practices on soil moisture dynamics and their benefit on farming.

Analysing the soil moisture trend for all configurations (Figure 4.7), it is noticeable that for HM, the soil moisture inside of the pond is higher than the threshold most of the time. This avoids that the crop sowed inside of the micro-basin may be affected by water shortage. Comparing the three HM configurations it can be observed that soil moisture in $HM_{30}$ is close to the saturation most of the time and never reaches the threshold. Conversely, at the end of the growing period, shallower HM cross the threshold leading to 2 and 7 days of plant water stress for $HM_{20}$ and $HM_{10}$, respectively. In those days, the limitation in soil water availability induces a condition of stress to the crop which limits its evapotranspiration, implying a $K_s$ lower than 1. The number of stressed days rises to 60 days in case of traditional sowing method. Hence, considering a growing season of 105 days for millet, the crop will suffer water stress more than half the time whether cultivated with the traditional method. The percentage of time considerably decreases to 0%, 2%, and 7% whether $HM_{30}$, $HM_{20}$ and $HM_{10}$, respectively, are adopted. Instead, in contradiction with the results showed in the

previous section, both PP configurations are able to keep the soil water content higher than the threshold over the entire growing season.

The additional information that also stands out in Figure 4.7 is that the soil water content rapidly decreases with the end of the rain season and the increase of the temperature (see also Figure 4.4). This is due to the high intensity of outcoming fluxes and absence of inflows. In TM configuration, the soil moisture reaches the threshold on 8th of October, just 2 days after the last simulated rainfall, and then starts to decrease from the onset of the dry season. The higher storage induced by the RWHT allows extending the growing season up to 20 days, avoiding the stress condition almost until the end of the month.
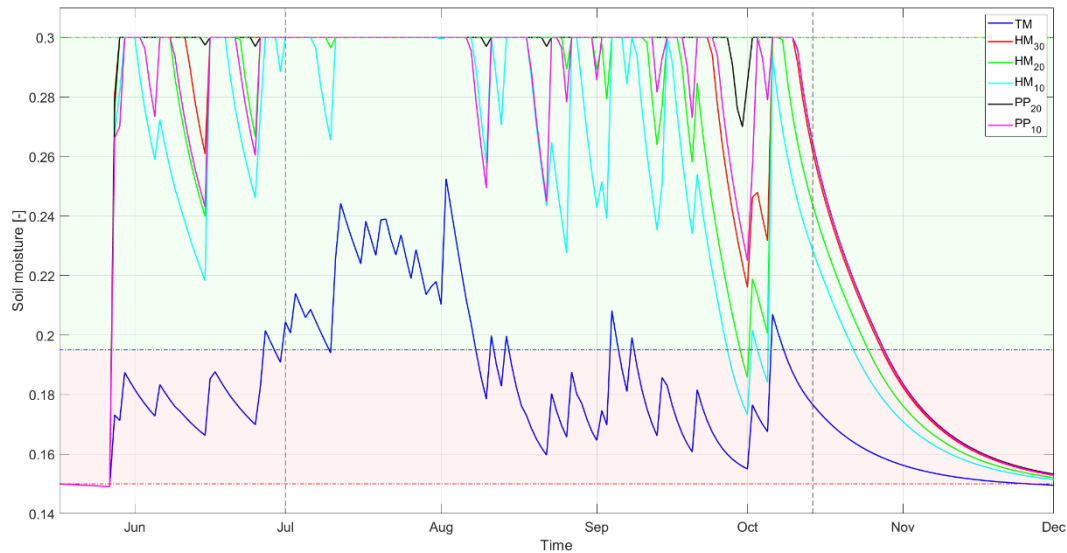


Figure 4.7 Soil moisture trend at the small scale over the wet season for millet. The red area represents the level of water content lower than the threshold in which the crop is water stressed. The green area highlights the range in which soil water availability is enough to meet the demand of the crop. The boundary between the two areas corresponds to the threshold of readily available water (blue dash-dotted line). The upper and lower limits are the soil moisture at saturation and permanent wilting point, respectively. The vertical dashed lines represent the growing period, from the sowing (left) to the harvest (right).

The soil moisture trends for the other crops are reported in Figure A.4 (see appendix A).

To observe the benefits induced using RWHT on crop cultivation, the water balance during the growing season of millet, sesame, and sweet potato was performed for the conventional sowing method and then compared with RWHT practices. The different phenological parameters of these crops lead to different evapotranspiration trends and therefore a different water requirement for the plant growing. Moreover, the characteristic growing period of each crop differently intercepts the rainfall pattern.

The benefit linked with the presence of RWHT was measured as the reduction of cumulative plant water deficit ($PWDR$), see Figure 4.8. The $PWD$ was calculated as the difference between the crop evapotranspiration (evapotranspiration under unstressed condition, see equation (4.5)) and the actual evapotranspiration.
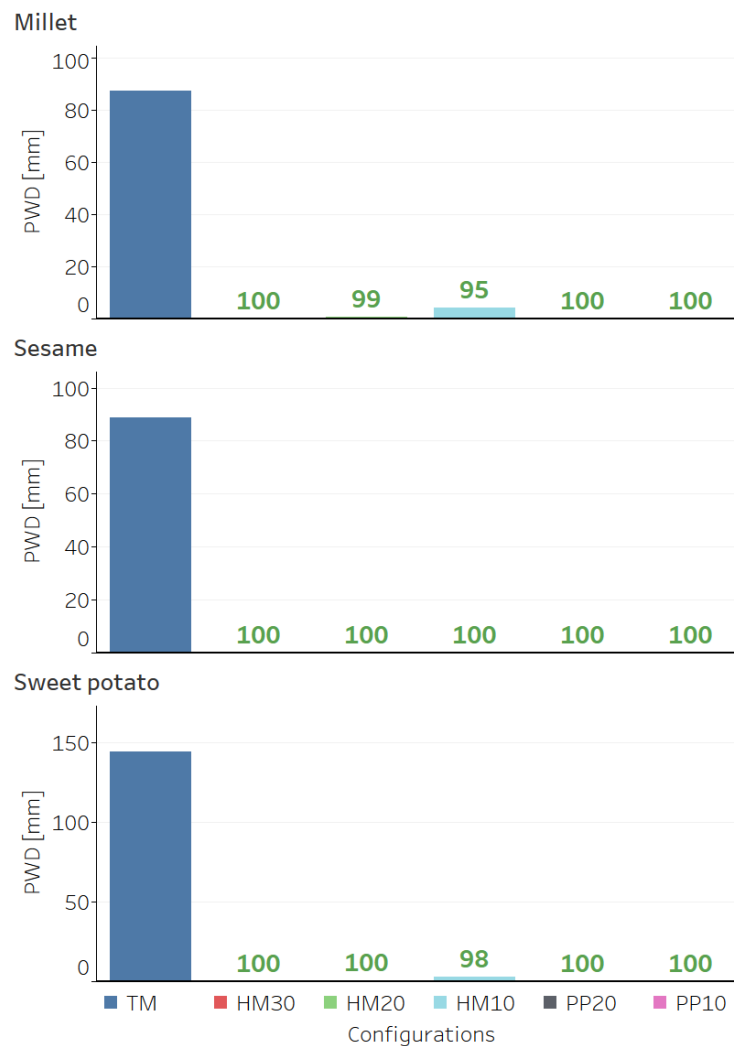


Figure 4.8 Cumulative plant water deficit induced by the use of the traditional sowing method or adopting RWHT for three traditional Sahelian crops. The green bold values indicate the PWDR when RWHT are used.

Figure 4.8 displays the evident fact that for all crops, the presence of the RWHT noticeably decreases the $PWD$, even until zero. The maximum reduction is obtained for the sesame since no deficit is produced when using any RWHT. This occurs since the sesame harvesting takes place around mid-September, hence before the end of rainfalls and increase of temperature. Instead, the longer growing season of sweet potato undermines the traditional system leading to a

higher *PWD*. Looking at all RWHT and their design, $HM_{30}$, $PP_{20}$ and $PP_{10}$ never produce *PWD*, while $HM_{10}$ brings a slight deficit for millet and sweet potato. $HM_{20}$ show an insignificant *PWD* of 1 mm over the entire millet growing season.

## 4.4   Discussion

By definition, the principal aim of using RWHT is to harvest the rainfall and runoff in order to maximize the availability of water for crop and to minimize the water deficit during the entire growing season [47]. In drylands, where food security is the first challenge, reducing water stress means decreasing the probability of crop failure promoting food security [198].

The results presented in this chapter provide a deep analysis of the hydrological functioning of Sahelian agricultural practices.

The great usefulness of RWHT can be observed at the beginning of the rainfall season. Together with the first precipitation, there is a fast increase in soil moisture making the soil more suitable to accommodate new seeds. Indeed, seeds that are commonly planted after cumulative precipitation of 20 mm [196], throughout the planting period, will find a more moist soil which will contribute to germination. The higher level of soil moisture enhances the biological activity which contributes to improving the soil structure avoiding the crustification of the surface and hence the reduction of hydraulic conductivity [185]. It will also help the recovery of grass between the basins, for the sustenance of cattle, or the implementation of intercropping. A recent study showed how the application of intercropping strategies lead to a greater yield as compared with the monoculture [199]. This would also support the return on the route of the African heritage. Indeed, African agriculture has always been a polyculture; the monoculture is a legacy of the colonial period (citing Professor Cheikh Mbow).

The water balance also confirms that with the use of RWHT it is not possible to extend the growing season much after the end of the rains since the high magnitude of outflowing fluxes rapidly empty the soil water storage. However, considering that commonly the rainy season ends at the beginning of October, the use of HM or PP may guarantee a sufficient availability of water up to the end of the month. Furthermore, in such hydrometeorological conditions, it is preferable to cultivate from the beginning of June to the mid of September and harvest no later than the end of September.

As reported in previous works [78,197], the improvement of soil moisture is a phenomenon spatially limited under the pond, since the lateral transport is

negligible (see Figure 4.9). For this reason, the soil between the ponds is much drier than below them. Hence, combining RWHT with other surface treatments will improve the hydrological efficiency of the whole farmland.



Figure 4.9 Overview and a close-up of the moisture spatial distribution after rainfall in a field with RWHT [200].

Knowing the spatial dishomogeneity of the moisture accumulation, the analysis at the two spatial scales allowed to appreciate the real effectiveness of RWHT for agricultural purposes. For PP, the observation at the field scale produced a scarce attenuation of the soil water stress, much lower than HM. This discrepancy may be attributed to the spatial layout of the two techniques. Indeed, the area treated, i.e. the area interested by ponds, in PP configuration is only 7.4% of the field surface, while in the HM configuration it covers almost 20%. Instead for TM, the area treated, i.e. where the surface crust is broken, is the almost 22% of the whole surface. Conversely, at the small scale, the results revealed that both PP configurations lead to a soil moisture trend even higher than HM.

Analysing the cultivation of different crops with or without RWHT, it is noticeable the impact of these techniques that are able to incredibly minimize the water deficit over the entire growing season. The right design can efficiently prevent any water stress condition, helping the plant to maximize its yield. Additionally, as aforementioned in the conclusion of the previous chapter, the right design may avoid excessive excavations leading to considerable time and manual labour-saving.

RWHT have their limitations in the fight against food insecurity. Their advantages mainly concern the increase in available water for crop and overland flow management. However, they are not able to improve the nutrient in soils that are naturally poor in organic matter. Thus, in order to increase the crop yield, the realization of RWHT should be always followed by the addition of manure or

fertilizer [8,58]. However, altering the surface roughness and slowing overland fluxes (runoff and wind), RWHT help to capture organic debris which provides nutrients for the natural regeneration of shrubs and agropastoral bush-woodland [80]. Additionally, decreasing the power of the surface runoff, they work also as anti-erosive actions presenting the integrity of the topsoil and avoiding that precious nutrients are flushed away. Consequently, more stable soil raises the survival capacity of the emerging vegetation. The combination of these joint effects inevitably leads to the filling of the micro-basins, which require annual maintenance to restore their storage capacity.

## 4.5   Concluding remarks

Water and food scarcity are among the main problems that undermine the livelihood of Sahelian inhabitants. To cope with these threats, a growing number of farmers living in sub-Saharan drylands are already taking advantages from the use of improved water and soil management practices.

In this chapter advanced numerical modelling is exploited to investigate the hydrological functioning of those RWHT locally used in the Sahel.

The results show the extraordinary benefits brought by the increment of infiltration and soil moisture, which leads to a considerable reduction of crop water stress along with the growing season.

In terms of water stress mitigation, the right design can bring the soil water deficit to zero, maximizing the crop yield and avoiding the necessity of supplementary irrigation.

The methodology proposed could be very useful to scrupulously plan the irrigation to avoid crop water stress, in areas where water scarcity makes the value of water even higher. The irrigation can be quantified in terms of the amount of water needed to meet the crop demand and scheduled, supplying the right amount of water when soil water content drops below the threshold. Indeed, maximizing the water use efficiency and avoiding the crop water stress, the crop yield increases, approaching the food security in the Sahel.

To deeply analyse the crop life cycle, the relatively simple formulation chosen to evaluate the potential evapotranspiration could represent a weakness point since it does not take into account all physical and physiological factors governing the evapotranspiration process. Notwithstanding these limitations, it addresses a preliminary calculation of the potential evapotranspiration coping with the scarcity of data that often characterize developing countries. Further

implementations could involve more complex formulations including more parameters such as solar radiation, humidity, and wind speed (e.g., the FAO-56 Penman-Monteith approach or the Hargreaves–Samani equation).

The methodology proposed would enlarge the field of application of hydraulic and hydrological models to ecological/agronomic context. Agro-hydrological physically-based models could be effective tools to investigate impacts of climate on the crop life cycle, its health, and yield, without neglecting the hydrodynamics that controls the runoff formation and flow.

In the Sahel, despite the considerable effort in embracing improved land and water management practices, the adoption of these strategies remains too limited to lead a considerable change in Africa's food and environmental security. Thus, this research should encourage to scale up these practices to make widespread the fight against food/water scarcity and environmental degradation. The results demonstrate that, in these contexts, it is not necessary to resort to "high-tech" solutions and unaffordable strategies to deal with such problems. National policies should invest in the education of farmers so that they can gain awareness of the benefits derived from appropriate practices.

# Chapter 5

# Final conclusions

The present dissertation contributes to both the scientific literature and decision-makers needs of understanding the threats related to hydroclimatic extremes and implementing strategies to deal with them in a developing context. Furthermore, the methodologies shown represent a noticeable step forward in the comprehensive investigation of rainwater harvesting techniques, extendible to every agricultural practice, in a numerical modelling framework.

The thesis addresses the investigation and provides the assessment of viable strategies to mitigate the harsh impacts of natural hazards, especially against floods and droughts.

The first part of the manuscript (chapter 2) reports all preliminary analyses performed for the implementation of the first EWS on the Sirba river, the main tributary of the MNRB. These analyses span through hydrological, hydraulic, and statistical assessments from the collection of on-site data to the flood hazard assessment of the Sirba's floodplains. The revision and update of the flow time series of the river show a sharp increment in flooding occurrence in recent decades. This shocking trend underlines that quick interventions are necessary for protecting riverine inhabitants. Moreover, it demonstrates how the hydrological functioning of the Sirba catchment is getting worse year after year. The study of the flow permanency, through the flow duration curves, seems to convey that more water is flowing into the river. Despite this apparently good news for a semi-arid context, the amount of precipitation is almost unchanged in recent times and so it is water that reaches immediately the channel during the rainfall. This means that less resource is available for productive scopes (rainfed agriculture) and more water is channelled into the river and feeds rainstorm-induced flood waves. Considering the non-stationarity of the river behaviour makes the evaluation of the flood frequency prediction even worse. Indeed, the probability of occurrence of a catastrophic flood results almost ten times higher than studying the discharge time series with stationary methods. The flood hazard scenarios have been designed with a twofold aim: (i) being thoroughly linked to the context and (ii) being immediately understandable by the majority. To achieve the goal,

the hazard alerts were defined in conformity to the current national protocol and tightly related to the impacts potentially triggered by floods with different magnitudes. Results showed that, despite the incredible spirit of adaptation of people living in riparian areas, many important settlements and assets are prone to be severely damaged by severe flooding events. As abovementioned, the results have a significative practical implication since flood hazard maps are also a useful tool that may guide urban planners and local administrations towards the best decisions for an aware use of the territory.

The significative environmental degradation that affects the Sirba basin and the subsequent deterioration of its hydrological functioning, unfortunately, reflects most of the sub-Saharan drylands. These territories not only share analogous climatic conditions, meaning the Sahelian climate, but their populations have a lot of common points, among which the livelihood systems. These strategies range from the agricultural and fishing practices, livestock herding and trading methods. On the base of these considerations and to make the results applicable on a vast range of contexts, the second part of the thesis (chapter 3) proposes the use of indigenous agricultural practices to simultaneously contrast the ongoing degradation and mitigate the flood risk. The examined practices were widely used in the past and are essentially hand-dug micro-catchments utilized to collect rain and runoff, hence the name of rainwater harvesting techniques. The assessment of their hydraulic efficiency and capacity of reducing the amount of water that flows towards the receptor water body has been accomplished through hydraulic numerical modelling. Two methodologies are presented which exploit two different hydraulic models with different features. The first makes use of HEC-RAS, whereby the benefits induced by the presence of RWHT are analysed at the field and basin scale. At both scales the runoff retention effect is remarkable, and outcomes suggest that the optimal arrangement is in staggered lines. In addition, it was the first scientific application of HEC-RAS for implementing a rainfall-runoff model. However, such application is at an early stage of development and still has some limitations, such as the impossibility of calculating infiltrations (implying the impermeability of the domain). The second methodology adopts the two-dimensional distributed model Iber. This model allows computing further hydrological processes occurring in the formation of the overland flow and so provides a more detailed overview of the RWHT hydraulic functioning. The model was iteratively run in a Monte Carlo analysis to replicate a vast set of scenarios typical of Sahelian farmlands. The outcomes show that the right configuration can retain up to 87% of the whole runoff flowing on the farm field and it may double the amount of water that infiltrates into the ground, refilling the

groundwater. This latter, beyond to be water that does not directly raise the water level into the river, it is a precious freshwater resource for both cropping and humans. Moreover, the strong influence of the physical features of the soil surface on runoff formation suggests that in order to optimize the whole farmland, the excavation of the ponds should be coupled with superficial treatments also between the micro-basins. The adopted approach highlights how the hydraulic performances are solidly related to the RWHT design and hydrological forcing agents. Thus, considering the ongoing climate trend, the intensification of hydrometeorological extremes should be evaluated in the planning phase in order to maximize the benefits deriving from the use of these techniques. Furtherly, the comparison between the outcomes of the two numerical models suggests that the computation of hydrological losses is not negligible at all, even whether of secondary importance with respect to the micro-basin design. Therefore, future studies should opt for hydrological models, instead of a pure hydraulic model, for studies which involve runoff formation and propagation processes.

Following this last consideration, the third part of this thesis (chapter 4) exploits Iber again to provide a comprehensive analysis concerning the improvements tied with the use of RWHT in reducing the drought-related water stress which affects Sahelian crops. The capabilities of Iber to compute the soil water balance at each computational cell were expanded introducing a hybrid methodology for the calculation of outgoing fluxes from the crop root zone, meaning the evapotranspiration. The proposed method combines the prompt assessment of the potential evapotranspiration via the empirical relation of Doorenbos and Pruitt, with the single-crop coefficient method presented in the FAO Irrigation and Drainage Paper-56. This coupling allowed accounting for the phenological features of plants and the water stress-induced effects without requiring several inputs, dealing with the scarcity of data that often characterize developing countries. The analyses show that the water stress mitigation may be optimized by a well-designed RWHT, completely avoiding the soil water deficit and the need for supplementary irrigation. Moreover, the right design may avoid oversized basin, up to two-thirds of the total excavation, saving a lot of hours of manual labour. This effort might be re-invested towards upscaling the realization of these practices for improving the hydrological functioning of vast drylands.

The thesis shows different numerical methodologies for the evaluation of Sahelian agricultural practices, but their application is absolutely not limited to this context. Indeed, they are suitable for other agricultural studies elsewhere in the world. The expensive on-site studies and the increasing availability of

database collecting various types of data make the choice of numerical model-based approach an effective option that can be easily replicated for different sites.

In the fight against hydrometeorological extremes, decision-makers could opt for more sophisticated interventions, such as large reservoirs to prevent floods and retain water immediately available for irrigation. Notwithstanding the unquestionable usefulness, large water mirrors are prone to waste a large amount of precious resource due to the high evaporation ratio related to the extremely high temperature that dominates the Sahelian climate. Thus, the benefit related to the infiltration increase led to the use of RWHT may partially solve this problem, storing water underground. In sub-Saharan countries, where most of the populations are agro-pastoralists, farmers should invest their energy in a larger use of RWHT to face simultaneously food security, land degradation and climate-related risk. Besides the technical aspects, social factors play a crucial role in Sahelian communities, where the idea of improving farmlands that are communally cultivated is quite unknown. The success of a project, in which an investment promotes the use of RWHT, will strictly depend upon the acceptance of the system by local farmers. Indeed, beneficiaries should be actively engaged in all phases of the project, from the planning, implementation to the maintenance of the water harvesting system. Whether this condition is not respected, despite the most effective knowledge transfer, the plan is bound to fail. Thus, the participative collaboration between land users and decision-makers might start an agricultural revolution promoting the dissemination of these indigenous practices on a wider scale. A future challenge may be the development of watershed management strategies which focus on RWHT as the driver for pursuing the mitigation of hydrometeorological-related threats and triggering a process of environmental restoration.

## 5.1 Limitations and recommendations for future progress

All analyses carried out in this dissertation are based on data collected from institutional databases and on-site measurements, and model concepts and assumptions. With regards the first part of the thesis, the recalibration of the rating curves of Garbey Kourou and the new assessment of the BB RC have been accomplished on the basis of a limited number of measurements. Despite the choice of split up the RC equation's range of validity into two intervals proved to be a successful approach, it leads to a slight uncertainty in correspondence of the

changepoint. This gap could be reduced incrementing the number of on-site measurements in order to optimize the process of linear regression.

Concerning the conceptualization of RWHT and simulation of the hydrodynamics and hydrological processes controlling the transformation of rainfall in runoff, some considerations can be advanced. The geometrical conceptualization was optimized to respect the real shape of digs and ridges and according to the constraints linked with the spatial discretization applied by the two models. Concerning the geometrical specifications, further studies should examine different designs and test the influence of the slope on the hydraulic efficiency. This latter insight could help to choose the best design or technique based on the topography of the study area. Moreover, simulating further meteorological forcing would allow mapping the best design for a specific RWHT based on the hydroclimatic features of each Sahelian area. This would represent a technical guideline useful for guiding local farmers in the right implementation of the most suitable practice for their farmlands.

The findings of this thesis could be also used to upscale the hydrological analyses from the field scale to a wider scale following the parametrization of the RWHT, as demonstrated by the results obtained using the methodology 1. More in detail, knowing how of the presence of RWHT affects the runoff coefficient, e.g. reduction of the curve number, it is possible to run the hydrological model without directly altering the computational domain but only setting the correct parameter for those treated areas. This avoids significantly increasing the computational load tied with the reduction of the size of the cells to shape the RWHT.

The last but not least recommendation, other hydrometeorological hazards might be investigated through the methodology implemented and tested in this thesis. An example is the hazard tied with the surface runoff, the soil erosion. The efficiency of RWHT in reducing soil erosion induced by extreme rainfall and the quantification of topsoil displacement could be achieved coupling the presented approach with the procedure experienced in the work of Cea et al. [170].

# Appendix

## A – Supplementary materials
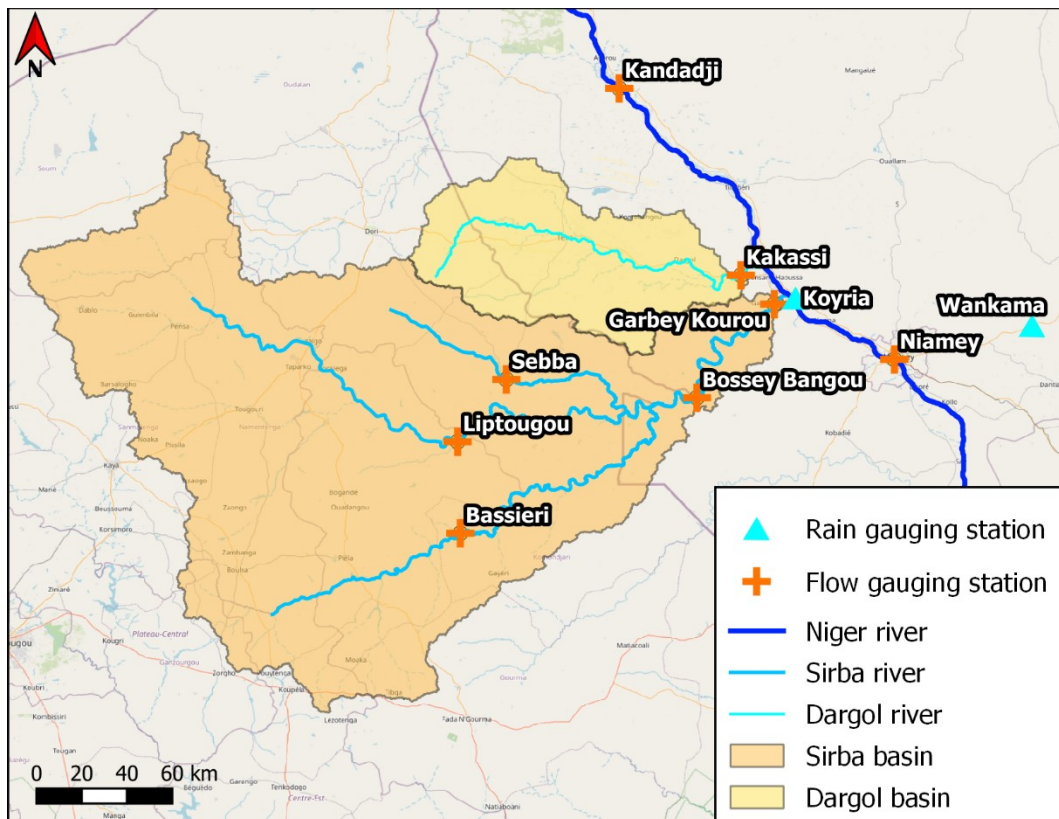


Figure A.1 Analysed flow and rain gauging stations in MNRB.
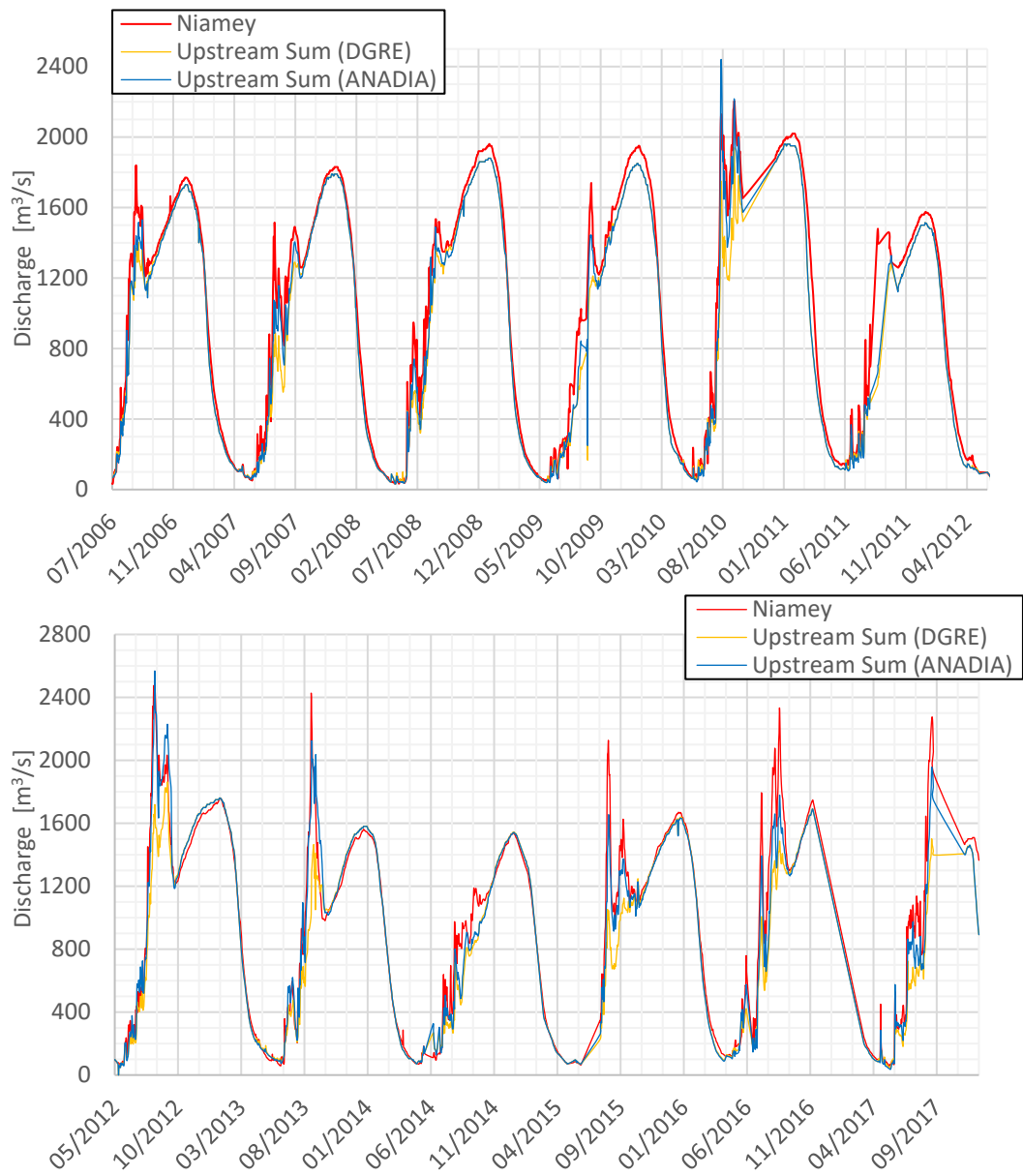
Figure A.2 Geometrical scheme of the conceptual configurations.
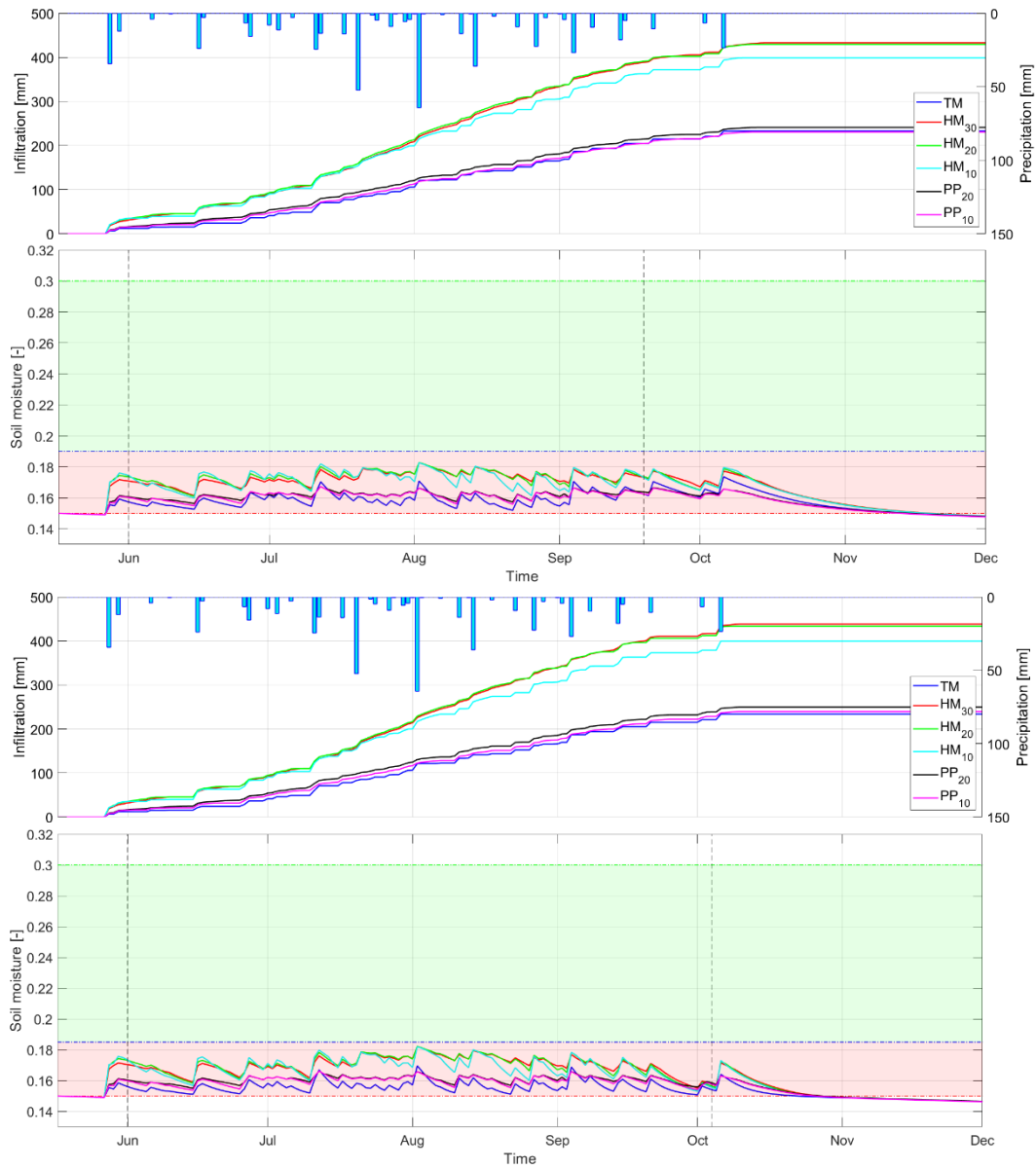
Figure A.3 Soil moisture trend at the small scale over the wet season for sesame (upper graph) and sweet potato (lower graph). The red area represents the level of water content lower than the threshold in which the crop is water stressed. The green area highlights the range in which soil water availability is enough to meet the demand of the crop. The boundary between the two areas corresponds to the threshold of readily available water (blue dash-dotted line). The upper and lower limits are the soil moisture at saturation and permanent wilting point, respectively. The vertical dashed lines represent the growing period, from the sowing (left) to the harvest (right).
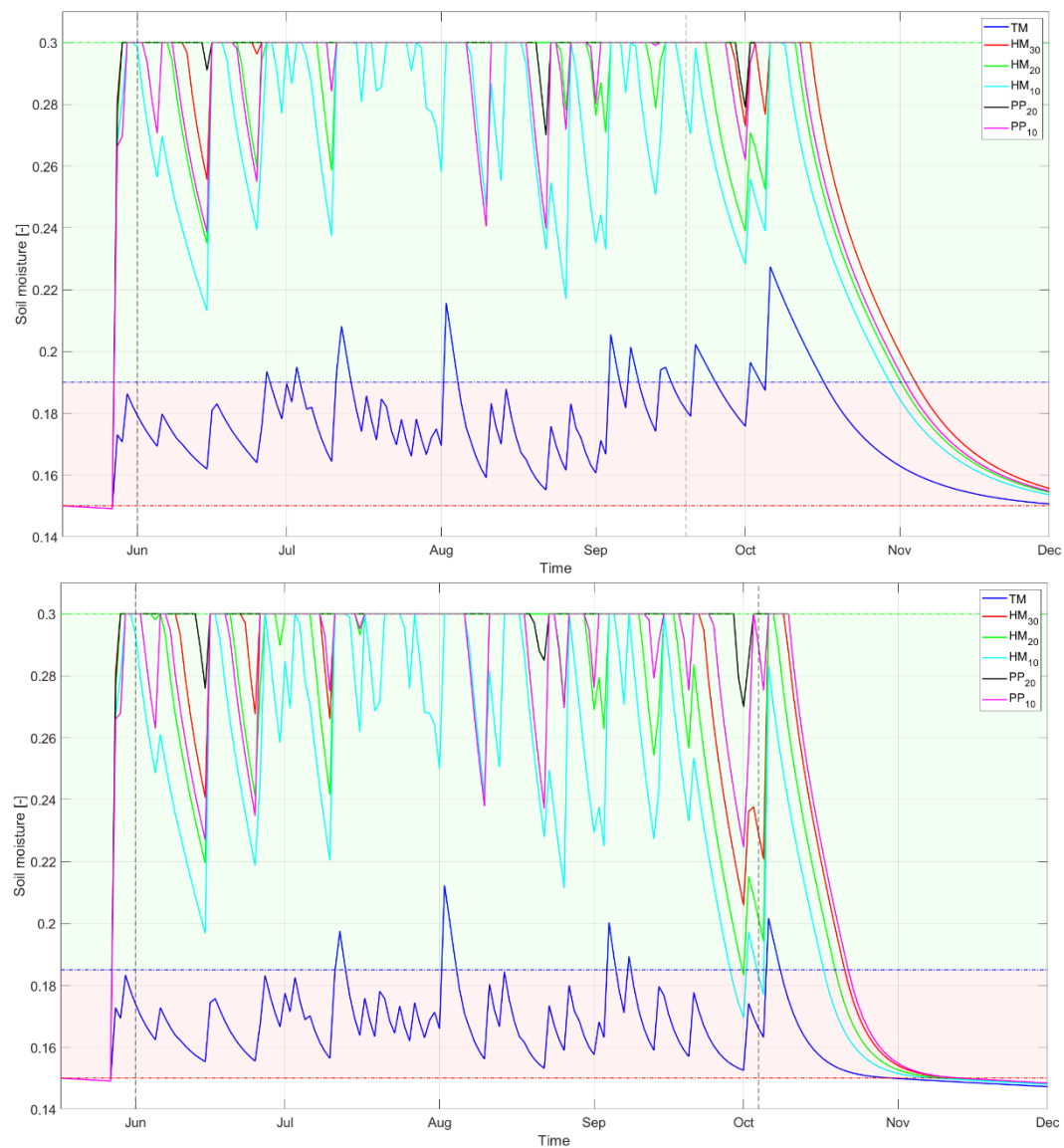
Figure A.4 Soil moisture trend at the small scale over the wet season for sesame (upper graph) and sweet potato (lower graph). The red area represents the level of water content lower than the threshold in which the crop is water stressed. The green area highlights the range in which soil water availability is enough to meet the demand of the crop. The boundary between the two areas corresponds to the threshold of readily available water (blue dash-dotted line). The upper and lower limits are the soil moisture at saturation and permanent wilting point, respectively. The vertical dashed lines represent the growing period, from the sowing (left) to the harvest (right).

# B – Geometrical specifications
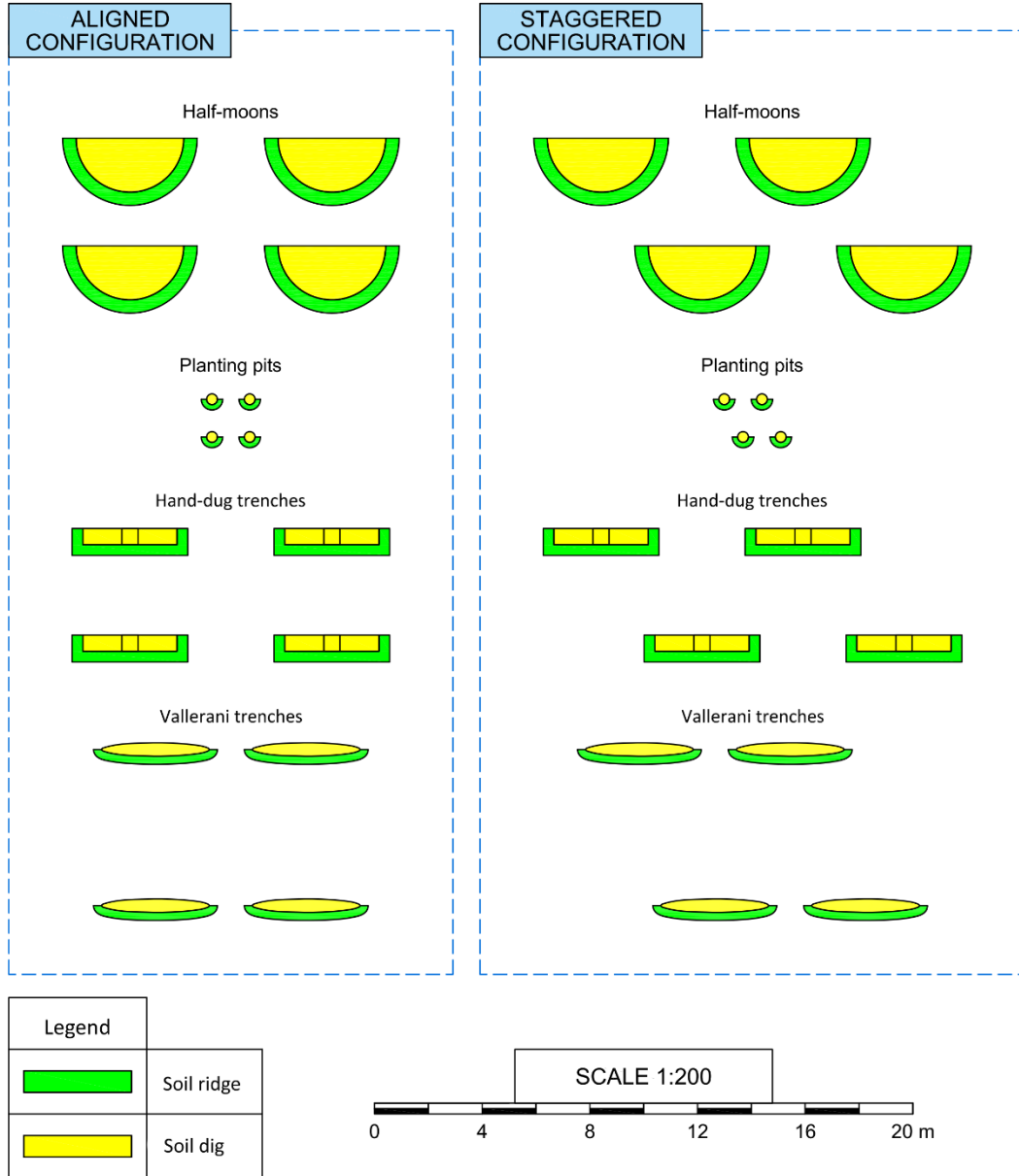


Figure B.1 Geometrical scheme of the conceptual configurations.
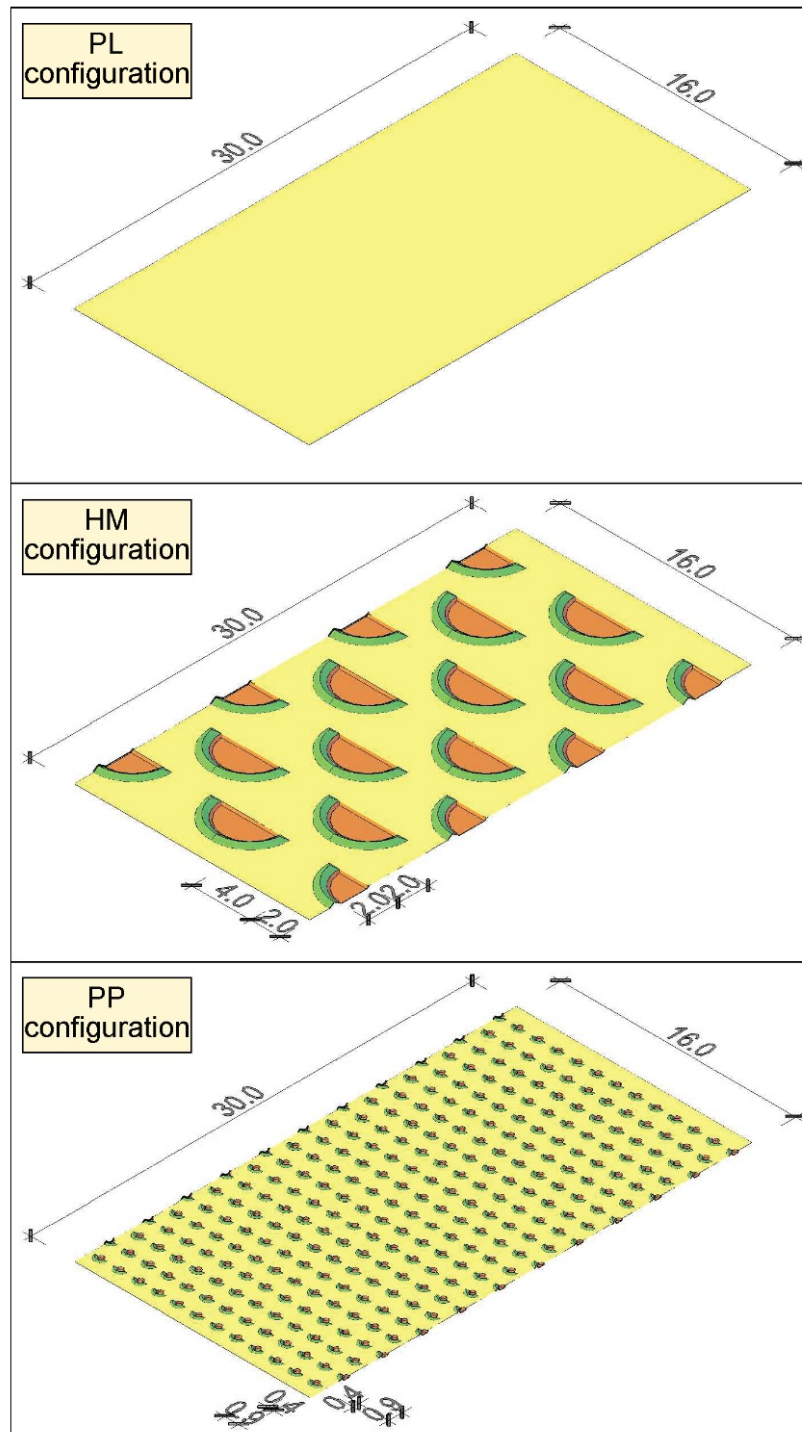
Figure B.2 Geometrical characteristics of the spatial domains used for simulations. All measures are in meters. All plots present a constant slope of 1% towards downstream. Colouring: red represents the treated surfaces (tilled areas), green displays ridges (realized from the excavated terrain), yellow shows the untreated surfaces (crusted areas).
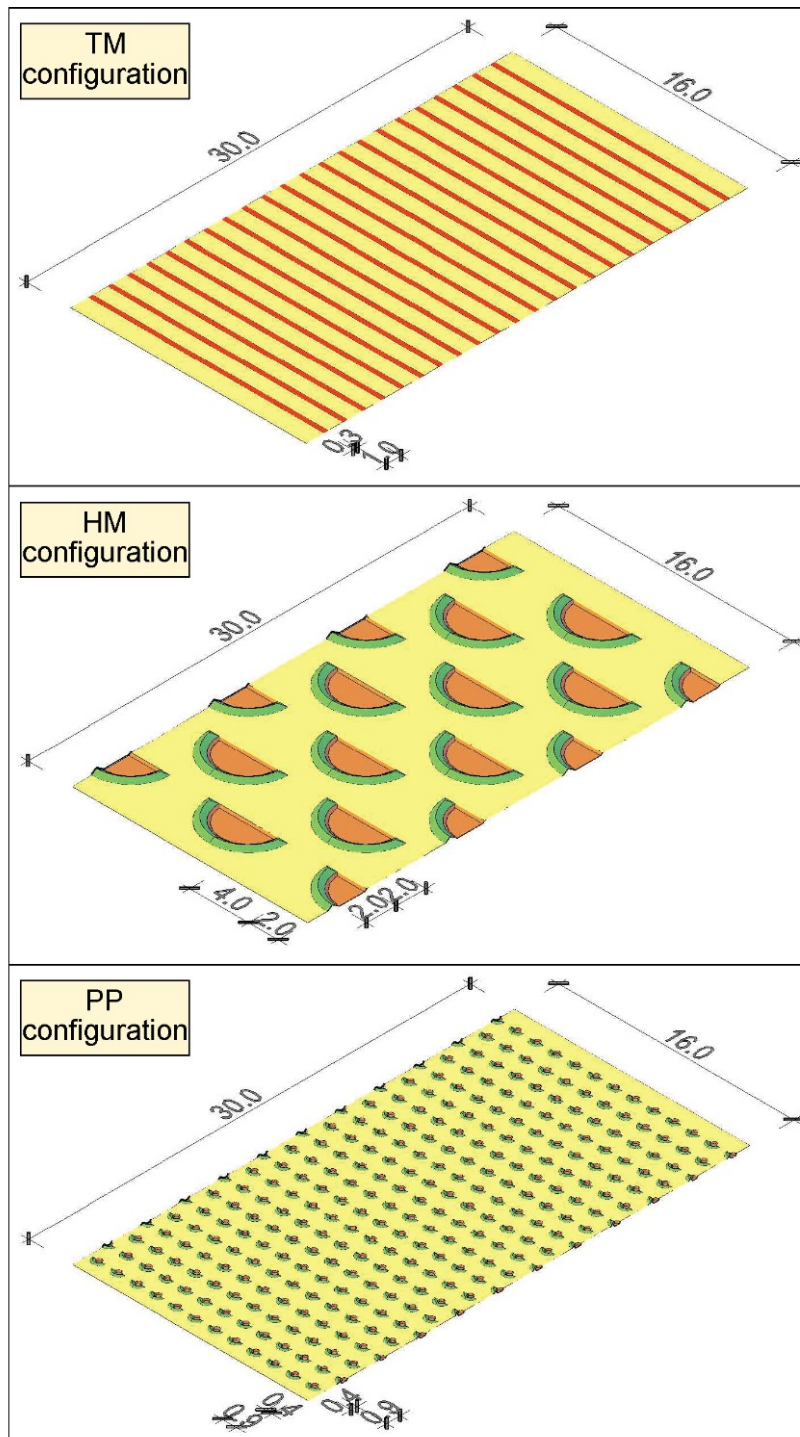
Figure B.3 Geometrical characteristics of the spatial domains used for simulations. All measures are in meters. All plots present a constant slope of 1% towards downstream. Colouring: red represents the treated surfaces (tilled areas), green displays ridges (realized from the excavated terrain), yellow shows the untreated surfaces (crusted areas).

# C – Scientific contributions and publications

The work described in this dissertation has been shared with the scientific community through the following articles:

- Tamagnone, P.; Massazza, G.; Pezzoli, A.; Rosso, M. Hydrology of the Sirba River: Updating and Analysis of Discharge Time Series. *Water* 2019, *11*, 156, doi:10.3390/w11010156.

- Massazza, G.; Tamagnone, P.; Wilcox, C.; Belcore, E.; Pezzoli, A.; Vischel, T.; Panthou, G.; Housseini Ibrahim, M.; Tiepolo, M.; Tarchiani, V.; et al. Flood Hazard Scenarios of the Sirba River (Niger): Evaluation of the Hazard Thresholds and Flooding Areas. *Water* 2019, *11*, 1018, doi:10.3390/w11051018.

- Tamagnone, P.; Comino, E.; Rosso, M. Landscape Metrics Integrated in Hydraulic Modeling for River Restoration Planning. *Environ. Model. Assess.* 2020, doi:10.1007/s10666-020-09693-y.

- Tamagnone, P.; Comino, E.; Rosso, M. Rainwater harvesting techniques as an adaptation strategy for flood mitigation. J. Hydrol. 2020, 586, 124880, doi:10.1016/j.jhydrol.2020.124880.

- Tamagnone, P.; Cea, L.; Comino, E.; Rosso, M. Rainwater Harvesting Techniques to Face Water Scarcity in African Drylands: Hydrological Efficiency Assessment. *Water* 2020, *12*, 2646, doi:10.3390/w12092646.

or have been presented, as oral or poster presentation, at the following events:

- Tamagnone, P. Data analysis, flood hazard assessment and mitigation in arid and semi-arid regions. PhD Days del Gruppo Italiano di Idraulica (GII), Università di Parma, Parma, Italy. July 2019.

- Tamagnone, P.; Comino, E.; Rosso, M. Hydraulic Performance Evaluation of Rainwater Harvesting Techniques to face climate changes in dry environments. 2019 Environmental Science and Climate Change Conference, Singapore. September 2019.

- Tamagnone, P.; Cea, L.; Comino, E.; Rosso, M. A numerical model approach to evaluate the efficiency of indigenous rainwater harvesting techniques for agriculture. The 8th World Sustainability Forum, Geneva, Switzerland. September 2020.

# References

1.  *Poverty and Shared Prosperity 2018: Piecing Together the Poverty Puzzle*; Poverty and Shared Prosperity; The World Bank, 2018; ISBN 978-1-4648-1330-6.

2.  Searchinger, T.; Hanson, C.; Waite, R.; Lipinski, B. Achieving replacement level fertility. *Work. Pap. Install. 3 Creat. Sustain. Food Future* 2013.

3.  Potts, M.; Henderson, C.; Campbell, M. The Sahel: A Malthusian Challenge? *Environ. Resour. Econ.* 2013, *55*, 501–512, doi:10.1007/s10640-013-9679-2.

4.  Department of Economic and Social Affairs *World Population Prospects 2019Volume I: Comprehensive Tables*; 2019; ISBN 978-92-1-148327-7.

5.  United Nations Development Programme Human Development Index (HDI) | Human Development Reports Available online: http://hdr.undp.org/en/content/human-development-index-hdi (accessed on Sep 22, 2020).

6.  FAO; IFAD; UNICEF; WFP; WHO. *The State of Food Security and Nutrition in the World 2019. Safeguarding against economic slowdowns and downturns.*; FAO: Rome, 2019; ISBN 978-92-5-131570-5.

7.  Winterbottom, R.; Reij, C.; Garrity, D.; Glover, J.; Hellums, D.; Mcgahuey, M.; Scherr, S. Improving Land and Water Management. *Work. Pap. Install. 4 Creat. Sustain. Food Future* 2013.

8.  Breman, H.; Groot, J.J.R.; van Keulen, H. Resource limitations in Sahelian agriculture. *Glob. Environ. Change* 2001, *11*, 59–68, doi:10.1016/S0959-3780(00)00045-5.

9.  Niang, I.; Ruppel, O.; Abdrabo, M.; Essel, A.; Lennard, C.; Padgham, J.; Urquhart, P. Climate change 2014: impacts, adaptation and vulnerability. Contribution of Working Group II to the Fifth Assessment Report of the Intergovernmental Panel on Climate Change. In; Cambridge University Press: Cambridge, 2014; Vol. 2, pp. 1199–1266 ISBN 978-1-107-68386-0.

10. *Climate change 2014: impacts, adaptation, and vulnerability: Working Group II contribution to the fifth assessment report of the Intergovernmental Panel on Climate Change*; Field, C.B., Barros, V.R.,

Intergovernmental Panel on Climate Change, Eds.; Cambridge University Press: New York, NY, 2014; ISBN 978-1-107-64165-5.

11. Lebel, T.; Ali, A. Recent trends in the Central and Western Sahel rainfall regime (1990-2007). *J. Hydrol.* 2009, *375*, 52–64, doi:10.1016/j.jhydrol.2008.11.030.

12. Barbé, L. Le; Lebel, T. Rainfall climatology of the HAPEX-Sahel region during the years 1950–1990. *J. Hydrol.* 1997, *188–189*, 43–73, doi:https://doi.org/10.1016/S0022-1694(96)03154-X.

13. Nicholson, S. On the question of the "recovery" of the rains in the West African Sahel. *J. Arid Environ.* 2005, *63*, 615–641, doi:https://doi.org/10.1016/j.jaridenv.2005.03.004.

14. Descroix, L.; Guichard, F.; Grippa, M.; Lambert, L.; Panthou, G.; Mahé, G.; Gal, L.; Dardel, C.; Quantin, G.; Kergoat, L.; et al. Evolution of Surface Hydrology in the Sahelo-Sudanian Strip: An Updated Review. *Water* 2018, *10*, 748–748, doi:10.3390/w10060748.

15. Dardel, C.; Kergoat, L.; Hiernaux, P.; Grippa, M.; Mougin, E.; Ciais, P.; Nguyen, C.-C. Rain-Use-Efficiency: What it Tells us about the Conflicting Sahel Greening and Sahelian Paradox. *Remote Sens.* 2014, *6*, 3446–3474, doi:10.3390/rs6043446.

16. Panthou, G.; Lebel, T.; Vischel, T.; Quantin, G.; Sane, Y.; Ba, A.; Ndiaye, O.; Diongue-Niang, A.; Diopkane, M. Rainfall intensification in tropical semi-arid regions: the Sahelian case. *Environ. Res. Lett.* 2018, *13*, 064013, doi:10.1088/1748-9326/aac334.

17. Descroix, L.; Diongue Niang, A.; Panthou, G.; Bodian, A.; Sane, Y.; Dacosta, H.; Malam Abdou, M.; Vandervaere, J.-P.; Quantin, G. Évolution récente de la pluviométrie en Afrique de l'ouest à travers deux régions : la Sénégambie et le Bassin du Niger Moyen. *Climatologie* 2015, doi:10.4267/climatologie.1105.

18. Panthou, G.; Vischel, T.; Lebel, T. Recent trends in the regime of extreme rainfall in the Central Sahel. *Int. J. Climatol.* 2014, *34*, 3998–4006, doi:10.1002/joc.3984.

19. Zahiri, E.-P.; Bamba, I.; Famien, A.M.; Koffi, A.K.; Ochou, A.D. Mesoscale extreme rainfall events in West Africa: The cases of Niamey (Niger) and the Upper Ouémé Valley (Benin). *Weather Clim. Extrem.* 2016, *13*, 15–34, doi:10.1016/j.wace.2016.05.001.

20. Giorgi, F.; Im, E.-S.; Coppola, E.; Diffenbaugh, N.S.; Gao, X.J.; Mariotti, L.; Shi, Y. Higher Hydroclimatic Intensity with Global Warming. *J. Clim.* 2011, *24*, 5309–5324, doi:10.1175/2011JCLI3979.1.

21. National Centers for Environmental Information Available online: https://www.ncdc.noaa.gov/cag/global/time-series/africa/land/1/7/1910-2019?trend=true&trend_base=10&firsttrendyear=1880&lasttrendyear=2019 .

22. Taylor, C.M.; Belušić, D.; Guichard, F.; Parker, D.J.; Vischel, T.; Bock, O.; Harris, P.P.; Janicot, S.; Klein, C.; Panthou, G. Frequency of extreme Sahelian storms tripled since 1982 in satellite observations. *Nature* 2017, *544*, 475–478, doi:10.1038/nature22069.

23. Balme, M.; Vischel, T.; Lebel, T.; Peugeot, C.; Galle, S. Assessing the water balance in the Sahel: Impact of small scale rainfall variability on runoff. *J. Hydrol.* 2006, *331*, 336–348, doi:10.1016/j.jhydrol.2006.05.020.

24. Aich, V.; Liersch, S.; Vetter, T.; Andersson, J.C.M.; Müller, E.N.; Hattermann, F.F. Climate or land use? - Attribution of changes in river flooding in the Sahel zone. *Water Switz.* 2015, *7*, 2796–2820, doi:10.3390/w7062796.

25. Amogu, O.; Esteves, M.; Vandervaere, J.-P.; Malam Abdou, M.; Panthou, G.; Rajot, J.-L.; Souley Yéro, K.; Boubkraoui, S.; Lapetite, J.-M.; Dessay, N.; et al. Runoff evolution due to land-use change in a small Sahelian catchment. *Hydrol. Sci. J.* 2015, *60*, 78–95, doi:10.1080/02626667.2014.885654.

26. Tamagnone, P.; Massazza, G.; Pezzoli, A.; Rosso, M. Hydrology of the Sirba River: Updating and Analysis of Discharge Time Series. *Water* 2019, *11*, 156, doi:10.3390/w11010156.

27. Sighomnou, D.; Descroix, L.; Genthon, P.; Mahé, G.; Moussa, I.B.; Gautier, E.; Mamadou, I.; Vandervaere, J.-P.; Bachir, T.; Coulibaly, B.; et al. The Niger River Niamey flood of 2012: The paroxysm of the Sahelian paradox? *Sécheresse* 20131-2-3, 3–13, doi:10.1684/sec.2013.0370.

28. Descroix, L.; Bouzou, I.; Genthon, P.; Sighomnou, D.; Mahe, G.; Mamadou, I.; Vandervaere, J.-P.; Gautier, E.; Faran, O.; Rajot, J.-L.; et al. Impact of Drought and Land – Use Changes on Surface – Water Quality and Quantity: The Sahelian Paradox. In *Current Perspectives in Contaminant Hydrology and Water Resources Sustainability*; Bradley, P., Ed.; InTech, 2013 ISBN 978-953-51-1046-0.

29. Gal, L.; Grippa, M.; Hiernaux, P.; Pons, L.; Kergoat, L. The paradoxical evolution of runoff in the pastoral Sahel: analysis of the hydrological changes over the Agoufou watershed (Mali) using the KINEROS-2 model. *Hydrol. Earth Syst. Sci.* 2017, *21*, 4591–4613, doi:10.5194/hess-21-4591-2017.

30. Wendling, V.; Peugeot, C.; Mayor, Á.G.; Hiernaux, P.; Mougin, E.; Grippa, M.; Kergoat, L.; Walcker, R.; Galle, S.; Lebel, T. Drought induced regime shift and resilience of a Sahelian eco-hydrosystem. *Environ. Res. Lett.* 2019, doi:10.1088/1748-9326/ab3dde.

31. Amogu, O.; Descroix, L.; Yéro, K.S.; Le Breton, E.; Mamadou, I.; Ali, A.; Vischel, T.; Bader, J.-C.; Moussa, I.B.; Gautier, E.; et al. Increasing River Flows in the Sahel? *Water* 2010, *2*, 170–199, doi:10.3390/w2020170.

32. Descroix, L.; Genthon, P.; Amogu, O.; Rajot, J.L.; Sighomnou, D.; Vauclin, M. Change in Sahelian Rivers hydrograph: The case of recent red floods of the Niger River in the Niamey region. *Glob. Planet. Change* 2012, *98–99*, 18–30, doi:10.1016/j.gloplacha.2012.07.009.

33. Nka, B.N.; Oudin, L.; Karambiri, H.; Paturel, J.E.; Ribstein, P. Trends in floods in West Africa: Analysis based on 11 catchments in the region. *Hydrol. Earth Syst. Sci.* 2015, *19*, 4707–4719, doi:10.5194/hess-19-4707-2015.

34. Aich, V.; Koné, B.; Hattermann, F.F.; Müller, E.N. Floods in the Niger basin — analysis and attribution. *Nat. Hazards Earth Syst. Sci. Discuss.* 2014, *2*, 5171–5212, doi:10.5194/nhessd-2-5171-2014.

35. Casse, C.; Gosset, M.; Vischel, T.; Quantin, G.; Tanimoun, B.A. Model-based study of the role of rainfall and land use-land cover in the changes in the occurrence and intensity of Niger red floods in Niamey between 1953 and 2012. *Hydrol. Earth Syst. Sci.* 2016, *20*, 2841–2859, doi:10.5194/hess-20-2841-2016.

36. Leblanc, M.J.; Favreau, G.; Massuel, S.; Tweed, S.O.; Loireau, M.; Cappelaere, B. Land clearance and hydrological change in the Sahel: SW Niger. *Glob. Planet. Change* 2008, *61*, 135–150, doi:10.1016/j.gloplacha.2007.08.011.

37. Fiorillo, E.; Crisci, A.; Issa, H.; Maracchi, G.; Morabito, M.; Tarchiani, V. Recent Changes of Floods and Related Impacts in Niger Based on the ANADIA Niger Flood Database. *Climate* 2018, *6*, 59, doi:10.3390/cli6030059.

38. Massazza, G.; Tamagnone, P.; Wilcox, C.; Belcore, E.; Pezzoli, A.; Vischel, T.; Panthou, G.; Housseini Ibrahim, M.; Tiepolo, M.; Tarchiani, V.; et al. Flood Hazard Scenarios of the Sirba River (Niger): Evaluation of the Hazard Thresholds and Flooding Areas. *Water* 2019, *11*, 1018, doi:10.3390/w11051018.

39. Aich, V.; Koné, B.; Hattermann, F.F.; Paton, E.N. Time series analysis of floods across the Niger River Basin. *Water Switz.* 2016, *8*, doi:10.3390/w8040165.

40. Tarhule, A. Damaging Rainfall and Flooding: The Other Sahel Hazards. *Clim. Change* 2005, *72*, 355–377, doi:10.1007/s10584-005-6792-4.

41. Erena, S.H.; Worku, H.; De Paola, F. Flood hazard mapping using FLO-2D and local management strategies of Dire Dawa city, Ethiopia. *J. Hydrol. Reg. Stud.* 2018, *19*, 224–239, doi:10.1016/j.ejrh.2018.09.005.

42. Tarchiani, V.; Massazza, G.; Rosso, M.; Tiepolo, M.; Pezzoli, A.; Housseini Ibrahim, M.; Katiellou, G.L.; Tamagnone, P.; De Filippis, T.; Rocchi, L.; et al. Community and Impact Based Early Warning System for Flood Risk Preparedness: The Experience of the Sirba River in Niger. *Sustainability* 2020, *12*, 1802, doi:10.3390/su12051802.

43. ISET-Internationa; urich Insurance Group Ltd Risk Nexus: Urgent case for recovery: what we can learn from the August 2014 Karnali River fl oods in Nepal 2015.

44. Giglio, P.; Bechis, S. *Nuova energia per l'Africa. 45 anni di cooperazione controcorrente nel Sahel*; L'Harmattan Italia: Italia, 2019; ISBN 88-7892-364-8.

45. Serdeczny, O.; Adams, S.; Baarsch, F.; Coumou, D.; Robinson, A.; Hare, W.; Schaeffer, M.; Perrette, M.; Reinhardt, J. Climate change impacts in Sub-Saharan Africa: from physical changes to their social repercussions. *Reg. Environ. Change* 2017, *17*, 1585–1600, doi:10.1007/s10113-015-0910-2.

46. Tiepolo, M. *Planning to cope with tropical and subtropical climate change*; De Gruyter Open: Warsaw, Poland, 2016; ISBN 978-3-11-048079-5.

47. Rockström, J.; Karlberg, L.; Wani, S.P.; Barron, J.; Hatibu, N.; Oweis, T.; Bruggeman, A.; Farahani, J.; Qiang, Z. Managing water in rainfed agriculture—The need for a paradigm shift. *Agric. Water Manag.* 2010, *97*, 543–550, doi:10.1016/j.agwat.2009.09.009.

48. International Water Management Institute, I. *Managing water for rainfed agriculture*; International Water Management Institute (IWMI), 2010.

49. Faures, J.-M.; Santini, G. *Water and the rural poor: interventions for improving livelihoods in Sub-Saharan Africa*; Food and Agriculture Organization: Rome, 2008; ISBN 978-92-5-105982-1.

50. Kodikara, I. *"Climate-Smart" Agriculture*; 2010.

51. Food and Agriculture Organization of the United Nations *Climate-smart agriculture sourcebook.*; 2014; ISBN 978-92-5-107720-7.

52.  United Nations About the Sustainable Development Goals Available online: https://www.un.org/sustainabledevelopment/sustainable-development-goals/ (accessed on Jun 17, 2019).

53.  Sonneveld, B.G.J.S.; Merbis, M.D.; Alfarra, A.; Ünver, İ.H.O.; Arnal, M.F.; Food and Agriculture Organization of the United Nations *Nature-based solutions for agricultural water management and food security*; 2018; ISBN 978-92-5-131125-7.

54.  Tabor, J.A. Improving crop yields in the Sahel by means of water-harvesting. *J. Arid Environ.* 1995, *30*, 83–106, doi:10.1016/S0140-1963(95)80041-7.

55.  Malley, Z.J.U.; Kayombo, B.; Willcocks, T.J.; Mtakwa, P.W. Ngoro: an indigenous, sustainable and profitable soil, water and nutrient conservation system in Tanzania for sloping land. *Soil Tillage Res.* 2004, *77*, 47–58, doi:10.1016/j.still.2003.10.003.

56.  Assefa, S.; Biazin, B.; Muluneh, A.; Yimer, F.; Haileslassie, A. Rainwater harvesting for supplemental irrigation of onions in the southern dry lands of Ethiopia. *Agric. Water Manag.* 2016, *178*, 325–334, doi:10.1016/j.agwat.2016.10.012.

57.  Walker, S.; Tsubo, M.; Hensley, M. Quantifying risk for water harvesting under semi-arid conditions. *Agric. Water Manag.* 2005, *76*, 94–107, doi:10.1016/j.agwat.2005.01.007.

58.  Zougmoré, R.; Zida, Z.; Kambou, N.F. Role of nutrient amendments in the success of half-moon soil and water conservation practice in semiarid Burkina Faso. *Soil Tillage Res.* 2003, *71*, 143–149, doi:10.1016/S0167-1987(03)00050-3.

59.  Hensley, M.; Bennie, A.; Van Rensburg, L.; Botha, J. Review of 'plant available water' aspects of water use efficiency under irrigated and dryland conditions. *Water SA* 2011, *37*, doi:10.4314/wsa.v37i5.14.

60.  Ammar, A.; Riksen, M.; Ouessar, M.; Ritsema, C. Identification of suitable sites for rainwater harvesting structures in arid and semi-arid regions: A review. *Int. Soil Water Conserv. Res.* 2016, *4*, 108–120, doi:10.1016/j.iswcr.2016.03.001.

61.  Critchley, W.; Siegert, K.; Chapman, C. Water harvesting, A manual guide for the design and construction of water harvesting schemes for plant production, FAO, Rome. 1991.

62.  Oweis, T.Y. *Water harvesting and supplemental irrigation for improved water use efficiency in dry areas*; SWIM paper; International Water

Management Institute: Colombo, Sri Lanka, 1999; ISBN 978-92-9090-378-9.

63. Mekdaschi Studer, R.; Liniger, H. *Water Harvesting: Guidelines to Good Practice.*; Centre for Development and Environment (CDE): Bern, 2013; ISBN 978-3-905835-35-9.

64. Salazar, O.; Casanova, M. Runoff Water Harvesting as a Strategy for Increasing Agricultural Production on Hillslope Areas in Arid and Semiarid Zones. In *Water Recycling and Water Management*; Water Resource Planning, Development and Management Environmental Science, Engineering and Technology; Daniel M. Carrey, 2011; pp. 1–39 ISBN 978-1-61761-305-0.

65. Vohland, K.; Barry, B. A review of in situ rainwater harvesting (RWH) practices modifying landscape functions in African drylands. *Agric. Ecosyst. Environ.* 2009, *131*, 119–127, doi:10.1016/j.agee.2009.01.010.

66. Biazin, B.; Sterk, G.; Temesgen, M.; Abdulkedir, A.; Stroosnijder, L. Rainwater harvesting and management in rainfed agricultural systems in sub-Saharan Africa – A review. *Phys. Chem. Earth Parts ABC* 2012, *47–48*, 139–151, doi:10.1016/j.pce.2011.08.015.

67. Gould, J.; Qiang, Z. *Every Last Drop: Rainwater Harvesting and Sustainable Technologies in Rural China*; 2012.

68. Ray, M.; Simpson, B. *Agricultural Adaptation to Climate Change in the Sahel: Profiles of agricultural management practices*; 2014.

69. Turton, A.R.; Ohlsson, L. Water scarcity and social stability: towards a deeper understanding of the key concepts needed to manage water scarcity in developing countries. 1999, 23.

70. Mukheibir, P. Water Access, Water Scarcity, and Climate Change. *Environ. Manage.* 2010, *45*, 1027–1039, doi:10.1007/s00267-010-9474-6.

71. Seidou, O. Climate Change May Result in More Water Availability in Parts of the African Sahel. In *Innovations and Interdisciplinary Solutions for Underserved Areas*; Kebe, C.M.F., Gueye, A., Ndiaye, A., Garba, A., Eds.; Springer International Publishing: Cham, 2018; Vol. 249, pp. 143–152 ISBN 978-3-319-98877-1.

72. Bigi, V.; Pezzoli, A.; Rosso, M. Past and Future Precipitation Trend Analysis for the City of Niamey (Niger): An Overview. *Climate* 2018, *6*, 73–73, doi:10.3390/cli6030073.

73. Kimaru-Muchai, S.W.; Ngetich, F.K.; Baaru, M.; Mucheru-Muna, M.W. Adoption and utilisation of Zai pits for improved farm productivity in drier upper Eastern Kenya. 2020, doi:10.17170/KOBRA-202002281030.

74. Zougmoré, R.; Zida, Z.; Kambou, N.F. Role of nutrient amendments in the success of half-moon soil and water conservation practice in semiarid Burkina Faso. *Soil Tillage Res.* 2003, *71*, 143–149, doi:10.1016/S0167-1987(03)00050-3.

75. Masse, D.; Hien, E.; Kaboré, T.; Bilgo, A.; Hien, V.; Chotte, J.-L. Evolution of farming practices in sub-Saharan region confronted by demographic and climatic changes: runoff control and organic matter resources management. *Procedia Environ. Sci.* 2011, *9*, 124–129, doi:10.1016/j.proenv.2011.11.020.

76. Lahmar, R.; Bationo, B.A.; Dan Lamso, N.; Guéro, Y.; Tittonell, P. Tailoring conservation agriculture technologies to West Africa semi-arid zones: Building on traditional local practices for soil restoration. *Field Crops Res.* 2012, *132*, 158–167, doi:10.1016/j.fcr.2011.09.013.

77. Wouterse, F. Empowerment, climate change adaptation, and agricultural production: evidence from Niger. *Clim. Change* 2017, *145*, 367–382, doi:10.1007/s10584-017-2096-8.

78. Zouré, C.; Queloz, P.; Koïta, M.; Niang, D.; Fowé, T.; Yonaba, R.; Consuegra, D.; Yacouba, H.; Karambiri, H. Modelling the water balance on farming practices at plot scale: Case study of Tougou watershed in Northern Burkina Faso. *CATENA* 2019, *173*, 59–70, doi:10.1016/j.catena.2018.10.002.

79. Fatondji, D.; Martius, C.; Bielders, C.L.; Vlek, P.L.G.; Bationo, A.; Gerard, B. Effect of planting technique and amendment type on pearl millet yield, nutrient uptake, and water use on degraded land in Niger. *Nutr. Cycl. Agroecosystems* 2007, *76*, 203–217, doi:10.1007/s10705-005-6209-9.

80. Reij, C.; Tappan, G.; Smale, M. Agroenvironmental Transformation in the Sahel: Another Kind of "Green Revolution." 2009, 52.

81. Bazza, M.; Kay, M.; Knutson, C.; FAO; University of Nebraska; National Drought Mitigation Center *Drought characteristics and management in North Africa and the Near East*; 2018; ISBN 978-92-5-130683-3.

82. Adham, A.; Riksen, M.; Ouessar, M.; Ritsema, C. A Methodology to Assess and Evaluate Rainwater Harvesting Techniques in (Semi-) Arid Regions. *Water* 2016, *8*, 198, doi:10.3390/w8050198.

83. Kahinda, J.M.; Lillie, E.S.B.; Taigbenu, A.E.; Taute, M.; Boroto, R.J. Developing suitability maps for rainwater harvesting in South Africa. *Phys. Chem. Earth Parts ABC* 2008, *33*, 788–799, doi:10.1016/j.pce.2008.06.047.

84. Mounirou, L.A.; Zouré, C.O.; Yonaba, R.; Paturel, J.-E.; Mahé, G.; Niang, D.; Yacouba, H.; Karambiri, H. Multi-scale analysis of runoff from a

statistical perspective in a small Sahelian catchment under semi-arid climate. *Arab. J. Geosci.* 2020, *13*, doi:10.1007/s12517-020-5141-2.

85. Mounirou, L.A.; Yacouba, H.; Karambiri, H.; Paturel, J.-E.; Mahé, G. Measuring runoff by plots at different scales: Understanding and analysing the sources of variation. *Comptes Rendus Geosci.* 2012, *344*, 441–448, doi:10.1016/j.crte.2012.08.004.

86. Defersha, M.B.; Melesse, A.M. Field-scale investigation of the effect of land use on sediment yield and runoff using runoff plot data and models in the Mara River basin, Kenya. *CATENA* 2012, *89*, 54–64, doi:10.1016/j.catena.2011.07.010.

87. Vaezi, A.R. Modeling Runoff from Semi-Arid Agricultural Lands in Northwest Iran. *Pedosphere* 2014, *24*, 595–604, doi:10.1016/S1002-0160(14)60045-X.

88. Hernández-Bernal, N. Water harvesting as a tool to allow environmental recovery in a semi-arid region in Brazil. In Proceedings of the 2007; Sydney, Australia.

89. Tamagnone, P.; Comino, E.; Rosso, M. Landscape Metrics Integrated in Hydraulic Modeling for River Restoration Planning. *Environ. Model. Assess.* 2020, doi:10.1007/s10666-020-09693-y.

90. Freni, G.; Liuzzo, L. Effectiveness of Rainwater Harvesting Systems for Flood Reduction in Residential Urban Areas. *Water* 2019, *11*, 1389, doi:10.3390/w11071389.

91. Haider, H.; Ghumman, A.R.; Al-Salamah, I.S.; Ghazaw, Y.; Abdel-Maguid, R.H. Sustainability Evaluation of Rainwater Harvesting-Based Flood Risk Management Strategies: A Multilevel Decision-Making Framework for Arid Environments. *Arab. J. Sci. Eng.* 2019, *44*, 8465–8488, doi:10.1007/s13369-019-03848-0.

92. Palla, A.; Gnecco, I.; La Barbera, P. The impact of domestic rainwater harvesting systems in storm water runoff mitigation at the urban block scale. *J. Environ. Manage.* 2017, *191*, 297–305, doi:10.1016/j.jenvman.2017.01.025.

93. Teston, A.; Teixeira, C.; Ghisi, E.; Cardoso, E. Impact of Rainwater Harvesting on the Drainage System: Case Study of a Condominium of Houses in Curitiba, Southern Brazil. *Water* 2018, *10*, 1100, doi:10.3390/w10081100.

94. Al-Seekh, S.H.; Mohammad, A.G. The Effect of Water Harvesting Techniques on Runoff, Sedimentation, and Soil Properties. *Environ. Manage.* 2009, *44*, 37–45, doi:10.1007/s00267-009-9310-z.

95. Ali, A.; Yazar, A.; Abdul Aal, A.; Oweis, T.; Hayek, P. Micro-catchment water harvesting potential of an arid environment. *Agric. Water Manag.* 2010, *98*, 96–104, doi:10.1016/j.agwat.2010.08.002.

96. Welderufael, W.A.; Le Roux, P.A.L.; Hensley, M. Quantifying rainfall–runoff relationships on the Dera Calcic Fluvic Regosol ecotope in Ethiopia. *Agric. Water Manag.* 2008, *95*, 1223–1232, doi:10.1016/j.agwat.2008.04.007.

97. Verbist, K.; Cornelis, W.M.; Gabriels, D.; Alaerts, K.; Soto, G. Using an inverse modelling approach to evaluate the water retention in a simple water harvesting technique. *Hydrol Earth Syst Sci* 2009, 14.

98. Fiorillo, E.; Crisci, A.; Issa, H.; Maracchi, G.; Morabito, M.; Tarchiani, V. Recent Changes of Floods and Related Impacts in Niger Based on the ANADIA Niger Flood Database. *Climate* 2018, *6*, 59–59, doi:10.3390/cli6030059.

99. Fick, S.E.; Hijmans, R.J. WorldClim 2: new 1-km spatial resolution climate surfaces for global land areas. *Int. J. Climatol.* 2017, *37*, 4302–4315, doi:10.1002/joc.5086.

100. HarvestChoice Long-term Annual Rainfall (mm, 1960-2014). Available online: https://harvestchoice.org/data/pre_mean (accessed on Dec 4, 2019).

101. Ali, A.; Lebel, T. The Sahelian standardized rainfall index revisited. *Int. J. Climatol.* 2009, *29*, 1705–1714, doi:10.1002/joc.1832.

102. Dame, M.C.W.// U. of N. Country Index // Notre Dame Global Adaptation Initiative // University of Notre Dame Available online: https://gain.nd.edu/our-work/country-index/ (accessed on Jul 2, 2020).

103. Todzo, S.; Bichet, A.; Diedhiou, A. Intensification of the hydrological cycle expected in West Africa over the 21st century. *Earth Syst. Dyn.* 2020, *11*, 319–328, doi:10.5194/esd-11-319-2020.

104. Kandji, S.T.; Verchot, L.; Mackensen, J. Climate Change Climate and Variability in Southern Africa: 2006, 42.

105. Tiepolo, M.; Bacci, M.; Braccio, S. Multihazard Risk Assessment for Planning with Climate in the Dosso Region, Niger. *Climate* 2018, *6*, 67, doi:10.3390/cli6030067.

106. Tiepolo, M.; Tarchiani, V. *Risque et adaptation climatique dans la région Tillabéri, Niger*; 2016; ISBN 978-2-343-08493-0.

107. Fiorillo, E.; Maselli, F.; Tarchiani, V.; Vignaroli, P. Analysis of land degradation processes on a tiger bush plateau in South West Niger using MODIS and LANDSAT TM/ETM+ data. *Int. J. Appl. Earth Obs. Geoinformation* 2017, *62*, 56–68, doi:10.1016/j.jag.2017.05.010.

108. SLAPIS: Système Locale d'Alerte Precoce contre les Inondations de la Sirba Available online: https://www.slapis-niger.org/fr.

109. Paturel, J.-E.; Ouedraogo, M.; Servat, E.; Mahe, G.; Dezetter, A.; Boyer, J.-F. The concept of rainfall and streamflow normals in West and Central Africa in a context of climatic variability. *Hydrol. Sci. J.* 2003, *48*, 125–137, doi:10.1623/hysj.48.1.125.43479.

110. Amani, A.; Paturel, J.-E. Le projet de révision des normes hydrologiques en Afrique de l'Ouest et Afrique Centrale. *La Météorologie* 2017, doi:https://doi.org/10.4267/2042/61964.

111. Wilcox, C.; Vischel, T.; Panthou, G.; Bodian, A.; Blanchet, J.; Descroix, L.; Quantin, G.; Cassé, C.; Tanimoun, B.; Kone, S. Trends in hydrological extremes in the Senegal and Niger Rivers. *J. Hydrol.* 2018, *566*, 531–545, doi:10.1016/j.jhydrol.2018.07.063.

112. Alfieri, L.; Salamon, P.; Bianchi, A.; Neal, J.; Bates, P.; Feyen, L. Advances in pan-European flood hazard mapping. *Hydrol. Process.* 2014, *28*, 4067–4077, doi:10.1002/hyp.9947.

113. Barredo, J.I.; de Roo, A.; Lavalle, C. Flood risk mapping at European scale. *Water Sci. Technol.* 2007, *56*, 11–17, doi:10.2166/wst.2007.531.

114. Tehrany, M.S.; Jones, S.; Shabani, F. Identifying the essential flood conditioning factors for flood prone area mapping using machine learning techniques. *CATENA* 2019, *175*, 174–192, doi:10.1016/j.catena.2018.12.011.

115. BRUNET-MORE, Y.; CHAPERON, P.; LAMAGAT, J.P.; MOLINIER, M. *Monographie Hydrologique Du Fleuve Niger*; 1986; ISBN 2-7099-0790-9.

116. Herschy, R.W. *Streamflow Measurement*; Chapman & Hall, Ed.; Second.; 1995.

117. Juston, J.; Jansson, P.-E.; Gustafsson, D. Rating curve uncertainty and change detection in discharge time series: case study with 44-year historic data from the Nyangores River, Kenya: RATING CURVE UNCERTAINTY AND CHANGE DETECTION IN DISCHARGE TIME SERIES. *Hydrol. Process.* 2014, *28*, 2509–2523, doi:10.1002/hyp.9786.

118. Wang, X.; H. Wen, Q.; Wu, Y. *Penalized Maximal t Test for Detecting Undocumented Mean Change in Climate Data Series*; 2007; Vol. 46.

119. Wang, X.L. Accounting for Autocorrelation in Detecting Mean Shifts in Climate Data Series Using the Penalized Maximal t or F Test. *J. Appl. Meteorol. Climatol.* 2008, *47*, 2423–2444, doi:10.1175/2008JAMC1741.1.

120. Leboutillier, D.W.; Waylen, P. *Regional variations in flow-duration curves for rivers in British Columbia, Canada*; 1993; Vol. 14.

121. T, S.; A, M.; Anttila, P.; Ruoho-Airola, T.; T, A. *MAKESENS 1.0.xls*; 2013;

122. Kraus, E.B. Subtropical Droughts and Cross-Equatorial Energy Transports. *Mon. Weather Rev.* 1977, *105*, 1009–1018, doi:10.1175/1520-0493(1977)105<1009:SDACEE>2.0.CO;2.

123. Katz, R.W.; Glantz, M.H. Anatomy of a Rainfall Index. *Mon. Weather Rev.* 1986, *114*, 764–771, doi:10.1175/1520-0493(1986)114<0764:AOARI>2.0.CO;2.

124. Jaranilla-Sanchez, P.A.; Wang, L.; Koike, T. Modeling the hydrologic responses of the Pampanga River basin, Philippines: A quantitative approach for identifying droughts. *Water Resour. Res.* 2011, *47*, doi:10.1029/2010WR009702.

125. Babatolu, J.S.; Akinnubi, R.T. Surface Temperature Anomalies in the River Niger Basin Development Authority Areas, Nigeria. 2013, *2013*, 532–537, doi:10.4236/acs.2013.34056.

126. Cleveland, W.S.; Devlin, S.J. Locally Weighted Regression: An Approach to Regression Analysis by Local Fitting. *J. Am. Stat. Assoc.* 1988, *83*, 596–610, doi:10.1080/01621459.1988.10478639.

127. Niger Basin Authority Available online: http://www.abn.ne/ (accessed on Mar 4, 2019).

128. Bertilsson, L.; Wiklund, K.; de Moura Tebaldi, I.; Rezende, O.M.; Veról, A.P.; Miguez, M.G. Urban flood resilience – A multi-criteria index to integrate flood resilience into urban planning. *J. Hydrol.* 2018, doi:10.1016/j.jhydrol.2018.06.052.

129. Horn, F.; Elagib, N.A. Building socio-hydrological resilient cities against flash floods: Key challenges and a practical plan for arid regions. *J. Hydrol.* 2018, *564*, 125–132, doi:10.1016/j.jhydrol.2018.07.001.

130. Bodoque, J.M.; Díez-Herrero, A.; Amerigo, M.; García, J.A.; Olcina, J. Enhancing flash flood risk perception and awareness of mitigation actions through risk communication: A pre-post survey design. *J. Hydrol.* 2019, *568*, 769–779, doi:10.1016/j.jhydrol.2018.11.007.

131. Andersson, J.C.M.; Ali, A.; Arheimer, B.; Gustafsson, D.; Minoungou, B. Providing peak river flow statistics and forecasting in the Niger River basin. *Phys. Chem. Earth Parts ABC* 2017, *100*, 3–12, doi:10.1016/j.pce.2017.02.010.

132. Salas, J.D.; Obeysekera, J. Revisiting the Concepts of Return Period and Risk for Nonstationary Hydrologic Extreme Events. *J. Hydrol. Eng.* 2014, *19*, 554–568, doi:10.1061/(ASCE)HE.1943-5584.0000820.

133. Adeloye, A.J.; Mwale, F.D.; Dulanya, Z. A metric-based assessment of flood risk and vulnerability of rural communities in the Lower Shire Valley, Malawi. *Proc. Int. Assoc. Hydrol. Sci.* 2015, *370*, 139–145, doi:10.5194/piahs-370-139-2015.

134. Ghile, Y.B.; Taner, M.Ü.; Brown, C.; Grijsen, J.G.; Talbi, A. Bottom-up climate risk assessment of infrastructure investment in the Niger River Basin. *Clim. Change* 2014, *122*, 97–110, doi:10.1007/s10584-013-1008-9.

135. Nkeki, F.N.; Henah, P.J.; Ojeh, V.N. Geospatial Techniques for the Assessment and Analysis of Flood Risk along the Niger-Benue Basin in Nigeria. *J. Geogr. Inf. Syst.* 2013, *05*, 123–135, doi:10.4236/jgis.2013.52013.

136. Odunuga, S.; Adegun, O.; Raji, S.A.; Udofia, S. Changes in flood risk in Lower Niger–Benue catchments. *Proc. Int. Assoc. Hydrol. Sci.* 2015, *370*, 97–102, doi:10.5194/piahs-370-97-2015.

137. Brunner, G.W. *HEC-RAS, River Analysis System Hydraulic Reference Manual*; US ARMY CORPS OF ENGINEERSHYDROLOGIC ENGINEERING CENTER (HEC), 2016.

138. Brunner, G.W. *HEC-RAS river analysis system: User's manual*; US Army Corps of Engineers, Institute for Water Resources, Hydrologic Engineering Center (HEC), 2002.

139. Chow, Te Ven *Open-Channel Hydraulics*; McGraw-Hill: New York, 1959;

140. Ligget, J.A.; Cunge, J.A. *Numerical methods of solution of the unsteady flow equations*; Water Resources Pubblications: Colorado, 1975.

141. Brunner, Gary W. *HEC-RAS River Analysis System: Hydraulic Reference Manual Version 5.0*; US Army Corps of Engineers - Hydrologic Engineering Center (HEC): Davis, California, 2016.

142. Detert, M.; Weitbrecht, V. Automatic object detection to analyze the geometry of gravel grains – a free stand-alone tool. *River Flow 2012* 2012, 595–600.

143. Detert, M.; Weitbrecht, V. User guide to gravelometric image analysis by BASEGRAIN. *Advances in River Sediment Research*.

144. Irmay, S. On steady Flow Formulas in Pipes and Channels. In Proceedings of the IAHR 3rd Congress; Grenoble, 1949.

145. CNR-IBE Il Sistema Locale di Allerta Precoce per le Inondazioni della Sirba (SLAPIS) Available online: https://climateservices.it/7232-2/ (accessed on Oct 7, 2020).

146. Tamagnone, P.; Comino, E.; Rosso, M. Rainwater harvesting techniques as an adaptation strategy for flood mitigation. *J. Hydrol.* 2020, *586*, 124880, doi:10.1016/j.jhydrol.2020.124880.

147. Tamagnone, P.; Cea, L.; Comino, E.; Rosso, M. Rainwater Harvesting Techniques to Face Water Scarcity in African Drylands: Hydrological Efficiency Assessment. *Water* 2020, *12*, 2646, doi:10.3390/w12092646.

148. Urama, K.C.; Ozor, N. IMPACTS OF CLIMATE CHANGE ON WATER RESOURCES IN AFRICA: the Role of Adaptation. 2010, 29.

149. Qadir, M.; Sharma, B.R.; Bruggeman, A.; Choukr-Allah, R.; Karajeh, F. Non-conventional water resources and opportunities for water augmentation to achieve food security in water scarce countries. *Agric. Water Manag.* 2007, *87*, 2–22, doi:10.1016/j.agwat.2006.03.018.

150. Oweis, T.Y. Rainwater harvesting for restoring degraded dry agro-pastoral ecosystems: a conceptual review of opportunities and constraints in a changing climate. *Environ. Rev.* 2017, *25*, 135–149, doi:10.1139/er-2016-0069.

151. Bladé, E.; Cea, L.; Corestein, G.; Escolano, E.; Puertas, J.; Vázquez-Cendón, E.; Dolz, J.; Coll, A. Iber: herramienta de simulación numérica del flujo en ríos. *Rev. Int. Métod. Numér. Para Cálculo Diseño En Ing.* 2014, *30*, 1–10, doi:10.1016/j.rimni.2012.07.004.

152. Oweis, T.; Prinz, D.; Hachum, A. *Water harvesting: indigenous knowledge for the future of the drier environments. ICARDA, Aleppo, Syria, 40 pp*; 2001.

153. Yazar, A.; Ali, A. Water Harvesting in Dry Environments. In *Innovations in Dryland Agriculture*; Farooq, M., Siddique, K.H.M., Eds.; Springer International Publishing: Cham, 2016; pp. 49–98 ISBN 978-3-319-47927-9.

154. WOCAT Available online: https://qcat.wocat.net/en/wocat/ (accessed on Feb 27, 2019).

155. Casulli, V. A high-resolution wetting and drying algorithm for free-surface hydrodynamics. *Int. J. Numer. Methods Fluids* 2009, *60*, 391–408, doi:10.1002/fld.1896.

156. Casulli, V.; Stelling, G.S. Semi-implicit subgrid modelling of three-dimensional free-surface flows. *Int. J. Numer. Methods Fluids* 2011, *67*, 441–449, doi:10.1002/fld.2361.

157. Soil Conservation Service *National Engineering Handbook, section 4, Hydrology,*; U. S. Dept. of Agriculture: Washington, D.C, 1972.

158. Mishra, S.K.; Singh, V.P. SCS-CN Method. In *Soil Conservation Service Curve Number (SCS-CN) Methodology*; Mishra, S.K., Singh, V.P., Eds.;

Springer Netherlands: Dordrecht, 2003; pp. 84–146 ISBN 978-94-017-0147-1.

159. Peugeot, C.; Esteves, M.; Galle, S.; Rajot, J.L.; Vandervaere, J.P. Runoff generation processes: results and analysis of field data collected at the East Central Supersite of the HAPEX-Sahel experiment. *J. Hydrol.* 1997, *188–189*, 179–202, doi:10.1016/S0022-1694(96)03159-9.

160. Vischel, T.; Lebel, T. Assessing the water balance in the Sahel: Impact of small scale rainfall variability on runoff. Part 2: Idealized modeling of runoff sensitivity. *J. Hydrol.* 2007, *333*, 340–355, doi:10.1016/j.jhydrol.2006.09.007.

161. Gerbaux, M.; Hall, N.; Dessay, N.; Zin, I. The sensitivity of Sahelian runoff to climate change. *Hydrol. Sci. J.* 2009, *54*, 5–16, doi:10.1623/hysj.54.1.5.

162. QGIS Development Team *QGIS Geographic Information System*; Open Source Geospatial Foundation, 2009.

163. Belcore, E.; Piras, M.; Pezzoli, A.; Massazza, G.; Rosso, M. RASPBERRY PI 3 MULTISPECTRAL LOW-COST SENSOR FOR UAV BASED REMOTE SENSING. CASE STUDY IN SOUTH-WEST NIGER. *ISPRS - Int. Arch. Photogramm. Remote Sens. Spat. Inf. Sci.* 2019, *XLII-2/W13*, 207–214, doi:10.5194/isprs-archives-XLII-2-W13-207-2019.

164. Mathon, V.; Laurent, H.; Lebel, T. Mesoscale Convective System Rainfall in the Sahel. *J. Appl. Meteorol.* 2002, *41*, 1081–1092, doi:10.1175/1520-0450(2002)041<1081:MCSRIT>2.0.CO;2.

165. Gaillardet, J.; Braud, I.; Hankard, F.; Anquetin, S.; Bour, O.; Dorfliger, N.; de Dreuzy, J.R.; Galle, S.; Galy, C.; Gogo, S.; et al. OZCAR: The French Network of Critical Zone Observatories. *Vadose Zone J.* 2018, *17*, 180067, doi:10.2136/vzj2018.04.0067.

166. Galle, S.; Grippa, M.; Peugeot, C.; Moussa, I.B.; Cappelaere, B.; Demarty, J.; Mougin, E.; Panthou, G.; Adjomayi, P.; Agbossou, E.K.; et al. AMMA-CATCH, a Critical Zone Observatory in West Africa Monitoring a Region in Transition. *Vadose Zone J.* 2018, *17*, 180062, doi:10.2136/vzj2018.03.0062.

167. Jansen, P.P.; Van Bendegom, L.; Van den Berg, J.; De Vries, M.; Zanen, A. *Principles of river engineering: The non-tidal alluvial river*; Delftse Uitgevers Maatschappij, 1994; ISBN 90-6562-146-6.

168. Cea, L.; Legout, C.; Darboux, F.; Esteves, M.; Nord, G. Experimental validation of a 2D overland flow model using high resolution water depth and velocity data. *J. Hydrol.* 2014, *513*, 142–153, doi:10.1016/j.jhydrol.2014.03.052.

169. Cea, L.; Bladé, E. A simple and efficient unstructured finite volume scheme for solving the shallow water equations in overland flow applications: THE SHALLOW WATER EQUATIONS FOR OVERLAND FLOW APPLICATIONS. *Water Resour. Res.* 2015, *51*, 5464–5486, doi:10.1002/2014WR016547.

170. Cea, L.; Legout, C.; Grangeon, T.; Nord, G. Impact of model simplifications on soil erosion predictions: application of the GLUE methodology to a distributed event-based model at the hillslope scale: Impact of model simplifications on soil erosion predictions. *Hydrol. Process.* 2016, *30*, 1096–1113, doi:10.1002/hyp.10697.

171. Cea, L.; Fraga, I.; Puertas, J.; Álvarez, M.; Bermúdez, M.; Coquerez, S.; Salsón, S.; Pettazzi, A. Influencia de la densidad espacial de estaciones pluviométricas y de la disponibilidad de datos radar en los hidrogramas de tormenta calculados con un modelo hidrológico distribuido: Aplicación a una cuenca de 24 Km2 en el Noroeste de España. In Proceedings of the IV Jornadas de Ingeniería del Agua, JIA2015; Córdoba, 2015; p. 10.

172. Fraga, I.; Cea, L.; Puertas, J. Effect of rainfall uncertainty on the performance of physically based rainfall–runoff models. *Hydrol. Process.* 2019, *33*, 160–173, doi:10.1002/hyp.13319.

173. Chow, V.T.; Maidment, D.R.; Mays, L.W. *Applied hydrology*; McGraw-Hill series in water resources and environmental engineering; McGraw-Hill: New York, 1988; ISBN 978-0-07-010810-3.

174. Helton, J.C.; Davis, F.J. Latin hypercube sampling and the propagation of uncertainty in analyses of complex systems. *Reliab. Eng. Syst. Saf.* 2003, *81*, 23–69, doi:10.1016/S0951-8320(03)00058-9.

175. McKay, M.D.; Beckman, R.J.; Conover, W.J. A Comparison of Three Methods for Selecting Values of Input Variables in the Analysis of Output from a Computer Code. *Technometrics* 1979, *21*, 239–245, doi:10.2307/1268522.

176. Olsson, A.; Sandberg, G.; Dahlblom, O. On Latin hypercube sampling for structural reliability analysis. *Struct. Saf.* 2003, *25*, 47–68, doi:10.1016/S0167-4730(02)00039-5.

177. Peugeot, C.; Cappelaere, B.; Vieux, B.E.; Séguis, L.; Maia, A. Hydrologic process simulation of a semiarid, endoreic catchment in Sahelian West Niger. 1. Model-aided data analysis and screening. *J. Hydrol.* 2003, *279*, 224–243, doi:10.1016/S0022-1694(03)00181-1.

178. Delestre, O.; Esteves, M. Rainfall overland flow simulations and real events in Niger. 2010, 9.

179. van de Giesen, N.; Stomph, T.J.; de Ridder, N. Surface runoff scale effects in West African watersheds: modeling and management options. *Agric. Water Manag.* 2005, *72*, 109–130, doi:10.1016/j.agwat.2004.09.007.

180. Abdou, M.M.; Vandervaere, J.-P.; Descroix, L.; Bouzou, I.; Maiga, O.F.; Abdou, S.; Seyni, B.B.; Daouda, L.O. Évolution de la conductivité hydraulique d'un sol sableux cultivé du Niger. 12.

181. Valentin, C. Surface crusts of semi-arid sandy soils: types, functions and management. In Proceedings of the Physical properties of tropical sandy soils; 2005; p. 12.

182. Esteves, M.; Faucher, X.; Galle, S.; Vauclin, M. Overland flow and infiltration modelling for small plots during unsteady rain: numerical results versus observed values. *J. Hydrol.* 2000, *228*, 265–282, doi:10.1016/S0022-1694(00)00155-4.

183. Rockström, J.; Barron, J.; Fox, P. Rainwater management for increased productivity among small-holder farmers in drought prone environments. *Phys. Chem. Earth Parts ABC* 2002, *27*, 949–959, doi:10.1016/S1474-7065(02)00098-0.

184. Aune, J.B.; Coulibaly, A.; Giller, K.E. Precision farming for increased land and labour productivity in semi-arid West Africa. A review. *Agron. Sustain. Dev.* 2017, *37*, doi:10.1007/s13593-017-0424-z.

185. Roose, E.; Kabore, V.; Guenat, C. Zai Practice: A West African Traditional Rehabilitation System for Semiarid Degraded Lands, a Case Study in Burkina Faso. *Arid Soil Res. Rehabil.* 1999, *13*, 343–355, doi:10.1080/089030699263230.

186. Descroix, L.; Laurent, J.-P.; Vauclin, M.; Amogu, O.; Boubkraoui, S.; Ibrahim, B.; Galle, S.; Cappelaere, B.; Bousquet, S.; Mamadou, I.; et al. Experimental evidence of deep infiltration under sandy flats and gullies in the Sahel. *J. Hydrol.* 2012, *424–425*, 1–15, doi:10.1016/j.jhydrol.2011.11.019.

187. Leblanc, M.J.; Favreau, G.; Massuel, S.; Tweed, S.O.; Loireau, M.; Cappelaere, B. Land clearance and hydrological change in the Sahel: SW Niger. *Glob. Planet. Change* 2008, *61*, 135–150, doi:10.1016/j.gloplacha.2007.08.011.

188. Mamadou, I.; Gautier, E.; Descroix, L.; Noma, I.; Bouzou Moussa, I.; Faran Maiga, O.; Genthon, P.; Amogu, O.; Malam Abdou, M.; Vandervaere, J.-P. Exorheism growth as an explanation of increasing flooding in the Sahel. *CATENA* 2015, *131*, 130–139, doi:10.1016/j.catena.2015.03.017.

189. Kihila, J.M. Indigenous coping and adaptation strategies to climate change of local communities in Tanzania: a review. *Clim. Dev.* 2018, *10*, 406–416, doi:10.1080/17565529.2017.1318739.

190. Xu, H.; Wu, M. A First Estimation of County-Based Green Water Availability and Its Implications for Agriculture and Bioenergy Production in the United States. *Water* 2018, *10*, 148, doi:10.3390/w10020148.

191. Schyns, J.F.; Hoekstra, A.Y.; Booij, M.J.; Hogeboom, R.J.; Mekonnen, M.M. Limits to the world's green water resources for food, feed, fiber, timber, and bioenergy. *Proc. Natl. Acad. Sci.* 2019, *116*, 4893–4898, doi:10.1073/pnas.1817380116.

192. Famiglietti, J.S.; Wood, E.F. Multiscale modeling of spatially variable water and energy balance processes. *Water Resour. Res.* 1994, *30*, 3061–3078, doi:10.1029/94WR01498.

193. Allan, R.; Pereira, L.; Smith, M. *Crop evapotranspiration-Guidelines for computing crop water requirements-FAO Irrigation and drainage paper 56*; 1998; Vol. 56.

194. Doorenbos, J.; Pruitt, W.O. *Guidelines for predicting crop water requirements*; 1977; Vol. 24.

195. Brocca, L.; Melone, F.; Moramarco, T. Distributed rainfall-runoff modelling for flood frequency estimation and flood forecasting. *Hydrol. Process.* 2011, *25*, 2801–2813, doi:10.1002/hyp.8042.

196. del Rio, A.; M. Simpson, B. Agricultural Adaptation to Climate Change in the Sahel: A Review of Fifteen Crops Cultivated in the Sahel 2014.

197. Barry, B.; Olaleye, A.O.; Zougmoré, R.; Fatondji, D. Rainwater harvesting technologies in the Sahelian zone of West Africa and the potential for outscaling. In Working Paper; Colombo, Sri Lanka, 2008; p. 40 ISBN 978-92-9090-684-1.

198. Komariah; Senge, M. The development of water harvesting research for agriculture. *Rev. Agric. Sci.* 2013, *1*, 31–42, doi:10.7831/ras.1.31.

199. Li, C.; Hoffland, E.; Kuyper, T.W.; Yu, Y.; Zhang, C.; Li, H.; Zhang, F.; van der Werf, W. Syndromes of production in intercropping impact yield gains. *Nat. Plants* 2020, *6*, 653–660, doi:10.1038/s41477-020-0680-9.

200. Burkina Faso: Greening the Sahel Desert across Africa Available online: https://www.weforest.org/project/burkina-faso (accessed on Oct 6, 2020).